AN ABSTRACT OF THE THESIS OF

Benn J. Eilers for the degree of Master of Science in Mechanical Engineering presented on June 3, 2010.

Title: Microchannel Steam-Methane Reforming Under Constant and Variable Surface Temperature Distributions.

Abstract approved:

_____

Vinod Narayanan   Sourabh V. Apte

Steam-methane reforming is a well understood industrial process used for generating hydrogen and synthesis gas. The reaction is generally carried out with residence times on the order of one second. By performing this reaction at microscales it is possible to take advantage of increased heat transfer rates and low diffusion times allowing equipment size and residence times to be decreased by an order of magnitude.

The energy required for the steam-methane reforming reaction could be supplied by solar energy through the use of a solar collector/receiver, thus providing a "cleaner" pathway for hydrogen generation. In such reactors, it is expected that the heat flux and temperature distribution is non-uniform. This study presents a first step in characterizing reforming performance under such variable temperature conditions. The design of the channel was such that the non-uniform heat flux profile expected inside of a solar receiver could be simulated by a controllable temperature profile along the reactor surface.

Experiments were conducted over four catalyst configurations and the effects of average reactor temperature, temperature distribution, residence time, steam-methane ratio, and long duration testing were all evaluated. Results demonstrated over 60% conversion of methane at 900°C and a residence time of 26 milliseconds. Methane conversion was found to be strongly dependent on reactor temperature. Ramping temperature

distributions demonstrated a 46% greater hydrogen output than isothermal reactions performed at the same average temperature.

This work was performed in conjunction with development of a CFD model of reacting flow through a microchannel [1]. The experiments were used to determine the pre-exponential constants of the global reaction rates.

Microchannel Steam-Methane Reforming Under Constant and Variable Surface
Temperature Distributions

by
Benn J. Eilers

A THESIS

submitted to

Oregon State University

in partial fulfillment of
the requirements for the
degree of

Master of Science

Presented June 3, 2010
Commencement June 2010

Master of Science thesis of Benn J. Eilers presented on June 3, 2010

APPROVED:

_____
Co-Major Professor, representing Mechanical Engineering

_____
Co-Major Professor, representing Mechanical Engineering

_____
Head of the School of Mechanical, Industrial, and Manufacturing Engineering

_____
Dean of the Graduate School

I understand that my thesis will become part of the permanent collection of Oregon State University libraries. My signature below authorizes release of my thesis to any reader upon request.

_____
Benn J. Eilers, Author

ACKNOWLEDGEMENTS

TABLE OF CONTENTS

TABLE OF CONTENTS (Continued)

TABLE OF CONTENTS (Continued)

TABLE OF CONTENTS (Continued)

LIST OF FIGURES

LIST OF FIGURES (Continued)

LIST OF TABLES

LIST OF APPENDICES

LIST OF APPENDIX FIGURES

LIST OF APPENDIX TABLES

NOMENCLATURE

h	Height (m)
k_i	Reaction rate constant of reaction i, $(kmol/(kPa^{0.5}\ kg_{cat}\ s))$
K_a	Adsorption coefficient of component a
K_{pi}	Equilibrium constant of reaction i
l	Length (m)
$\dot{\mathcal{M}}_i$	Molar flow rate of component i, $(mole/min)$
$\mathcal{M}_i$	Molecular weight of component i, $(kg/kmol)$
$\dot{m}_i$	Mass flow rate of component i, (g/min)
P_i	Partial pressure of component i, (Pa)
P	Pressure of mixture (Pa)
r_i	Rate of reaction i, $(kmol/m^2 s)$
R_{SM}	Steam-methane ratio (molar basis), $(moles/s)/(moles/s)$
t_{res}	Residence time (s)
T	Temperature $(°C)$
U	Average velocity (m/s), Uncertainty (%)
$\dot{V}$	Volumetric flow rate (m^3/s)
w	Width (m)
X_i	Molar fraction of component i
Y_i	Mass fraction of component i
ΔH_{298}	Enthalpy change of reaction (kJ/mol)

Greek

ρ_i Density of component i, (kg/m^3)

μ Viscosity $(kg/s \cdot m)$

Microchannel Steam-Methane Reforming Under Constant and Variable Surface Temperature Distributions

1. INTRODUCTION

The dwindling supply of easily accessible fossil fuels combined with concern surrounding man-made climate change have recently accelerated research into alternative energy technologies. Hydrogen has been investigated extensively as an alternative fuel source due to the lack of CO_2 production during combustion, and the ability to generate energy directly using fuel cells. Hydrogen can be produced using a variety of methods including electrolysis, thermolysis, partial oxidation, and steam reforming. Of these options, steam reforming of methane is the most economical and most widely used method of hydrogen generation [2,3]. This process has been used for over 70 years, with the majority of hydrogen produced being used for ammonia production [4]. Steam-methane reforming involves the following three reactions.

$$CH_4 + H_2O \leftrightarrow CO + 3H_2 \qquad \Delta H_{298} = 206 \ kJ/mol \qquad (1.1)$$

$$CO + H_2O \leftrightarrow CO_2 + H_2 \qquad \Delta H_{298} = -41 \ kJ/mol \qquad (1.2)$$

$$CH_4 + 2H_2O \leftrightarrow CO_2 + 4H_2 \qquad \Delta H_{298} = 165 \ kJ/mol \qquad (1.3)$$

The reactions in Eq. (1.1) and Eq. (1.2) are known as the steam-methane reforming reactions, and are highly endothermic. The reaction in Eq. (1.2) is the water-gas shift reaction and is generally carried out at lower temperatures (210 - 330°C) over a Cu catalyst and is used to strip CO from the gas mixture to avoid contamination of fuel cells [2,5]. The sum of reactions (1.1) and (1.2) can be expressed as a total reaction as seen in Eq. (1.3).

The thermodynamic equilibrium of the gas mixture at multiple temperatures was calculated using STANJAN software and is shown in Fig. 1.1 for a pressure of 101 kPa and a steam-methane ratio of 3. The software allows one to calculate the chemical composition with minimum Gibbs free energy for a given atomic composition. The

thermodynamic equilibrium of the reaction is such that temperatures in excess of 700°C are required to achieve full conversion of methane.
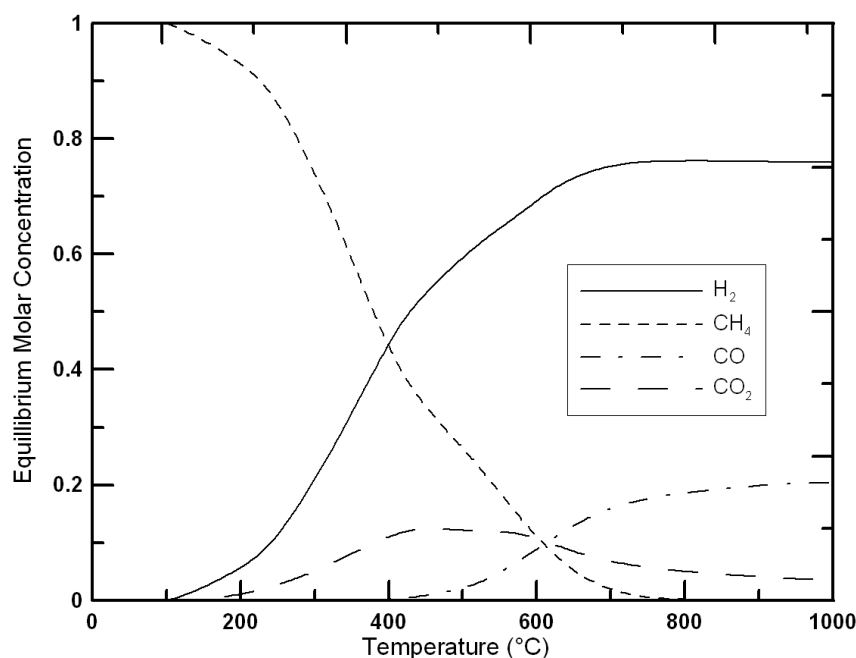
Fig. 1.1: Equilibrium composition of dry product stream (P=101 kPa, R_{SM} =3)

Negligible conversion is seen until the reaction temperature occurs at over 200°C. Increasing temperatures produce higher H_2 equilibrium concentrations until the H_2 concentration reaches a maximum near 800°C. The H_2 equilibrium concentration slightly declines at temperatures over 800°C due to an increase in the reverse water gas shift reaction (0.2% reduction from 800°C to 1000°C).

The energy for the high temperature endothermic reaction can be supplied from a multitude of sources, but is generally supplied from the combustion of fossil fuel sources. In areas with high direct solar radiation, the solar thermal processing of methane is a viable option and is the motivation for this research. By using clean solar energy to produce hydrogen, the "carbon footprint" of the overall process is greatly reduced. It has been suggested that hydrogen could account for $3 - 8\%$ of final energy usage in the

United States by 2050 [4], further driving the need for clean hydrogen production technology.

This research represents a first step in the development of a microchannel solar reactor. The experimental study examines steam-methane reforming carried out in a microchannel subjected to flat and longitudinally variable surface temperature profiles designed to simulate conditions on the inside wall of a solar receiver.

2. LITERATURE REVIEW

The research presented in this thesis involved a combination of three overlapping fields of study: steam-methane reforming, microchannel technology, and solar fuel processing. In this chapter each of these fields is investigated in turn.

2.1 Steam-Methane Reforming

Steam-methane reforming is a well understood industrial process used to produce hydrogen and syngas (a mixture of hydrogen and carbon monoxide). The majority of this gas is used for ammonia production with a smaller portion being used in hydrocarbon processing facilities for gas-to-liquid Fischer-Tropsch processes. The general configuration of a large scale facility consists of reforming tubes several meters long oriented vertically and heated with side-fired burners. The residence time for reaction in these plants is on the order of seconds. In order for large steam-methane reforming plants to operate efficiently, it is necessary to increase the pressure to the range of 2000 – 4000 kPa [6]. The corresponding density increase of the reacting mixture allows for smaller reforming equipment, thereby reducing capital investment. Equilibrium methane conversion is higher for a given temperature at lower pressures (Fig. 2.1), necessitating an increase in reaction temperature in the larger scale facilities to achieve high hydrogen yield. The data from Fig. 2.1 were adapted from Rostrup-Nielsen et al. [6].
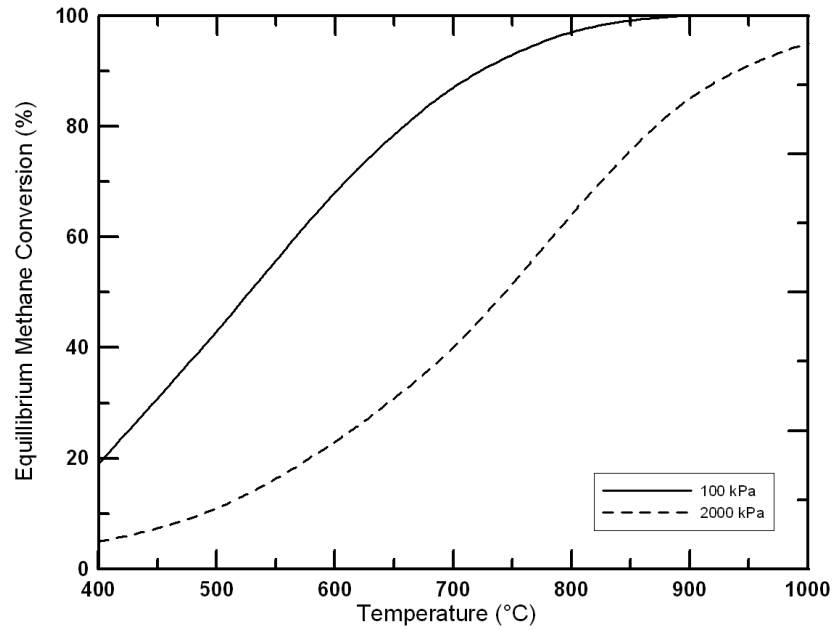
Fig. 2.1: Equilibrium methane conversion (R_{SM} = 2.5)

Industrial steam-methane reformers have historically operated at temperatures below 900°C, but recent advances in materials and technology have allowed operation up to 1050°C with large increases in overall efficiency [7]. The reaction rate kinetics along with discussion of the various available catalysts are presented below.

2.1.1 Chemical Kinetics

A summary of the chemical kinetics studies on steam-methane reforming is presented in Table 2.1.

Table 2.1: Details of chemical kinetics studies

Study	Pressure (kPa)	Temperature (°C)	Catalyst	Rate Controlling Step
Akers and Camp (1955) [8]	101	340 - 638	Ni on Kieselguhr	Adsorption
Bodrov et al. (1964 - 68) [9-11]	101	400 - 900	Ni foil and porous Ni	< 600°C - Reaction > 600°C - Adsorption
Ross and Steel (1972) [12]	102	500 - 600	Ni - Al_2O_3 powder	Adsorption
Agnelli et al. (1987) [13]	101	642 - 737	Ni on Al_2O_3	Adsorption
De Deken (1982) [14]	500 - 1500	550 - 640	Ni on Al_2O_3	Reaction
Numaguchi and Katsutoshi (1988) [15]	120 - 2550	401 - 887	Ni on Al_2O_3	Reaction
Xu and Froment (1989) [16]	500 - 1500	500 - 575	Ni on Mg spinel	Reaction
Hou and Hughes (2000) [17]	120 - 600	475 - 550	Ni on Al_2O_3	Reaction

Kinetic rate equations for heterogeneous reactions were developed in 1955 by Akers and Camp [8], followed by extensive work by Bodrov et al. [9-11]. The reaction rates generated by Bodrov et al. [9-11] postulated that at temperatures above 600°C the reaction was limited by the rate of adsorption, whereas at lower temperatures it was limited by the rate of reaction. Many kinetics models were postulated later in the century, with much disagreement as to what was the rate limiting step of the reaction. Work by Ross and Steel [12] as well as Agnelli et al. [13] surmised that methane adsorption was the rate limiting step, whereas work done by De Deken et al. [14] and Numaguchi and Katsutoshi [15] concluded that the rate limiting step was the rate of reaction.

A 13 step model was suggested by Xu and Froment [16] whereby the adsorbtion, surface reactions, and desorption were all modeled. In this work, the surface reactions were

assumed to be the rate controlling step and the 13 step model was able to be collapsed into a set of three core equations.

$$r_1 = \frac{k_1 \left(P_{CH_4} P_{H_2O} - \frac{P_{CO} P_{H_2}^3}{K_{p1}} \right)}{P_{H_2}^{2.5} (DEN)^2} \tag{2.1}$$

$$r_2 = \frac{k_2 \left(P_{CO} P_{H_2O} - \frac{P_{CO_2} P_{H_2}}{K_{p2}} \right)}{P_{H_2} (DEN)^2} \tag{2.2}$$

$$r_3 = \frac{k_3 \left(P_{CH_4} P_{H_2O}^2 - \frac{P_{CO_2} P_{H_2}^4}{K_{p3}} \right)}{P_{H_2}^{3.5} (DEN)^2} \tag{2.3}$$

where $DEN = 1 + K_{CO} P_{CO} + K_{H_2} P_{H_2} + K_{CH_4} P_{CH_4} + K_{H_2O} \frac{P_{H_2O}}{P_{H_2}}$, r_i = rate of reaction, k_i = rate coefficient, P_i = partial pressure, K_{pi} = equilibrium constant, and K_i = adsorption constant. These equations were developed for steam reforming over a magnesium supported nickel catalyst at temperatures of 500-575°C with steam to methane molar ratios of 3-5 and operating pressures of 500-1500 kPa. If the reactant stream is a binary mixture of methane and steam, the reaction equations are invalid due to the partial pressure of hydrogen being in the denominator of Eqs. (2.1 - 2.3). To alleviate this problem, hydrogen was added to the feedstock at a hydrogen to methane ratio of 1.25. The Xu and Froment [16] model is the basis for the majority of research into the kinetics of steam-methane reforming.

Hou and Hughes [17] investigated steam-methane reforming over a nickel catalyst supported on α-alumina under similar conditions to that of Xu and Froment [16]. Again, the rate determining step was found to be the reaction rate between the adsorbed species summarized by the following three equations:

$$r_1 = \frac{k_1 \frac{P_{CH_4} P_{H_2O}^{0.5}}{P_{H_2}^{1.25}} \left(1 - \frac{P_{CO} P_{H_2}^3}{K_{p1} P_{H_2O} P_{CH_4}}\right)}{(DEN)^2} \tag{2.4}$$

$$r_2 = \frac{k_2 \frac{P_{CO} P_{H_2O}^{0.5}}{P_{H_2}^{0.5}} \left(1 - \frac{P_{CO_2} P_{H_2}}{K_{p2} P_{CO} P_{H_2O}}\right)}{(DEN)^2} \tag{2.5}$$

$$r_3 = \frac{k_3 \frac{P_{CH_4} P_{H_2O}}{P_{H_2}^{1.75}} \left(1 - \frac{P_{CO_2} P_{H_2}^4}{K_{p3} P_{CH_4} P_{H_2O}^2}\right)}{(DEN)^2} \tag{2.6}$$

where $DEN = 1 + K_{CO} P_{CO} + K_{H_2} P_{H_2O}^{0.5} + K_{H_2O} \frac{P_{H_2O}}{P_{H_2}}$. The variables in Eqs. $(2.4 - 2.6)$ are the same as identified in Eqs. $(2.1 - 2.3)$.

The same issue exists for the chemical kinetics model devised by Hou and Houghes as was seen in the Xu and Froment model whereby an initial lack of hydrogen causes the equations to become undefined.

The numerical work by Peterson [1] employed the use of a simplified alternative analytically based model which was less computationally intensive and avoided the instability associated with the lack of hydrogen at the inlet. The rate of reaction only depended on the concentration of the reactants, as opposed to Eqs. $(2.1 - 2.6)$ which incorporated the concentrations of the products as well as the reactants. Details of the model can be found in Kuo [18]. The three reaction rate equations used in this model are as follows:

$$r_1 = k_1 \left(\frac{\rho}{\mathcal{M}_{CH_4}}\right) \left(\frac{\rho}{\mathcal{M}_{H_2O}}\right) Y_{CH_4} Y_{H_2O} \tag{2.7}$$

$$r_2 = k_2 \left(\frac{\rho}{\mathcal{M}_{CO}}\right) \left(\frac{\rho}{\mathcal{M}_{H_2O}}\right) Y_{CO} Y_{H_2O} \tag{2.8}$$

$$r_3 = k_3 \left(\frac{\rho}{\mathcal{M}_{CH_4}}\right) \left(\frac{\rho}{\mathcal{M}_{H_2O}}\right)^2 Y_{CH_4} Y_{H_2O}^2 \tag{2.9}$$

Where r_i = rate of reaction, k_i = reaction rate constant, ρ = density of the mixture, $\mathcal{M}_i$ = molecular weight, and Y_i = mass fraction. The reaction rate constants (k) were found experimentally through the work discussed herein and are further explained in Peterson [1].

2.1.2 Catalysis

Catalytic activity of methane over certain metals was first observed during the development of the Davy Lamp in 1815. It wasn't until 1924 that experimental reactions verified equilibrium concentrations with the use of a Ni catalyst [19]. Early work focused on catalyst identification and optimization with Ni being the catalyst of choice until recently.

A thorough review of catalyst activity studies combined with experimental work was conducted by Jones et al. [20]. The experimental work by Jones et al. involved testing six different catalytic metals (Ru, Rh, Pd, Pt, Ir, and Ni) in 18 different catalyst configurations in order to determine the order of reactivity. Their findings agreed well with previous studies [21,22] and suggested a reactivity trend as follows:

Ru ~ Rh > Ni ~ Ir ~ Pt ~ Pd

The differences between all metals tested were determined to be small, with Ru and Rh being approximately twice as active as the other metals. It has been shown that of these metals, Ni has the largest tendency to form carbon deposits (coking), and therefore is subject to deactivation under reduced steam-methane ratio testing procedures [23]. For this reason, large-scale reforming plants that employ Ni as a catalyst use a relatively high steam to carbon ratio (~3). Use of noble metal catalysts on an industrial scale has not been adopted due to the high cost of the metal.

A large amount of research has focused on Rh as a catalyst due to its elevated level of reactivity and its resistance to coking [23-30]. Although most industrial reformers operate with residence times on the order of seconds, noble metal catalysts combined with novel reactor designs have been able to greatly reduce the time to acheive equilibrium. Experimental and numerical work by Tonkovich [24] and numerical work

by Stefanidis [31] demonstrated the ability to reduce the necessary reaction time to 1 ms or less.

Palladium catalysts have been used recently in membrane reactors [32-34]. Palladium and its alloys are permeable to H_2. By removing the hydrogen during the reaction, the partial pressure of H_2 is kept low and serves to facilitate the reaction. Most applications use a Ni catalyst in conjunction with the Pd membrane in order to further accelerate the conversion process. Work by Alkhaldi [35] used Pd supported on an intermetallic for steam reforming of methane. Alkahaldi's research combined with in-house expertise on Pd nanoparticle synthesis [36] guided the decision to use Pd as the catalyst for the research presented here.

2.2 Microchannel Reactors

Microchannel technology is a promising field of research that offers several advantages over traditional macroscale applications. The high surface area to volume ratios seen in microreactors allow for greatly enhanced heat transfer and therefore more precise temperature control [35]. The reduced diffusion lengths can be exploited by otherwise mass transfer limited systems resulting in increased reaction rates [37]. The combination of increased reaction rates, reduced residence times, and reduced size of the reactor assembly could allow for total system miniaturization by an order of magnitude. The decreased residence times present in a microreactor can also be used to suppress undesirable slower reactions such as coke formation [38].

The benefits of using microchannels do not come without significant drawbacks, as outlined by Holladay et al. [37]. The pressure drop through the channel is greatly increased and can be quickly exacerbated through coke formation. Sealing the small devices is a non-trivial issue with very few researchers reporting on techniques of assuring a completely sealed system. Thermal management in small reactors becomes difficult due at elevated temperatures due to the large size of the connectors relative to the channel. System monitoring requires specialized techniques and equipment to accurately characterize operational parameters. Very small flow rates of reactants must

be stably fed to the reactor, requiring precise instrumentation. Additionally, small diameter thermocouples must be used to minimize conduction losses where appropriate.

Despite the drawbacks, microchannel technology has been shown to greatly reduce reaction times necessary for hydrogen production in steam-methane reforming. Experimental studies of steam-methane reforming in microchannels are discussed in the following section.

2.3 Steam-Methane Reforming in a Microchannel

A summary of the available literature detailing steam-methane reforming in a microchannel is presented in Table 2.2. Experimental work of steam-methane reforming in a microchannel is limited to research conducted by Pacific Northwest National Laboratory (PNNL) (Richland, WA) [29,39], and collaborations of Velocys, Inc (Plain City, OH) with PNNL, [23,24,27], along with the research by Alkhaldi [35].

Table 2.2: Microchannel steam-methane reforming experiments

Exp.	Reactor	Catalyst	Test Conditions	Details / Findings
Tonkovich et al. (2004) [27]	Inconel w=9.65 mm l=177.8 mm h=250 μm	Rh on MgO/Al$_2$O$_3$ on FeCrAlY Felt	T = 870°C P = 1300 kPa R$_{SM}$ = 3 & 4.8 t$_{res}$ = 4.3 & 6 ms	Parallel flow combustion channels Long duration testing (568 h) ~90% conv observed q" = 17.7 - 18.2 W/cm^2
Wang et al. (2004) [23]	Inconel w=8.9 mm l=50.8 mm h=889 μm	Rh on MgO/Al$_2$O$_3$ on FeCrAlY Felt	T = 650 - 900°C P = 101 kPa R$_{SM}$ = 1 - 3 t$_{res}$ = 25 - 27 ms	FeCrAlY preferable CAT support Stable conv for 40 h. (R$_{SM}$=1, T=900°C) ↑% conv with ↑R$_{SM}$ ↑% conv linear to ↑T
Cao et al. (2005) [39]	Inconel w=9 mm l=51 mm h=250 μm	Rh on MgO/Al$_2$O$_3$ on FeCrAlY Felt	T = 850°C P = 405 - 2027 kPa R$_{SM}$ = 2 t$_{res}$ = 3.8 & 13.8 ms	2 CAT orientations tested 74% conv (P=405 kPa t$_{res}$=3.8 ms) 93% conv (P=405 kPa t$_{res}$=13.8 ms) ↓% conv with ↑P
Alkhaldi (2005) [35]	Inconel w=22 mm l=75 mm h=250 μm	Pd on aluminized FeAl	T = 630 - 1000°C P = 101 kPa R$_{SM}$ = 4.8 - 8.1 t$_{res}$ = 27 - 42 ms	10% conv (T=630°C, t$_{res}$=39ms) 49% conv (T=1000°C, t$_{res}$=27ms) ↑% conv with ↑R$_{SM}$ ↑ CO selectivity with ↑T 24% ↓ in activity after 100 min R$_{SM}$ >1.39 to prevent coking
Tonkovich et al. (2007) [24]	Inconel w=10.7 mm l=11.4 mm h=76 μm	Rh on MgO/Al$_2$O$_3$ on FeCrAlY Felt	T = 811 - 837°C P = 1140 - 1290 kPa R$_{SM}$ = 3 t$_{res}$ = 90 & 900 μs	Crossflow combustion channels 21.3% conv @ 90 μs 99% conv @ 900 μs Stable conv after 100 h.
Johnson et al. (2007) [29]	Inconel w=9.4 mm l=50.8 mm h=390 μm	Rh on porous Al$_2$O$_3$	T = 540 - 900°C P = 101 kPa R$_{SM}$ = 1 t$_{res}$ = 27 ms	10% ↓ in conv after 100 h. @ 900°C only ↑5% conv w 3X ↑ CAT loading ↑ sintering with ↑CAT loading No coking @ R$_{SM}$ = 1
This Work	304 SS l=133 mm w=19 mm h=700 - 1067 μm	Pd on aluminized FeCrAlY	T = 625 - 925°C P = 103 - 201 kPa R$_{SM}$ = 2.54 - 5.8 t$_{res}$ = 5.3 - 42.5 ms	62% conv (T=904°C, R$_{SM}$=2.9, t$_{res}$=26ms) ↑% conv linear to ↑ t$_{res}$ ↑% conv exponential to ↑T No observed R$_{SM}$ dependence

↑:increase, ↓:decrease, T:Temperature, P:Pressure, R$_{SM}$:Steam-Methane ratio, CAT:catalyst, t$_{res}$:Residence Time, conv:Conversion

The work by Tonkovich et al. (2004) [27] looked at long term steam-methane reforming at high pressures (1400 kPa) in a 250 μm channel at residence times of 4.3 and 6 ms. Heat was provided for the reaction by an integrated co-flow combustion chamber

adjacent to the reaction zone. The catalyst bed was located on the wall adjacent to the combustion chamber. The catalyst used in this experiment was Rh on a mixture of MgO and Al_2O_3 subsequently deposited on a FeCrAlY felt material. The catalyst in this work was the same as what was used in all work conducted by PNNL and Velocys Inc. except for the work by Johnson et al. [29], who used a porous Al_2O_3 substrate.

The device was tested in excess of 575 hours. Two different samples were reported by the authors, one at 277 hours, one at 568 hours with results tabulated in Table 2.3.

Table 2.3: Experimental results adapted from Tonkovich et al. (2004) [27]

Sample	1	2
Time on Stream (h)	277	568
Steam-Methane Ratio	4.8	3
Residence Time (ms)	4.3	6
Reactor Pressure (kPa)	1375	1395
Reactor Temp (°C)	868	875
CH_4 Conversion (%)	93.4	89.2

Increased conversions would be expected in sample 2 (Table 2.3), due to the 40% increased residence time and slightly increased temperature. Instead the conversion percent was reduced, thus demonstrating slight deactivation of the catalyst.

It is important to note that in this research, the residence time was calculated by using the entire reactor volume (open channel and porous catalyst volume). The catalyst bed thickness was the same as the open channel height, thus increasing the residence time estimations by two fold over conventional practice of using the open channel volume for residence time calculations.

A modified design of the integrated combustion/reformer unit was examined by Tonkovich et al. (2007) [24]. Multiple cylindrical combustion chambers were situated in a cross-flow configuration to the steam-methane reforming flow. A 0.28 mm thick catalyst bed was situated adjacent to the wall with the combustion chambers and formed an open channel height of 76 μm. This reactor was also tested at high pressures (1300 kPa), but with very low residence times of less than 1 ms. Residence time was calculated

by using the open channel volume only. If the total reactor volume (open channel and catalyst volume) were to have been used, the corresponding residence times would have been increased by a factor of 4.7. The tabulated results for the two sampling points are presented in Table 2.4.

Table 2.4: Experimental results from Tonkovich et al. (2007) [24]

Sample	1	2
Time on Stream (h)	73	10
Steam-methane Ratio	3	3
Residence Time (ms)	0.9	0.09
Reactor Pressure (kPa)	1295	1250
Reactor Temp (°C)	837	811
CH_4 Conversion (%)	88.2	17

Time series conversion data was presented for testing at a residence time of 0.09 ms. Methane conversion percentages stayed stable between 16% and 19% for over 100 hr of testing, suggesting little to no catalyst deactivation.

The reactors studied by Wang et al.[23], Cao et al.[39] and Johnson et al.[29] listed different channel heights, but all had similar width and length dimensions (9 mm by 51 mm). The above mentioned research was all conducted in conjunction with PNNL, suggesting that the experiments were most likely done using the same reactor. In all of the above mentioned experiments the reactor was heated in an oven or furnace to isothermal conditions.

The research by Wang et al. [23] examined the effects of low steam-methane ratios (1 -3) along with analyzing temperature effects between 650 – 900°C. The microchannel height was 889 μm (0.01 in) and was filled entirely with the catalyst bed. All tests were carried out at atmospheric pressure. The conversion of methane was greatly reduced at small steam-methane ratios (Fig. 2.2), but no coke was formed on the catalyst after testing under these conditions for 40 hours. The steam-methane ratio variations were conducted at a fixed temperature of 900°C and residence time of 27 ms.
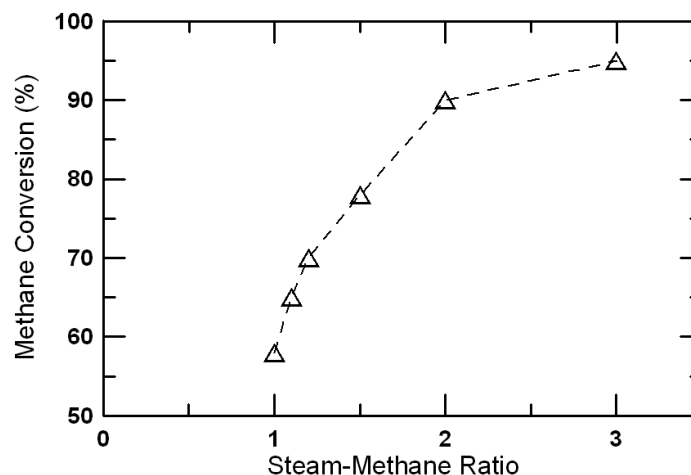
Fig. 2.2: Methane conversion for varying steam-methane ratios [23]

Two different catalyst beds were tested at multiple temperatures. The first catalyst bed was in powder form, and one on an aluminized FeCrAlY catalyst bed (Fig. 2.3). Tests were performed with a steam-methane ratio of 1, pressure of 101 kPa, and residence time of 27 ms. The FeCrAlY catalyst bed provided increased methane conversion at all temperatures tested.
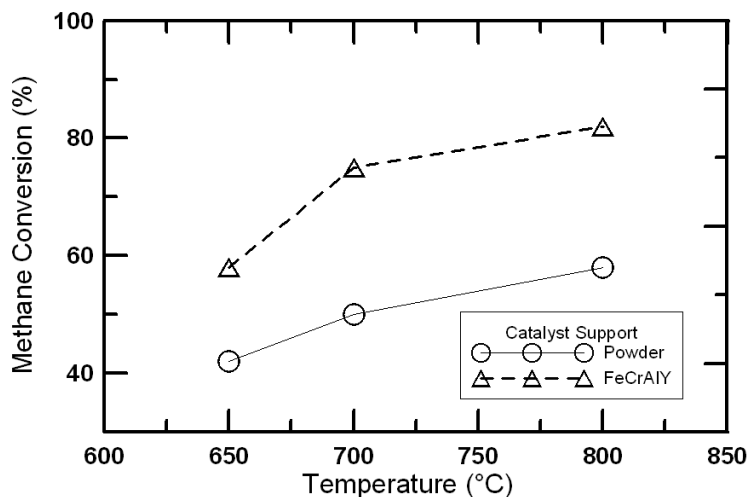
Fig. 2.3: Methane conversion for two catalyst supports (adapted from [23])

Methane conversions were reported over a 14 hour testing period at conditions of steam-methane ratio of unity and reactor temperature of 900°C. A 7% decrease in methane

conversion was observed with initial and final methane conversions of 60% and 56% respectively.

Cao et al. [39] configured the above mentioned reactor such that two 250 μm thick catalyzed FeCrAlY inserts were positioned on either side of the channel, with an open channel gap of 250 μm. The residence times were computed using the open channel volume. Tests were performed at temperature of 850°C with a steam-methane ratio of 2. Two different residence times were tested over a range of pressures. The results are tabulated in Table 2.5.

Table 2.5: Experimental results adapted from Cao et al. [39]

Pressure (kPa)	Residence Time (ms)	CH_4 Conversion (%)
405	13.8	93
405	3.8	74
912	13.8	86
1013	3.8	72
1419	13.8	78
1723	3.8	64
2027	13.8	72

It was seen that increased pressure had a strong negative effect on methane conversion percentage. Cao et al. [39] also looked at an unconventional catalyst bed configuration whereby the catalyst coated FeCrAlY was arranged in a saw-tooth pattern through the reactor. This caused the reacting flow to be forced through the catalyst bed multiple times. Modeling and experiments demonstrated increased methane conversion using the conventional design of the catalyst beds confined to the walls.

Johnson et al. [29] also tested a Rh catalyst, but utilized a different substrate made from a porous ceramic. Two different catalyst loadings were tested in this configuration, one with 3.7% Rh weight loading, and one with 10% Rh weight loading. The effects of temperature on both catalyst loadings are shown in Fig. 2.4. The experiments were performed with a steam-methane ratio of 1 and a residence time of 27 ms.
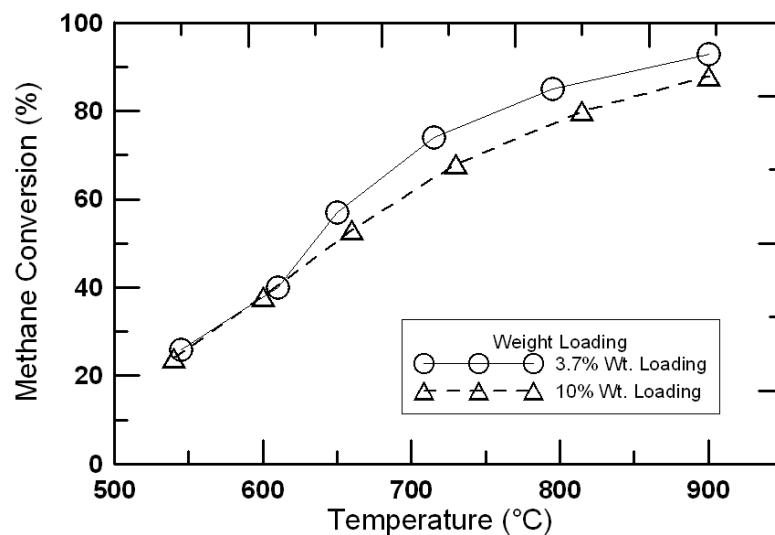
Fig. 2.4: Methane conversion by temperature (adapted from [29])

Both catalyst beds were tested for deactivation at the same conditions identified above, but with a stable temperature of 900°C. The results of 100 hours of testing on each catalyst bed are shown in Fig. 2.5.
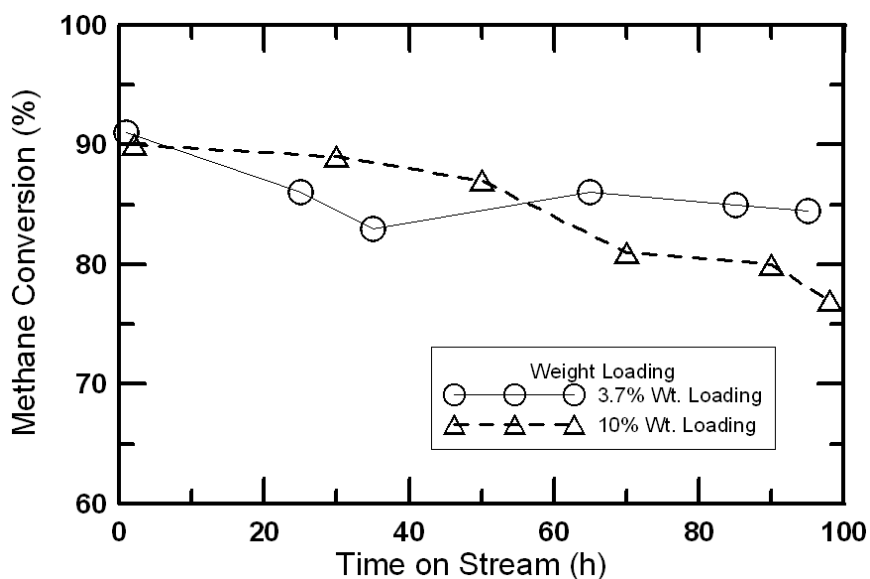
Fig. 2.5: Catalyst stability testing for two catalyst loadings (adapted from [29])

Both experiments demonstrated the superiority of the lighter catalyst loading, which was counterintuitive. Microstructural analysis of both catalyst beds post-testing revealed

increased sintering of the catalyst bed with the higher loading, suggesting that there is an ideal loading density to maximize methane conversion.

The research conducted by Alkhaldi [35] was the only work that could be located documenting steam-methane reforming in a microchannel using Pd as a catalyst. Even though a different catalyst substrate was used than in the present work, Alkhaldi's work proved instrumental in guiding the experimental design. The experiments were conducted at atmospheric pressure and examined methane conversions at temperatures ranging from 630 – 1000°C with steam-methane ratios of 4.8 – 8.1. Changes in density of the flow were not accounted for during the testing, causing the residence time to vary. The results of all steam-methane reforming experiments conducted by Alkhaldi [35] are shown in Fig. 2.6.
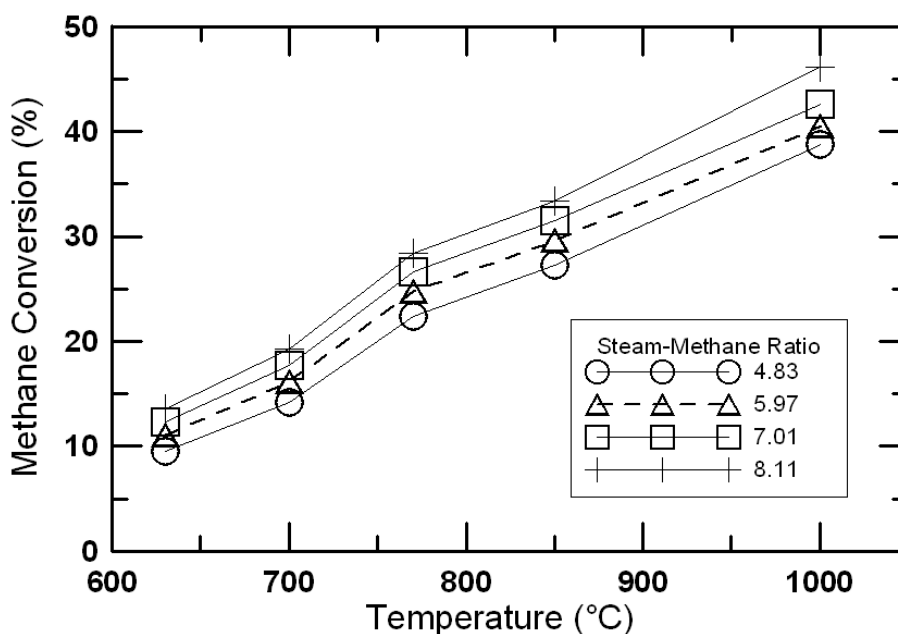
Fig. 2.6: Effects of temperature and steam-methane ratio on CH_4 conversion [35]

Residence times for these experiments ranged from 27 – 42 ms, with higher steam-methane ratios having larger residence times at a given temperature. Similarly, for a given steam-methane ratio, higher temperatures produced smaller residence times. The data as they are presented suggest a slight increase in methane conversion with an increase in steam-methane ratio. There is also a strong linear dependence of methane

conversion percentage to reaction temperature with the exception of one data point at 760°C.

All of the above mentioned literature on microchannel steam-methane reforming helped guide current research efforts discussed herein by providing insights into the expected responses to input parameter variations as well as influencing experimental design.

2.3 Solar Thermal Production of Hydrogen

Solar energy has the advantages of being renewable, clean, plentiful in many areas, and inexhaustible. Concentrating apparatus still require large capital investments, but are a well developed, robust technology. There are several routes of hydrogen production using solar energy: thermolysis, solar cracking, and reforming, all of which are subjects of current research endeavors. An in-depth review and assessment of the different pathways of solar hydrogen generation has been outlined by Steinfeld [40]. The work examined herein will focus on the solar thermal steam reforming of methane.

A concentrated effort has been underway by the European Union in the form of a project known as SOLREF (Solar Steam Reforming of Methane Rich Gas for Synthesis Gas Production). This project builds upon research completed by Moller et al. [41] on the SOLASYS project (Solar Upgrading of Fossil Fuels). The SOLASYS project was a small scale (200-300 kW total solar input) test facility coupled with a detailed cost analysis, whereas the SOLREF project aims to build upon this research and develop a pilot plant with 400 – 500 kW total solar input to bring solar thermal steam-methane reforming close to industrialization [42]. The SOLREF project began in 2004; no publications documenting the progress or results of this project could be located.

The general volumetric receiver design that has been considered in previous reforming research [43-46] is illustrated in Fig. 2.7.
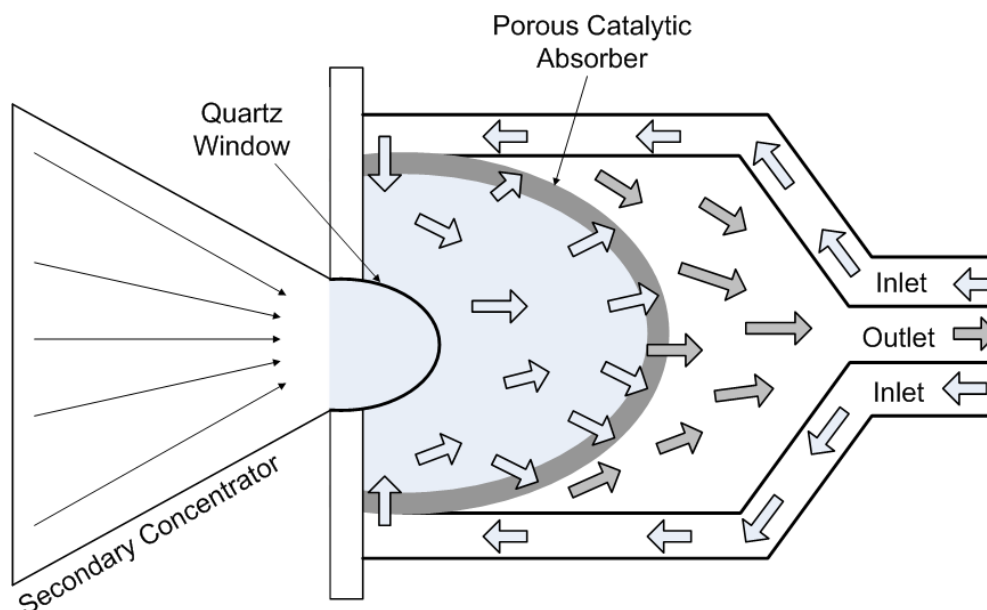
Fig. 2.7: Schematic of volumetric solar receiver/reformer

This receiver consists of a counter-flow heat exchanger leading into an insulated reactor where the reactants are preheated and fed into the reaction cavity which is housed behind a quartz window. The reactants flow through a porous membrane which has been treated with a catalyst; this usually consists of Rh supported on an α-alumina substrate [40]. The solar radiation is directed through the aperture of the receiver and onto the ceramic surface, thereby heating the catalyst directly. Several problems with this design have been encountered. The quartz window necessary to keep the reactants inside the reactor is not entirely transparent. The transmittance for a one centimeter thick piece of optical grade fused quartz at the wavelength of peak solar irradiation (~ 600 nm) is about 92% [47]. Additionally, the wavelength range of virtual transparency (transmittance > 85%) is reduced at higher temperatures [48]. Undesirable gas-phase reactions could quickly lead to carbon accumulation on the inside of the quartz window, further inhibiting transmittance. In addition to transmittance problems, the non-uniform heat flux distribution present on the catalyst surface has led to problems with intensive coking due to operation at non-optimum conditions [44].

The work considered in this research is based on a "windowless" receiver configuration designed to take advantage of the non-uniform heat flux profile, effectively eliminating the two previously mentioned problems.

3. OVERALL DESIGN AND OBJECTIVES

Development of clean methods of hydrogen generation from fossil fuels is an essential step towards building a carbon-neutral "hydrogen economy". Using solar energy to efficiently generate hydrogen from methane could prove to be an important building block of this overall process. This research takes an alternative approach to the standard solar receiver/reactor design by investigating the operational parameters associated with a microchannel exposed to a varying heat flux profile (as would be seen on the inside of a solar receiver) (Fig. 3.1).
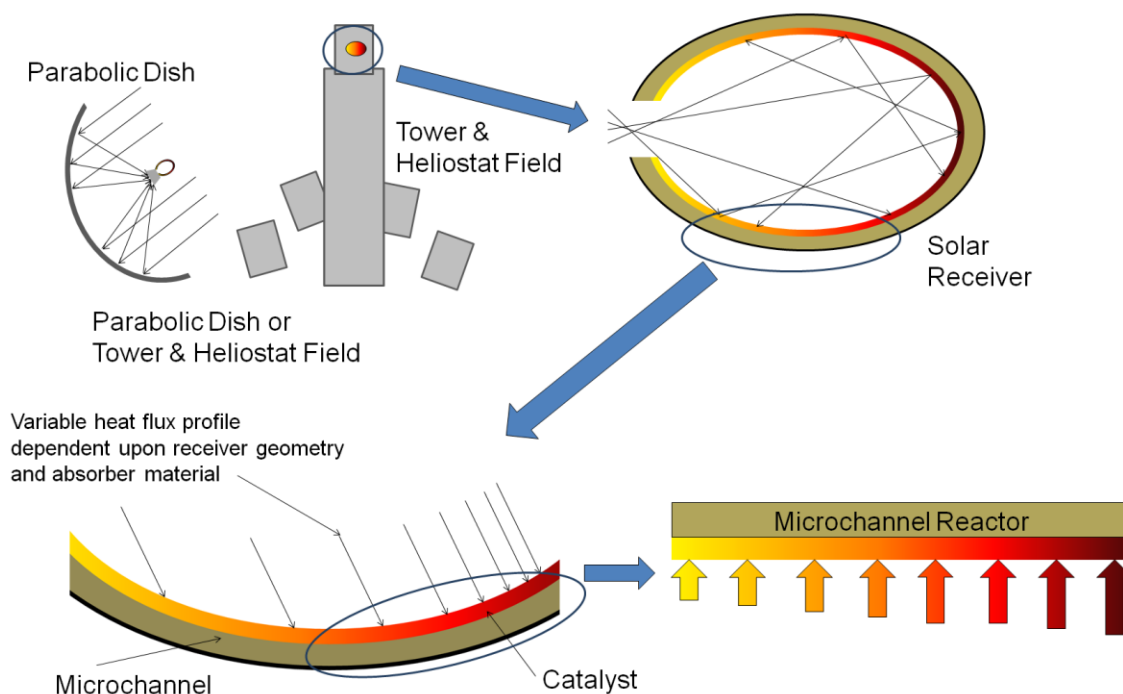
Fig. 3.1: Overall design concept

The inside of the reactor would be lined with a high temperature absorptive material. The shape of the solar receiver cavity could be designed to provide an optimum heat flux profile within the reactor. No solar receiver was built during this research; instead, a single wide aspect ratio microchannel was constructed as an initial test facility to study

the effects of the varied temperature profile, such as would be present inside a solar receiver. This presents a first step towards designing a solar receiver for the optimal production of H_2 through steam-methane reforming.

The curved surface on the inside of the receiver was simulated experimentally using a flat microchannel. An array of individually adjustable propane torches was used to provide a variable heat flux input along the length of the microchannel in order to simulate conditions present along a reactor wall.

The objective of this research was to provide calibration and experimental validation of a computational fluid dynamics (CFD) numerical simulation of a reacting flow through a microchannel. The numerical simulation work was conducted concurrently with the research herein by Peterson [1]. This was to be accomplished by accurately characterizing the catalyst reactivity through perturbations of temperature, steam to methane ratio, residence time, pressure, and temperature distributions. The results would allow for CFD simulations to be performed investigating optimized heat flux profiles for the steam-methane reforming reaction.

4. EXPERIMENTAL FACILITY

Many factors were considered in the design of the test section. The design requirements for the experimental facility were as follows:

- o Adjustable channel height of less than 1 mm

- o Reactor capable of being disassembled for examination and changing of catalyst beds

- o Laminar flow through reactor

- o Minimized flow fluctuations to eliminate transients

- o Quantifiable longitudinally variable heat flux input

- o Residence time must be less than reaction time and diffusion time

- o Gases must enter reactor pre-heated

- o All H_2O must be eliminated from the outlet stream

- o All high temperature components must reside inside fume hood

In addition, special consideration was given to safety due to the operational temperatures and combustible nature of the working gases. With these considerations in mind, the reactor was designed and constructed as detailed in this chapter.

4.1 Design Considerations for Test Section

Three main design elements were examined to provide insight into the final reactor design. The residence time within the channel had to be such that the reaction would not be carried out to completion; otherwise variations of input parameters would not be evident. Secondly, the channel had to be constructed to receive a longitudinally variable heat flux input. Thirdly, the reactor would need to be designed to withstand the elevated temperatures anticipated during the testing. All three of these design considerations are examined here.

4.1.1 Time Scales

In designing the test section, it was necessary to account for factors that would fundamentally influence the operation of the reformer. Three different time scales had to be considered in the design process: residence time, diffusion time, and reaction time. The geometrical configuration of the reactor combined with the flow metering equipment would serve to define the residence time (Eq. (4.1)) of the channel.

$$t_{res} = \frac{l}{U} \tag{4.1}$$

From the onset, it was desired to take advantage of the increased heat transfer and reduced diffusion times provided by utilization of a microchannel. Consequently, the channel height was limited to less than 1 mm during the design stage.

As the methane is consumed by the reaction, additional molecules of CH_4 need to diffuse to the catalyst surface for the reaction to continue. Microchannels greatly reduce the diffusion length, allowing for much smaller residence times. As the species composition changes through the reactor, slight variation in diffusivity will occur.   For simplicity, the analysis of the diffusion length time scale only looked at methane diffusing in steam. The diffusion time was defined as follows

$$t_{dif} = \frac{h_g^2}{D} \tag{4.2}$$

where h_g is the channel height and D is the diffusion coefficient. The diffusion coefficient was calculated using the formula from Kuznetsov [49], which is a simplified version of the work outlined by Fuller (1969) [50].

$$D = \frac{9.99 \times 10^{-5} \, T^{1.75}}{P} \tag{4.3}$$

The diffusion times were evaluated over a wide range of temperatures and possible channel heights to assess where diffusion limited reactions would be present (Fig. 4.1). The diffusion time increases greatly as the channel height is increased. To avoid a diffusion limited process it would be necessary to operate the reactor with residence times well above the calculated diffusion time.
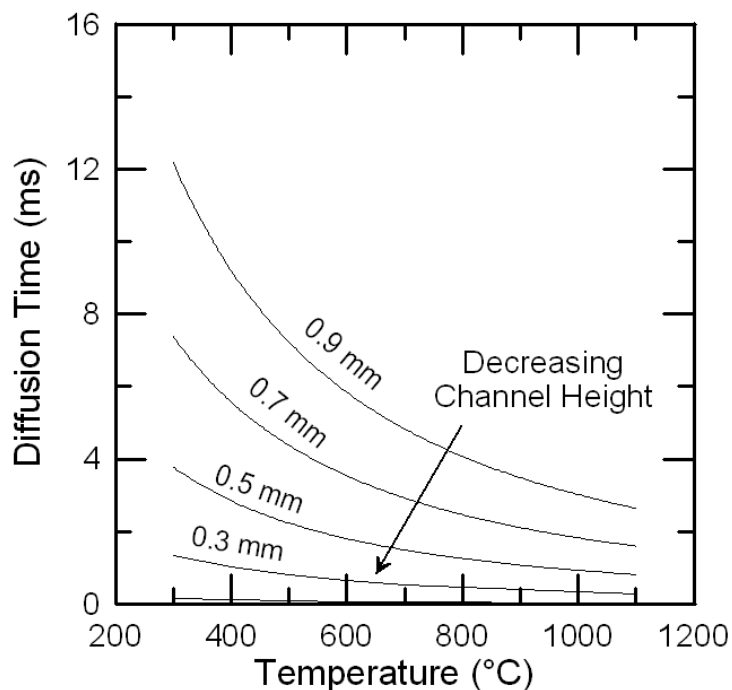
Fig. 4.1: Diffusion times for different channel heights over varying temperatures

The reaction rates were slightly more challenging to obtain. The reaction rate constants are generally experimentally obtained and are highly sensitive to catalyst type, loading, and configuration. During the initial design process, residence times and methane conversion percentages over a Pd catalyst presented by Alkhaldi [35] were used to define a desired residence time range of 5 to 50 milliseconds.

4.1.2 Discrete Heating Zones

The vast majority of research on steam reforming microreactors involved operating at isothermal conditions in a precisely controlled environment. Microchannels are well suited for isothermal operation due to their limited size and length. The microchannel in this experiment needed to be long enough to be non-isothermal and receive heat flux from discrete heating elements along its length. Several electrical heating options were investigated including cartridge heaters and high temperature microheaters. Cartridge heaters are relatively inexpensive and easily controlled, but the maximum sheath temperature of commercial Incoloy® cartridge heaters is 750°C, far less than what was

required. High temperature microheaters from Micropyretics Heaters International Inc. (Cincinnati, OH), were considered as an attractive option with maximum temperatures of 1900°C. The cost of the heaters and control electronics with this option proved excessive with the projected cost at over $5,000 per heated section.

To achieve the required temperatures at a reduced cost, it was decided to use direct flame impingement as a heating source. Bunsen burners did not provide heat at the temperature required, subsequently several options were tested utilizing compressed propane. Preliminary tests were conducted in order to examine flame interaction to determine appropriate torch spacing. The diameter of each torch was 12.7 mm (0.50 in), and torch spacing (center – center) of 19 mm (0.75 in) produced no significant flame interactions as seen in Fig. 4.2.
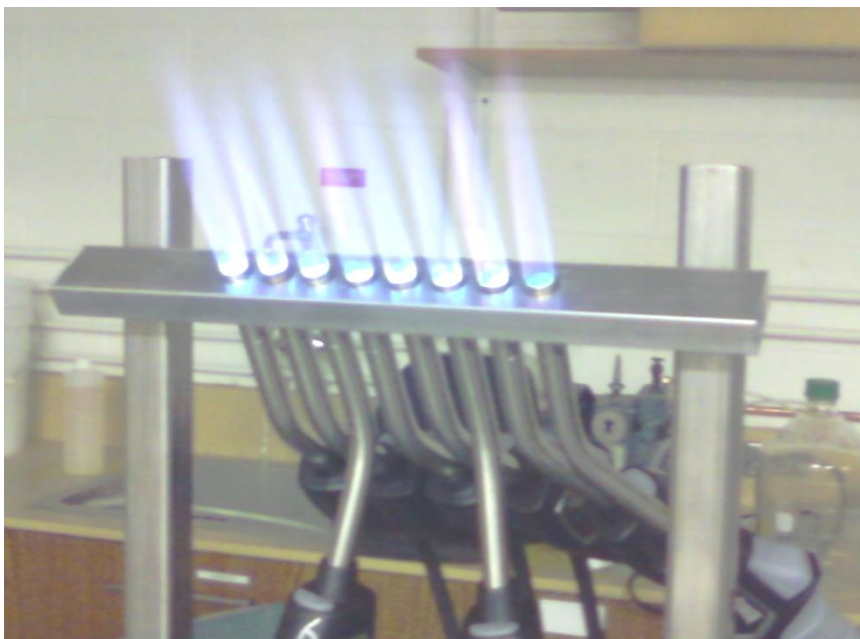
Fig. 4.2: Torch flame proximity test

The torches would provide heat to the channel by way of conduction through the bottom surface of the reactor. In order to quantify the heat flux entering each section of the reactor, three thermocouples were oriented in-line with the primary direction of heat transfer with a 5.08 mm (0.20 in) separation distance. In addition to quantifying the heat flux in each section, extrapolating the thermal gradients present in the heating block

provided a basis for calculating a surface temperature. A diagram of a single heating section is shown in Fig. 4.3.
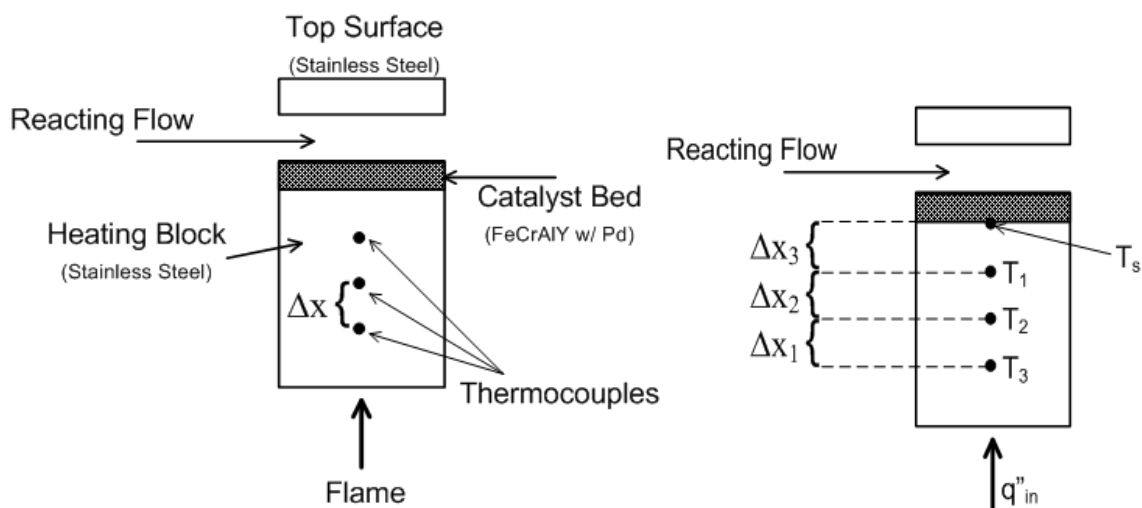
Fig. 4.3: Single heating section of reactor

The surface temperature was calculated using the temperature gradient between the two thermocouples closest to the microchannel using the following equation

$$T_s = T_1 + \frac{T_1 - T_2}{\Delta x_2} * \Delta x_3 \tag{4.4}$$

The locations of the measurements in Eq. (4.4) are identified in Fig. 4.3.

4.1.3 Elevated Temperatures

The reaction rate along with the equilibrium concentrations of the outlet gases is highly dependent upon temperature. The equilibrium concentration of all reactants as a function of temperature is shown in Fig. 1.1. To maximize the hydrogen yield, it is necessary to carry out the reforming process at temperatures above 700°C, preferably closer to 800°C. Testing at temperatures up to 950°C was desired in the test apparatus which led to concerns regarding materials selection.

Superalloys such as Inconel have high melting temperatures and excellent corrosion resistance at elevated temperatures, but can be exceedingly difficult to machine. All of the machining was performed in-house, thus it was preferable to use a material with a greater degree of machinability. With a melting temperature of 1400°C, type 304

stainless steel was chosen as a suitable material from which to construct the microchannel. Much of the oxidation resistance of the stainless steel would be lost once exposed to temperatures greater than 900°C, but the oxidation was expected to be limited to the exterior of the reactor.

The high temperatures necessary for the reaction complicated the task of sealing the reactor. Permanent sealing techniques such as diffusion bonding or welding would have provided a seal capable of withstanding elevated testing pressures, but such sealing techniques would have prohibited the examination and swapping of catalysts. A commercial gasket of the type commonly found in vehicle exhaust systems was used due to availability. A combination of high temperature alumina silica ceramic (McMaster-Carr pn 9379K93) and Pyrogel XT aerogel sheeting (Aspen Aerogels) was used to insulate the reactor.

4.2 Final Reactor Assembly

The final design of the reactor assembly is shown in Fig. 4.4 and Fig. 4.5. Heat input was provided by nine Bernzomatic® torches impinging on the bottom surface of the reactor. The initial two torches acted as preheaters for the reactor, whereas the subsequent seven torches impinged on the surface corresponding to the location of the catalyst and provided heat for the reaction. Half of the preheater zone had the same thermocouple arrangement as the catalyst zone, whereas in the other half the flame impinged directly on the reactor wall, thereby reducing heat transfer resistance. The microchannel height was formed by a high temperature exhaust gasket, or shim, compressed between two pieces of stainless steel to form a large aspect ratio channel. The catalyst was contained on a porous FeCrAlY felt insert which is discussed in Ch. 5. The channel was held together with 30 8x32 stainless steel bolts distributed around the perimeter of the channel. It was desired to distribute the compressive force as much as possible to minimize the potential for leaks in the system. To eliminate conduction between heating zones, 0.8 mm (1/32 in) slits were cut between each heating zone creating an insulating air gap. Detailed drawings of the reactor components with measurements are located in Appendix A.
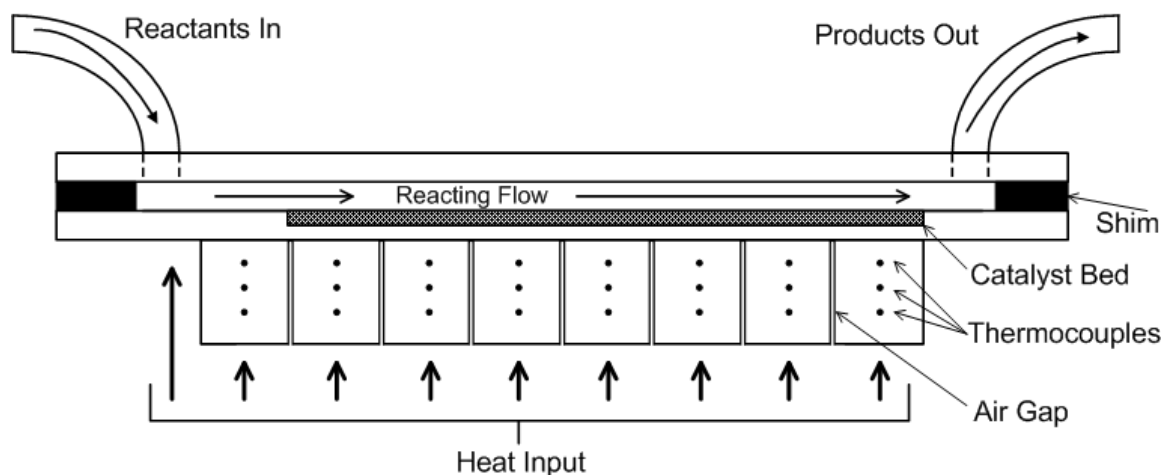
Fig. 4.4: Cross sectional view of reactor
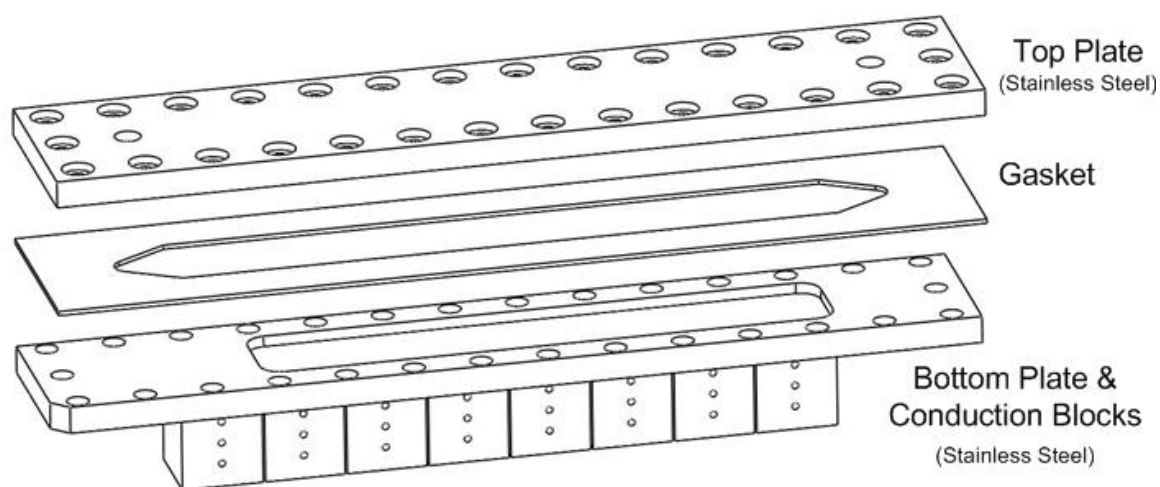
Fig. 4.5: Exploded view of reactor assembly

The microchannel height was determined by measuring the thickness of the stainless steel walls forming the top and bottom of the reactor prior to assembly and subsequently measuring the thickness of the entire assembly after all bolts had been tightened. The catalyst bed was slightly taller than the cavity in the base of the reactor, causing the channel to be further restricted. A diagram illustrating the channel height measurements is shown in Fig. 4.6.
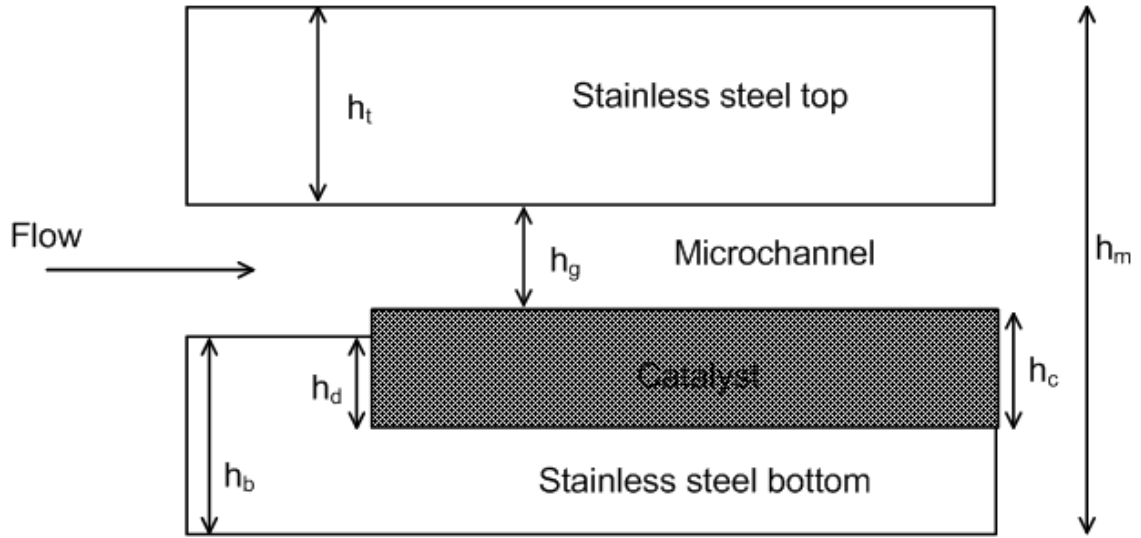
Fig. 4.6: Microchannel height measurements

The microchannel height was calculated as follows

$$h_g = h_m - (h_t + h_b) - (h_c - h_d) \tag{4.5}$$

The height of the catalyst bed used in this work was 3.175 mm (0.125 in). The final dimensions of the microchannel were 133.6 mm (5.25 in) in length, 19 mm (0.75 in) in width, and a height between 0.70 – 1.067 mm (0.028 - 0.042 in).

4.3 Operational Parameters of Reactor

During the design stage, it was necessary to look at a multitude of geometric configurations and flow parameters in order to ensure that the reactor would be operating in a range that would allow slight variations of output gases to be observed. The effects of varying the temperature, steam-methane ratio, pressure, and channel height were all investigated. All calculations were performed for a non-reacting flow, taking into account only the conditions at the inlet of the reactor. The parameter over which all variables were examined was the mass flow rate of methane. The mass flow controller to be used in the experiment had a flow range of 0.15 – 7 g/min, but only the lower end of this flow range was used in the experiments.

4.3.1 Variation of Temperature

The effects of varying temperature in the channel were analyzed through the range of expected temperatures (500 – 1000°C) (Fig. 4.7). Residence time in the channel was calculated using the channel length (l) and velocity (U) as follows:

$$t_{res} = \frac{l}{U}$$ (4.6)
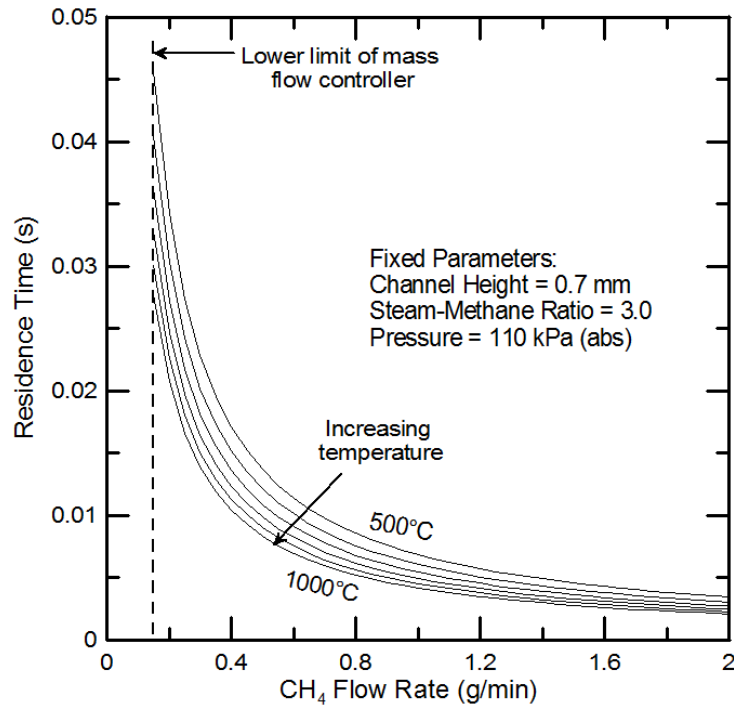
Fig. 4.7: Residence time effects of temperature variation

Increasing surface temperature (and thereby gas temperature) caused the density of the mixture to decrease, thereby producing decreased residence times for a given flow rate. The magnitude of variation of the residence time was greatly decreased at higher methane flow rates. The maximum residence time at 800°C was predicted to be 33 ms with a methane flow rate of 0.15 g/min. By increasing the temperature from 500°C to 1000°C the residence times were reduced by 40% for all flow rates.

For the experiments to coincide with the numerical simulations being conducted by Peterson [1], it was necessary to ensure that the flow stayed within the laminar flow

regime. In channel flow, the transition Reynolds number is 2300 [51]. The expected Reynolds number inside the reactor was calculated from Eq. (4.7) and is plotted by methane flow rate for multiple temperatures in Fig. 4.8.

$$\mathrm{Re} = \frac{\rho_{mix}\, U(2h)}{\mu_{mix}} \tag{4.7}$$
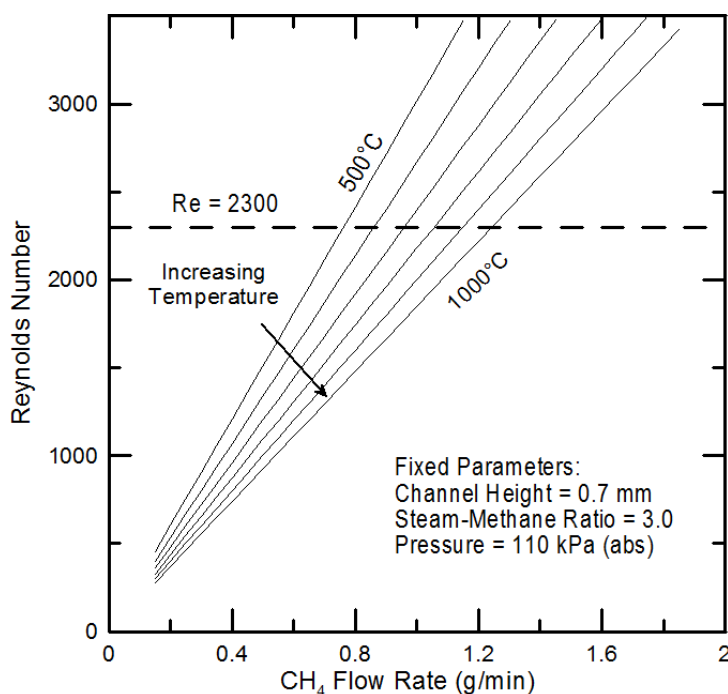
Fig. 4.8: Reynolds number effects of temperature variation

At a reactor temperature of 800°C, laminar flow would be maintained at a flow rate of less than one g/min of CH_4, however at a reduced temperature of 500°C, the transitional flow regime would be encountered at 0.75 g/min of CH_4. An increase in temperature causes the density to decrease and the viscosity of the mixture to increase. These factors combined have a greater influence on the Reynolds number than does the corresponding increase in velocity, thereby causing a decrease in the Reynolds number with an increase in temperature.

4.3.2 Variation of the Steam-Methane Ratio

The reactor temperature was set at 800°C and the steam-methane ratio was varied from 2 to 4 to examine the effects on residence time (Fig. 4.9) and the Reynolds number (Fig. 4.10).
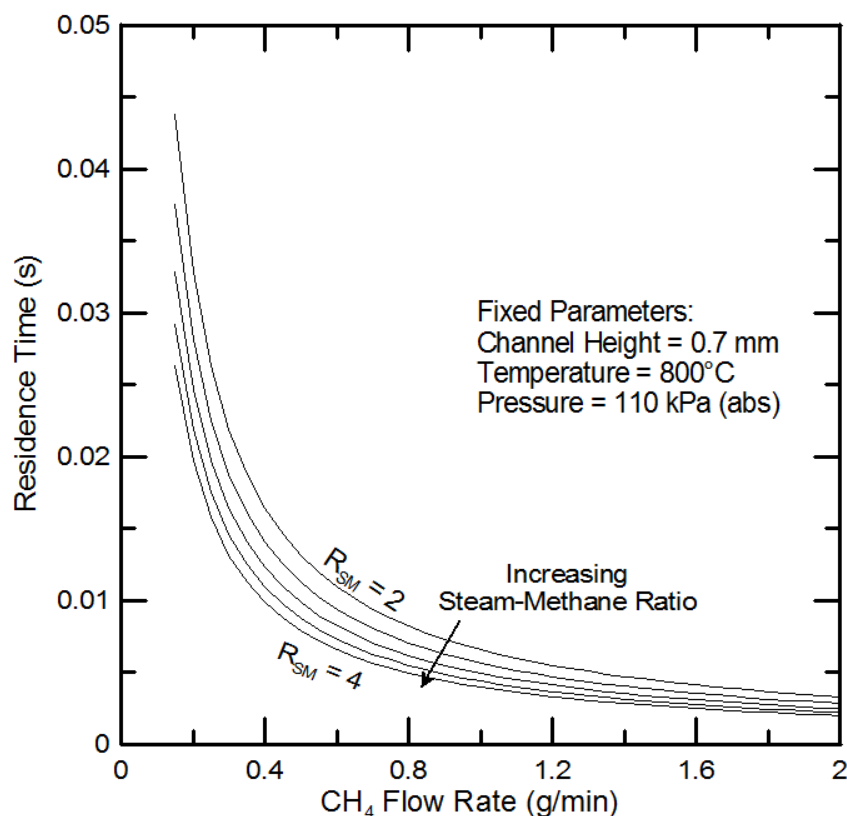
Fig. 4.9: Residence time effects of steam-methane ratio variation

Increasing the steam-methane ratio increases the total mass flowing through the system, thereby reducing the residence time through the channel. By decreasing the steam-methane ratio from 4 to 2, a 66% increase in residence time was evident over all flow rates. If CO and H_2 are the sole products of steam-methane reforming, the stoichiometric ratio of H_2O to CH_4 is unity. Carbon dioxide is formed during the reaction as well (less at higher temperatures), thus causing a temperature-dependant stoichiometric ratio generally between $1.2 - 1.5$. Operating a reactor at steam-methane ratios close to the stoichiometric ratio would be beneficial by increasing the residence time for a given

methane flow rate. This would increase conversion, but it would also increase the potential for coking and catalyst deactivation.
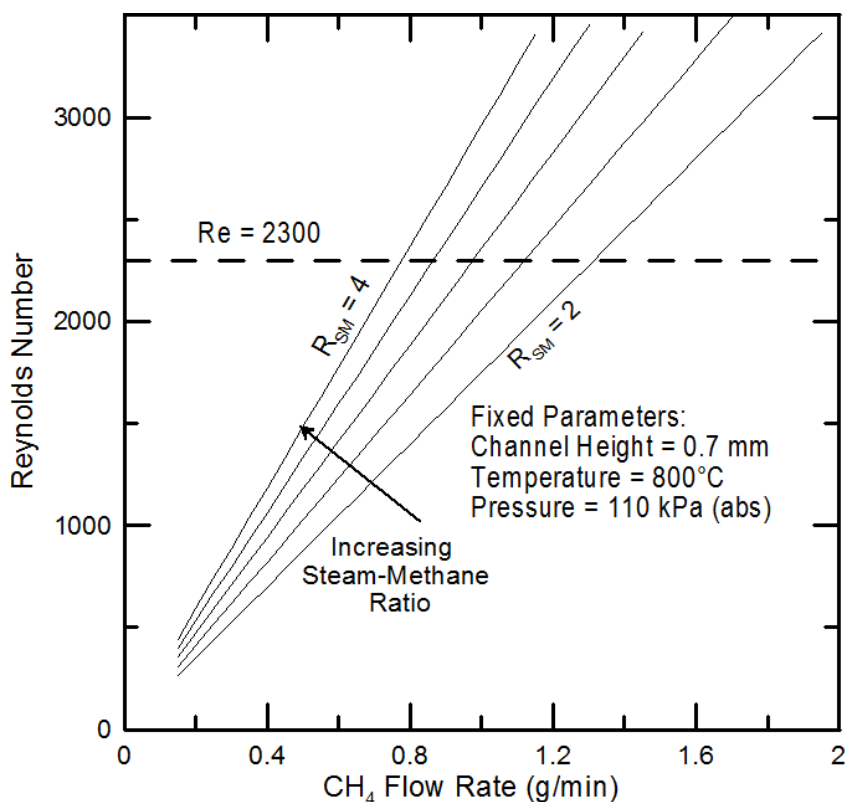
Fig. 4.10: Reynolds number effects of steam-methane ratio variation

The Reynolds number through the channel increases with increased steam-methane ratios as seen in (Fig. 4.10). Transitional Reynolds numbers will be encountered with elevated steam-methane ratios at flow rates of 0.75 g/min of methane.

4.3.3 Variation of Pressure

Industrial reactors operate at greatly elevated pressures of 20 – 40 bar [52]. The increased density allows for greater mass flow rates while maintaining a set residence time. The reactor used in this study did not employ a robust enough sealing method to allow for such pressures, so only the effects of pressure variations up to 400 kPa were investigated. Increasing the pressure by a factor of two caused the density to double,

thereby producing a corresponding increase in residence time by the same factor (Fig. 4.11).
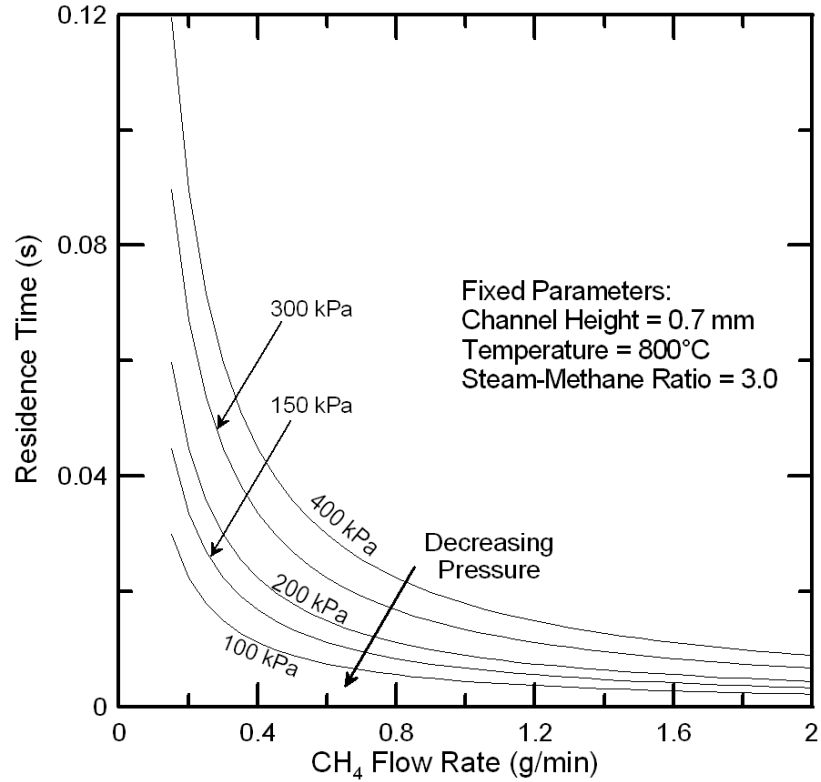
Fig. 4.11: Residence time effects of pressure variation

The Reynolds number was unaffected by changes in pressure. This can be seen by expressing the velocity through the channel in terms of a mass flow rate.

$$U = \frac{\dot{m}_{mix}}{\rho_{mix}\,(w * h)} \qquad (4.8)$$

Substituting Eq (4.8) into Eq (4.7) yields an expression for the Reynolds number independent of density, and therefore pressure (Eq. (4.9)). The viscosities of all constituents were independent of pressure and varied only with temperature.

$$\text{Re} = \frac{2\dot{m}_{mix}}{w * \mu_{mix}} \qquad (4.9)$$

4.3.4 Variation of Channel Height

One of the advantages of the modular design of the reactor was the ability to swap out different shims, effectively changing the channel height in the reactor. Lower residence times (<10 ms) at moderate methane flow rates could be readily explored by reducing the channel height (Fig. 4.12).
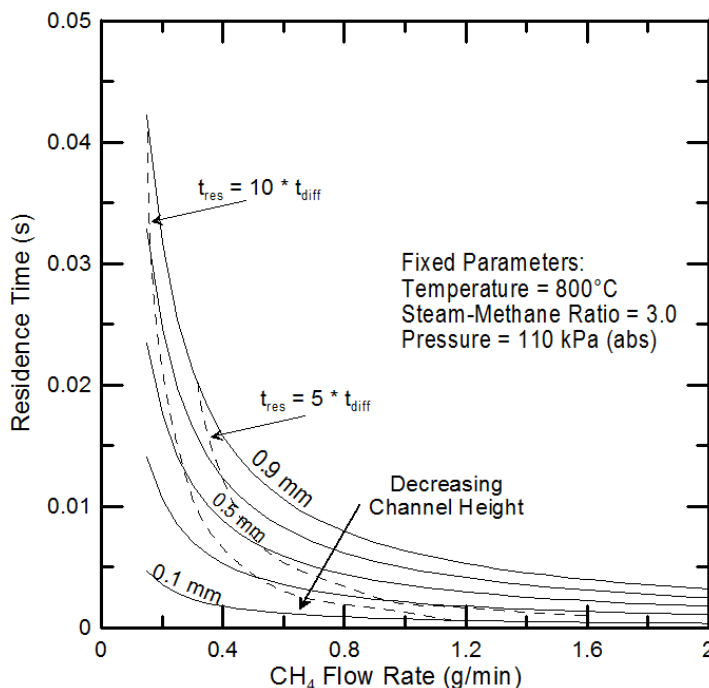
Fig. 4.12: Residence time effects of channel height variation

While keeping the channel height sub-millimeter, the upper limit of residence time for the reactor was calculated to be on the order of 50 ms. The residence time and diffusion time were calculated using Eq. (4.1) and Eq. (4.2) respectively. The dashed lines in Fig. 4.12 represent operational points where the residence time would be equal to five and 10 times the diffusion time. This indicates that the diffusion time scale becomes less limiting as the microchannel height is decreased. The Reynolds number variation for perturbation of channel height was analyzed and showed that for a set methane flow rate, the Reynolds number was constant. The reasoning for this is readily apparent from the formulation of Eq. (4.9).

4.4 Test Facility

The reactor was integrated into a test facility as shown in Fig. 4.13. Monitoring instrumentation is shown in green. All open flames and components at elevated temperatures were located inside a vent hood as indicated by the dashed line in Fig. 4.13.
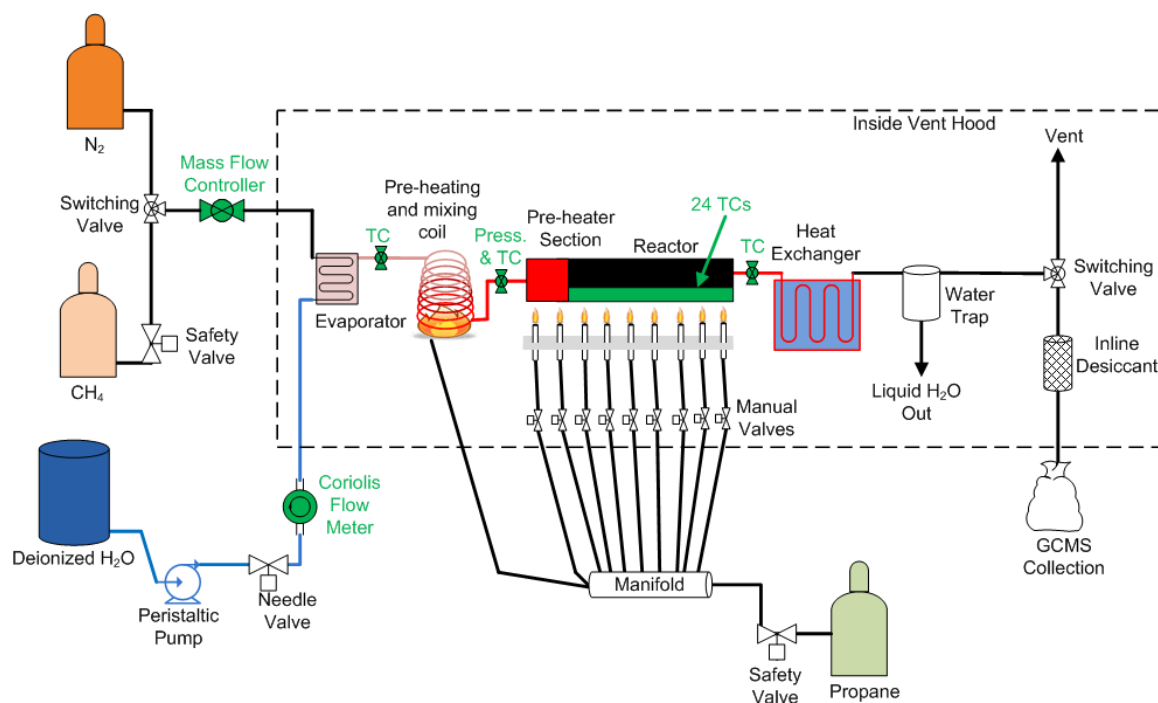
Fig. 4.13: Test facility schematic

All components of the test facility carrying the products and reactants are connected using 6.35 mm (0.25 in) OD 316 stainless steel tubing with a wall thickness of 0.89 mm (0.035 in) with a resultant inside diameter of 4.57 mm (0.18 in). Nitrogen and CH_4 streams are fed to a switching valve and controlled using a common mass flow controller. The experimental design was such that either N_2 or CH_4 could be fed through the system at a time, but not both. Deionized H_2O is pressurized using a peristaltic pump capable of 689 kPa (100 psi) and controlled using a 16-turn needle valve. A Coriolis flow meter measures the H_2O flow rate before it is injected into the evaporator which is further described in Section 4.2.1. From the evaporator, the steam/gas mixture flows through a 0.3 m (1 ft) insulated section to a 3 m (10 ft) coil of tubing situated on top of a 7.6 cm (3

in) diameter propane burner. This section (labeled as "Pre-heating and mixing coil" in Fig. 4.13) heats the gas mixture to near the inlet temperature (~550°C), and allows the gases time to diffuse into a homogeneous mixture. Once the gases are well mixed and pre-heated, they flow through a short (~15 cm) section of insulated tubing configured with two monitoring ports (temperature & pressure) before flowing into the reactor. The product gases exit the reactor at a greatly elevated temperature (~700°C). The gas stream needs to be cooled in order to condense and remove the remaining steam. A counter-flow shell and tube heat exchanger was designed and built (Fig. 4.14). City water at approximately 10°C was used for the cold stream. Prior to entering the heat exchanger, the reactants flowed through 61 cm (2 ft) of exposed tubing causing an estimated temperature drop of approximately 200°C.
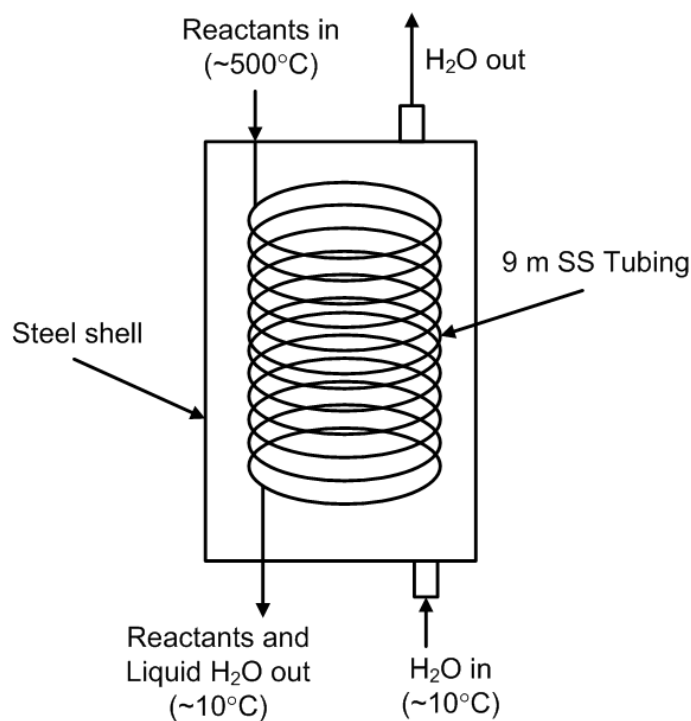
Fig. 4.14: Counter-flow heat exchanger/condenser

The reactant stream contained a large portion of steam that is condensed in the heat exchanger. A downward slope of the interior coils was maintained in order to facilitate liquid water flow out of the condenser. The condensed water was removed from the

product stream as shown in Fig. 4.15. The separation is gravity-driven, whereby the water precipitates out into a collection hose and the "dry" products continue through the flow loop. The simple design of this water trap was chosen to avoid any recirculation zones in the flow loop which would have been present if a large diameter/large volume water trap were to have been used.
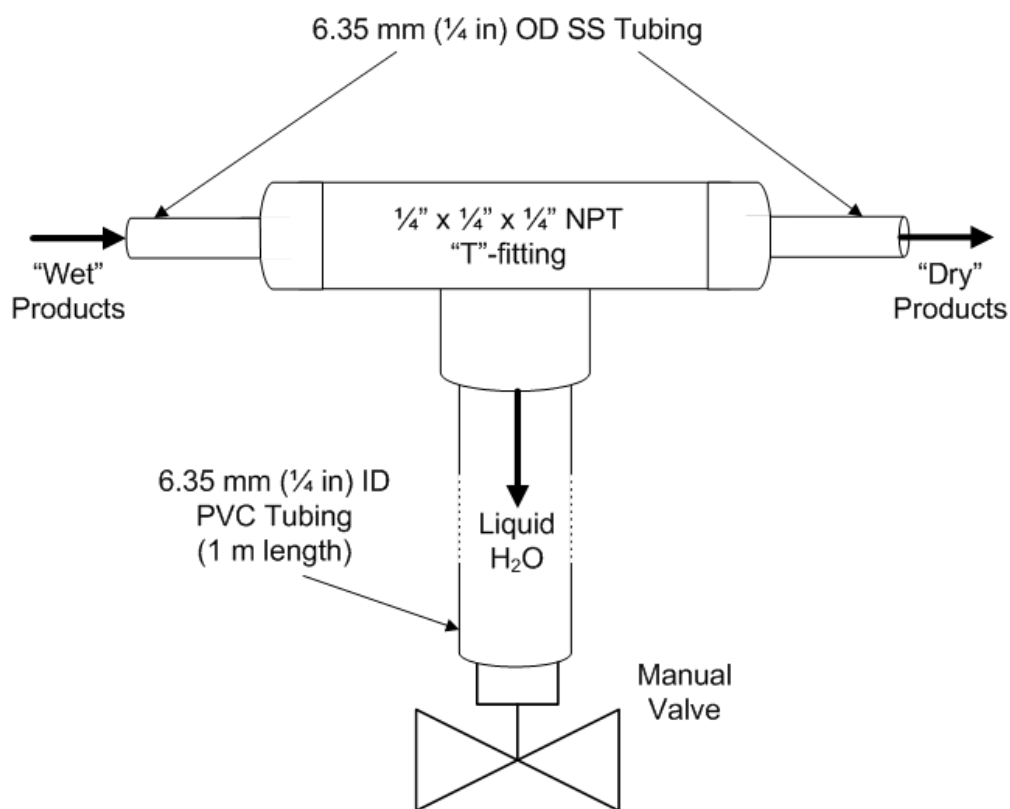
Fig. 4.15: Schematic of the water trap

The "dry" products are then either sent through a desiccant cartridge to remove any remaining water vapor and collected in sample bags for analysis in a gas chromatograph (GC), or vented to the atmosphere. Both exits from the flow the flow loop were fitted with 20 gauge hypodermic needles with inner diameters of 0.6 mm. The needle situated after the desiccant cartridges was used for injection of the product gases into the sample bags, whereas the needle on the vent was used to provide uniform backpressure to the experiment regardless of where the gas was exiting the system.

4.4.1 Propane Delivery

A standard 9 kg (20 lb) propane cylinder was used to fuel all burners. A full cylinder provided a run time of approximately 12 hours. All propane delivery lines to the torches were unregulated and provided a variable temperature dependant pressure of 621 – 827 kPa (90-120 psi). Each torch had a regulator, which provided a uniform pressure of 345 kPa (50 psi) to all torches.

4.4.2 Evaporator Design

The component that required the most design iterations was the evaporator. During the evaporation process at atmospheric pressure, water expands to approximately 1000 times its original volume. Consequently, any flow inconsistencies are greatly amplified and directly observable through dramatic pressure variations in the test section. Thus, the evaporator had to be capable of generating steam at a steady rate while avoiding minor transients as much as possible. The final evaporator design allowed for a maximum water flow rate of 21 g/min with a total power consumption of 1250 W. The final design of the evaporator consisted of a hollowed out aluminum cylinder (76.2 mm (3 in) in diameter and 152.4 mm (6 in) in length) with five 250 W cartridge heaters fitted in the base (Fig. 4.16). The cartridge heaters were maintained at a desired temperature using a PID controller connected to a solid state relay. A K type thermocouple located between the cartridge heaters and the bottom of the cavity provided the set temperature for PID control. The cap was sealed using eight 10x32 bolts and an O-ring. Three fittings were installed in the lid of the evaporator; a gas inlet for the nitrogen/methane, a separate inlet for the liquid water, and a common outlet. The water inlet fitting was a 1/16" Swagelok® pass-through tubing adapter with a 100 mm (4 in) section of 1.59 mm (0.0625 in) OD, 0.51 mm (0.02 in) ID stainless steel tubing.
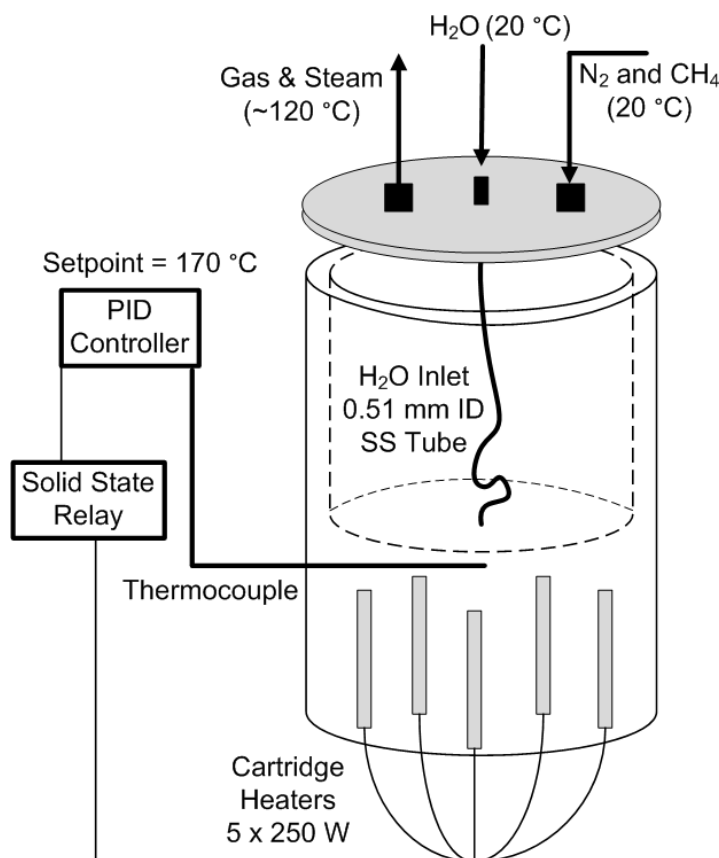
Fig. 4.16: Evaporator schematic

Surface tension effects become very prominent when dealing with small volumes of water and resultant droplet formation would cause undesirable flow transients. A spray nozzle or atomizer would have circumvented the droplet formation problem, but would have narrowed the range of operation of the system. To avoid droplet formation at the exit of the water inlet, the tube was configured such that it was "spring-loaded" against the base of the cavity of the evaporator. In this configuration, as soon as the water exits the inlet tube it spreads over the heated surface. This configuration produced a near-constant flow of steam and gas to the mixing coil.

4.4.3 Safety and Preparedness

Safety was of great concern during this experiment due to the combination of high temperatures, open flames, pressurized flammable gases, and the proximity of water and electrical equipment. The greatest foreseeable hazard was a rupture of a high pressure

propane delivery hose. In addition to segregating the high temperature components inside a fume hood, two fire extinguishers were procured and located near the experiment. It was desired to have a remote method of stopping all flammable gas flow to the experiment, should an accident occur. The CH_4 and propane feeds were fitted with 12 V normally-closed solenoid valves connected to a remote stop switch which was located near the laboratory exit, approximately 10 m from the experiment. Experiments were only conducted when two or more people trained on the safety and experimental procedures were present.

4.5 Data Acquisition

The flow path of data from the sensors to the computer is illustrated in Fig. 4.17. The gas chromatograph was housed at a separate location and data were collected on a different computer.
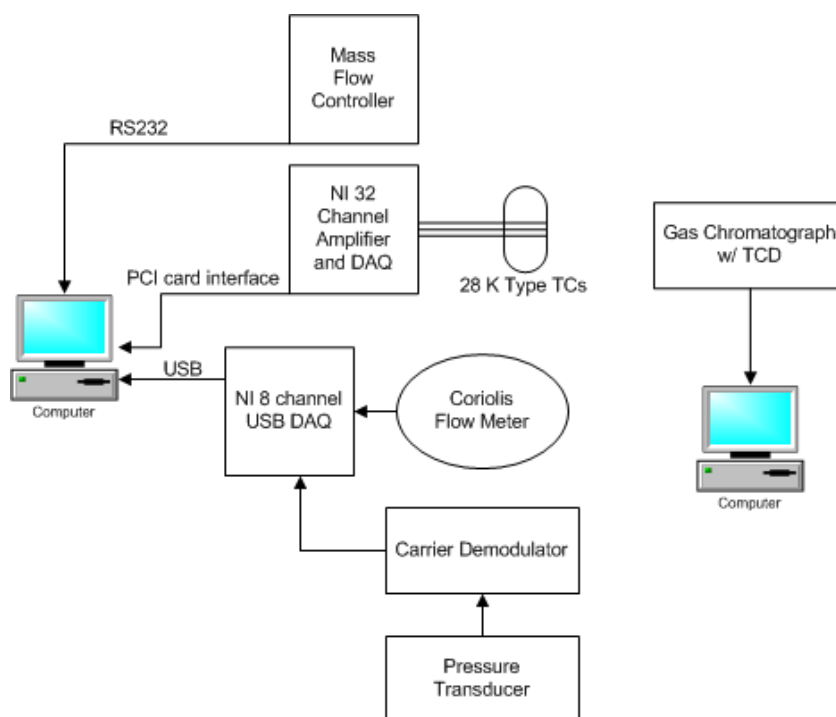
Fig. 4.17: Instrumentation schematic

Data were collected using two digital acquisition (DAQ) modules connected to a Windows PC running LabVIEW 8.5. A LabVIEW virtual instrument (VI) was developed which served to concatenate, display, and store all experimental variables. All data were time-stamped using the time from the computer clock, and stored at a frequency of one hertz. The time of each gas sample was recorded and the gas analysis data was joined into the dataset as part of the post-processing.

4.6 Equipment and Instruments

A summary of the equipment used is provided in Table 4.1. Instruments are listed in Table 4.2.

Table 4.1: Equipment

Item	Model	Qty
Pre-heater Torch	Bernzomatic BZ8250	1
Propane Torches	Bernzomatic TS839	8
Water Pump	Stenner model 85MHP17	1
16-turn Valve	Cole Parmer SN 68246-22	1
PID Controller	OMEGA CNi3253	1
Solid State Relay	OMEGA SSR330DC50	1
Solenoid Valves	AFC Inc. Model 121	2
Desiccant Cartridges	Arrow Pneumatic Mini In-Line	2
Sample Bags	Tedlar - SKC model 232-02 (0.5 L)	20

Table 4.2: Instruments

Item	Model	Range	Accuracy
Thermocouples	OMEGA Super OMEGACLAD XL Type K KMTXL-062U-12 (Qty: 28)	0 - 1335 °C	+/- 0.4% of Reading (>300°C)
Mass Flow Controller	Sierra Smart-Trak C100L	0 - 7 g/min	+/- 0.3% FS + 0.7% reading
Coriolis Meter	MicroMotion Elite CMF010 w/ MicroMotion 2700R Transmitter	0 - 50 g/min	+/- 0.05% of reading
Pressure Transducer	Validyne DP15-40 Transducer w/ Validyne CD15 Carrier Demodulator	0 - 345 kPa	+/- 0.25% of FS
USB-DAQ	NI USB-6009 DAQ	+/- 10 V	+/- 7.7 mV
DAQ	NI SCXI-1000 Chassis NI SCXI-1102 32 channel TC Amplifier NI SCXI-1303 Terminal block	+/- 10 V	0.05% of Reading
Gas Chromatograph	HP 5890 with TCD	0 – 100 %	+/- 1.5% of reading
Scale	Scientech SA 120	0 - 120 g	+/- 0.2 mg

5. CATALYST PREPARATION

The most widely used catalysts for steam-methane reforming are nickel, palladium, and rhodium. Palladium was chosen for this set of experiments due to the expertise available involving palladium nanoparticle synthesis from O.P. Valmikanathan at Oregon State University. The raw materials for synthesis of the catalyst (palladium chloride, sodium borohydride, and dodecanethiol) were purchased from Sigma Aldrich.

5.1 Synthesis

The palladium nanoparticles were synthesized with assistance from O.P. Valmikanathan using a modified form of Brust's method [36,53]. To generate the palladium stock solution, 100 mg of palladium chloride was dissolved in 13 molar hydrochloric acid and diluted with deionized H_2O to 500 ml. Two drops (~40 mg) of dodecanethiol was added to 100 ml of toluene and poured into a round bottom flask. The flask was partially submerged in an ice bath and the mixture was stirred on a magnetic stirrer. Fifty milliliters of the stock palladium solution were added to the mixture along with 50 ml of deionized H_2O forming a biphasic mixture consisting of 100 ml aqueous phase and 100 ml organic phase. The solution was stirred rapidly for 30 minutes.

A reducing solution of 2 mg sodium borohydride and 40 ml deionized H_2O was prepared and situated above the mixture in a burette. The sodium borohydride solution was added dropwise to the mixture over a period of approximately 10 minutes. The mixture underwent a color change during the reduction process from light yellow to black, denoting the formation of palladium nanoparticles. The mixture was then stirred continuously for three hours during which the palladium nanoparticles were transferred from the aqueous phase to the organic phase. The aqueous phase was separated and discarded. Ten iterations of this procedure were necessary to produce a batch of palladium nanoparticles. The resulting solution consisted of one liter of toluene containing nanoparticles produced from 100 mg of palladium chloride (60 mg palladium). This mixture was then evaporated under reduced pressure using a Buchi

Rota-vapor R110 from Brinkman Instruments (Westbury, NY). The original one liter was evaporated to a volume of 40 ml of densely concentrated palladium nanoparticles suspended in toluene.

5.2 Deposition

To enhance the surface area available for nanoparticle deposition, an 85% porous 3.175 mm (0.125 in) thick FeCrAlY metallic felt (FM542) provided by Technetics (www.techneticsfl.com), was used as a catalyst substrate for all experimental beds (except one, which was deposited directly onto the stainless steel channel wall). The FeCrAlY sheet was oxidized at 900°C for four hours in air, causing the aluminum to migrate to the surface and form α-alumina. This procedure has been documented to increase the surface area of the FeCrAlY by a factor of 10 [54]. Scanning electron microscope (SEM) images were taken of the substrate before (Fig. 5.1) and after (Fig. 5.2) the heat treatment process.
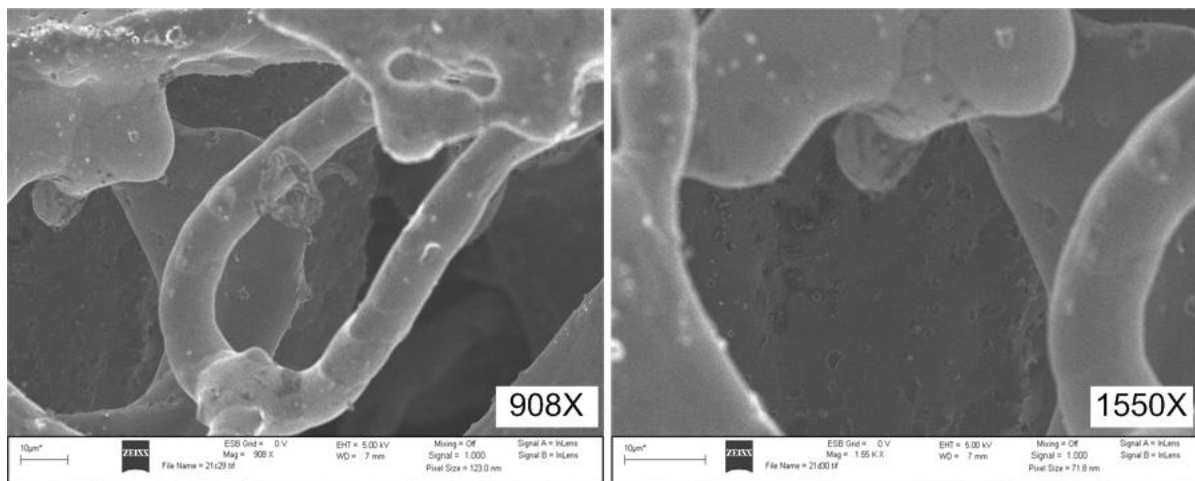
Fig. 5.1: SEM images of FeCrAlY prior to heat treatment
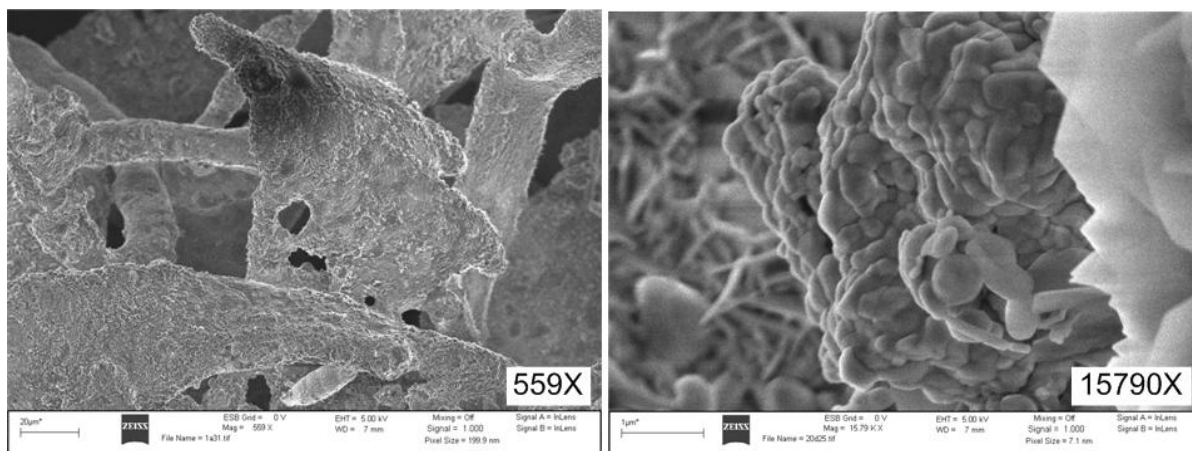
Fig. 5.2: SEM images of FeCrAlY with α-alumina after heat treatment

Drastic differences in surface texture were apparent after the heat treatment process. A mixture of two different types of α-alumina (round nodules and thin ridges) was apparent in the SEM images.

The aluminized felt was then cut to fit in the reactor and dried in an oven at 120°C for two hours to remove water vapor. The substrate was weighed using a Scientech SA 120 scale to establish an initial mass, then dip coated in the toluene/nanoparticle slurry. The nanoparticles adhered to the substrate and the toluene solution turned from black to clear after several minutes of slight agitation. The catalyst impregnated FeCrAlY was then dried at 110°C for two hours and weighed again to assess total mass loading.

5.3 Characterization

Several small (19 mm x 10 mm) sections of aluminized FeCrAlY were loaded with catalyst for initial testing and characterization. One section was loaded into the reactor and exposed to a moderate temperature (500°C) high velocity (>10 m/s) flow of nitrogen to test for catalyst adhesion and durability (typical velocities during experiments were ~ 5 m/s). The samples were then taken to the CAMCOR facility at the University of Oregon for SEM imaging. In the previous work done by Valmikanathan, particle sizes of 15nm were produced [36]. Similar particle sizes were seen in this research, but a large degree of agglomeration occurred as can be seen in Fig. 5.3 and Fig. 5.4. The nanoparticles can be seen as the clumped small round particles distributed throughout both figures.
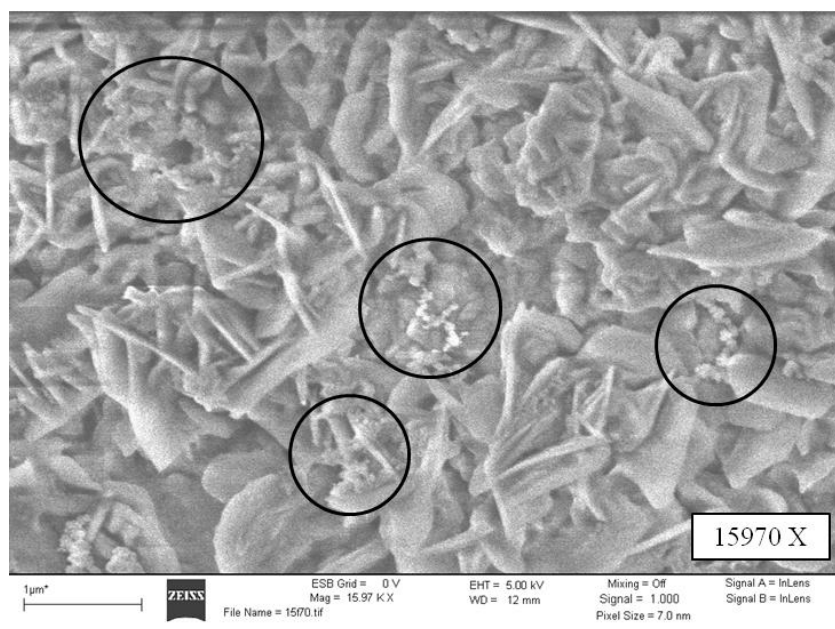
Fig. 5.3: SEM image of coupon 15 with no shear testing

No noticeable reduction in particle density was observed after the shear testing, suggesting that particles were adequately adhered to the substrate.
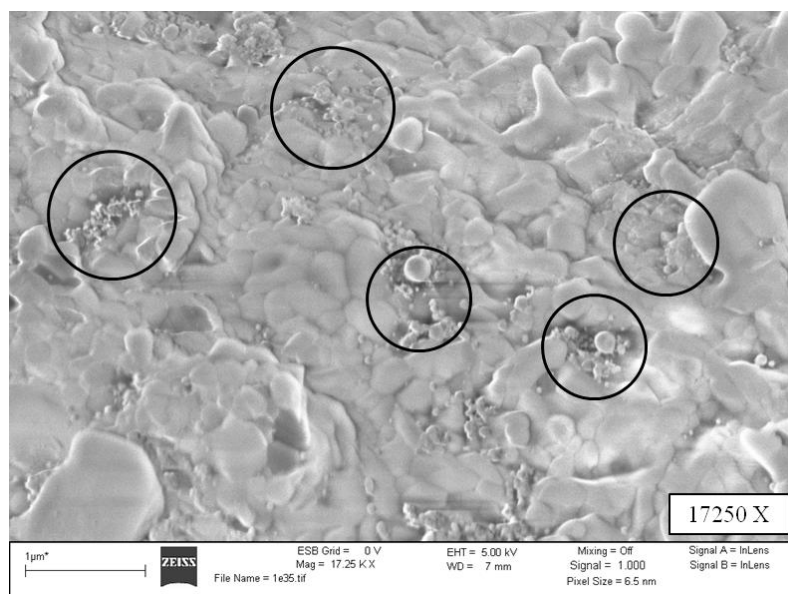
Fig. 5.4: SEM image of coupon 1 after shear testing

The SEM imaging demonstrated the durability of the catalyst and the suitability of the substrate material.

5.4 Reduction
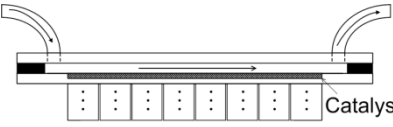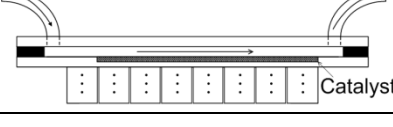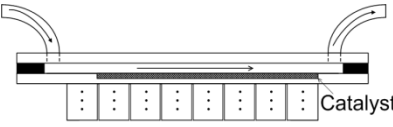
For the catalyst to fully facilitate the reaction, it must be exposed to a reducing agent. Reduction of noble metal catalysts is performed using a high temperature stream of H_2 either in pure form or carried by an inert gas. The process is generally carried out at temperatures of $350 - 800°C$ for a period of $1 - 3$ hours [35,17,23,26]. The reduction procedure used during these experiments uses the same prescribed temperature regime as the work performed by Hou and Hughes [17] but utilizes a H_2/inert mixture where as Hou and Hughes used pure H_2. A mixture of 4% (molar) H_2, 96% Ar was purchased from Airgas. An Ar mixture was used (as opposed to N_2) due to availability of the gas mixture at a highly reduced cost.

The catalyst bed was situated in the reactor, and the reactor was assembled and configured inside the test loop. A N_2 stream was fed through the test loop and the reactor was heated to a temperature of $500°C$ and held constant for one hour. The feed gas was then switched to the H_2/Ar mixture and maintained at $500°C$ for two hours. The temperature of the reactor was then increased to $600°C$ and held for an additional hour. The feed gas was then switched back to N_2 and either experiments were conducted immediately, or the torches were turned off and the system was allowed to cool to ambient while maintaining the flow of nitrogen.

5.5 Catalyst Configurations Used in Experiments

A total of five catalyst configurations were used during the experiments (Table 5.1). The channel heights of each catalyst configuration are listed in Table 5.1.

Table 5.1: Details of catalyst configurations

Catalyst Bed	Total Mass Loading (mg)	Est. Pd Loading (mg)	Bed Length (mm)	μ-chan ht. (μm)	Description	Schematic
Coupon 1	5.3	1.9	10	750	Small coupon for initial activity testing	
Bed A	68	24.3	152	710	Catalyst present in 8 heating zones	
Bed B	87.1	31.1	133	870	Catalyst present in 7 heating zones	
Bed C	150.9	54	133	700	Same as "B" but with higher Pd loading and preferential dip-coating	
Bed D	N/A	~40	133	1067	Catalyst wash coated directly on reactor surface	

The length of catalyst bed A is longer than others due to the catalyst originally being deposited in the first heating zone. The configuration was later changed whereby the catalyst was removed from the first heating zone to effectively lengthen the preheating zone. Total mass loading of the catalyst bed was not entirely due to the mass of the palladium. Catalyst bed C was loaded with a full batch of palladium nanoparticles, which corresponded to a total palladium mass of 60 mg, but the increase in mass was found to be 151 mg. Using bed C as a reference and assuming 10% palladium loss through the multiple container exchanges during the synthesis process, an estimated palladium mass loading was calculated to be 36% of the total mass loading. The total mass of all constituents (except toluene and H_2O) was 142 mg, less than the total mass loading of 151 mg as seen on catalyst bed C. Although the difference is less than 10%, that would

imply that none of the constituents remained in the aqueous phase. It is evident that an alternative method of catalyst loading characterization (such as H_2 chemisorption) needs to be used to more accurately assess the small mass loadings present in such systems.

It is important to note that a general dip-coating technique was used on catalyst bed B where a near-uniform dispersion of catalyst was expected; whereas catalyst bed C was dip coated using a selective technique to enhance the percentage of catalyst present at the surface of the catalyst bed. A small amount of toluene solution containing concentrated Pd nanoparticles was poured into an aluminum block with a machined slot designed to accommodate a single catalyst bed. The catalyst bed was placed in the aluminum block to absorb the small amount of liquid; this procedure was repeated several times with special attention being paid to which side of the catalyst was subject to the enhanced loading. When catalyst bed C was loaded into the reactor, the side with the higher Pd loading was placed upwards, exposed to the open channel of the reactor.

6. EXPERIMENTAL PROCEDURE

Running the experiment required accurately manipulating the inlet flow streams while maintaining prescribed temperature conditions throughout the channel. Procedural steps had to be followed to ensure catalyst integrity as well as to mitigate the possibility of unwanted ignition of the flammable gases. To minimize operator error during the experiments, operational flowcharts were generated.

6.1 Startup Procedure

Prior to the start of each experiment, the levels of propane, CH_4, and N_2 were checked and refilled if necessary. The desiccant cartridges were such that a color change from blue to pink occurs once the desiccant material can no longer absorb moisture. If the desiccant was pink, the cartridge was either replaced, or reactivated at 115°C for a minimum of two hours. A flowchart detailing the startup procedure is provided in Fig. 6.1. The gas valve was set to N_2 and the outlet valve was set to vent. Valves on all propane equipment (torches and pre-heater burner) were set to off. The solenoid valves on the propane and CH_4 delivery lines were turned on and enabled. The pressure transducer demodulator was then turned on. The mass flow controller was powered on and set to the desired flow rate, causing nitrogen to flow through the test loop. The evaporator was plugged in and enabled through the PID controller. The LabVIEW VI was started on the computer and checked to ensure all inputs were being received properly.

Occasionally the instruments would not be communicating properly with the computer. This was addressed by either restarting LabVIEW, or by restarting the computer. Once the LabVIEW program was operating properly, data recording was enabled. Set points for the first experiment were input into the LabVIEW VI which enabled plotting of actual versus desired operating conditions for surface temperature, CH_4 flow rate and H_2O flow rate.

Start Experiment

- Set gas valve to N_2
- Set outlet valve to vent
- Set torches and pre-heater to OFF
- Turn on gas solenoids

- Open main N_2 valve
- Turn on pressure transducer demodulator
- Turn on mass flow controller and set to desired flow rate
- Turn on evaporator

Diagnose and restart computer if necessary

Start LabVIEW VI

Is data being received properly?

no

yes

- Start data recording in LabVIEW
- Open main propane valve
- Turn on and ignite pre-heater
- Turn on and ignite all torches
- Open water valve to heat exchanger

- Adjust torch valves until reactor temperatures are near (+/- 50°C) desired setpoint
- Turn on H_2O pump

- Adjust H_2O flow rate with valve

Is H_2O at desired flow rate?

no

yes

- Open main CH_4 valve
- Switch gas valve to CH_4

Are reactor temperatures stable at desired levels?

no

Individually adjust torches to achieve desired temperatures

yes

Proceed to sampling procedure

Fig. 6.1: Experiment startup flowchart

The main propane valve was then opened slowly. Quickly opening the valve would cause an internal safety switch to be triggered whereby the propane flow rate would be greatly limited. The pre-heater burner was turned on and ignited with a laboratory gas lighter. The pre-heater torch was turned on and also ignited with the laboratory gas lighter. The neighboring torches were turned on in series and lit by the neighboring flame. The flow rate of each torch was adjusted so that the cone of the flame was just touching the surface of the reactor. The water valve to the heat exchanger was then turned on.

The reactor temperatures were monitored in LabVIEW. As the reactor temperatures approached the desired levels, the torch valves were adjusted individually to achieve the correct temperature at each heating zone to within 50°C. For experiments involving sampling a short time period after the reforming process had started, this tolerance was reduced to 10°C. At this point the H_2O pump was turned on and the water valve was adjusted to the correct flow rate based on the CH_4 flow rate and the steam-methane ratio desired. The H_2O flow rate was continuously monitored throughout the experiment and adjusted if necessary. A significant increase in pressure was observed in LabVIEW, verifying that steam was flowing through the reactor. At this point the main CH_4 valve was opened and the regulator was set to 170 kPa (25 psi). The gas valve was switched from N_2 to CH_4 and the experiment start time was recorded.

Minor adjustments were made to each torch to fine tune the temperature in each heating zone. This process was ongoing throughout the each experiment. The startup procedure generally required about 45 minutes. Reactor temperatures were regarded as stable once all measurements were within 10°C of the desired point for a period of three minutes. Once stability was achieved, sampling procedures commenced.

6.2 Sampling Procedure

Sampling of the outlet gases was conducted at different intervals depending on which tests were being performed, but the same general procedure was used as outlined in Fig. 6.2.

```
            ╭──────────────────╮
            │  Start Sampling   │
            │   Procedure       │
            ╰──────────────────╯
                     │
                     ▼
   ┌──────────────────────────────────────────────────┐
   │ •   Evacuate sample bag using a syringe            │
   │ •   Switch outlet valve to desiccant               │
   │ •   Ensure outlet gas flows through hypodermic needle │
   │ •   Wait two minutes to flush filters              │
   └──────────────────────────────────────────────────┘
                     │
                     ▼
   ┌──────────────────────────────────────────────────┐
   │ •   Insert outlet needle into septum of sample bag │
   │ •   Record time and bag number                     │
   │ •   Allow bag to fully inflate but not pressurize  │
   │ •   Remove outlet needle from sample bag           │
   └──────────────────────────────────────────────────┘
                     │
                     ▼
        ┌────────────────────────────────────┐
        │ •   Return outlet valve to vent      │
        └────────────────────────────────────┘
```

Fig. 6.2: Sampling procedure flowchart

Sample bags were used multiple times across experiments and had to be evacuated of previous sample contents prior to being used again. This was achieved by placing a smooth board on top of the sample bag and inserting a hypodermic needle into the septum of the sample bag. Once the majority of the contents had been evacuated, a 50 cc syringe was connected to the needle and the remaining gases were withdrawn. The needle and syringe were removed from the sample bag while vacuum pressure was held in the syringe.

Two minutes prior to the expected sample time the outlet valve was switched to direct the flow through the desiccant cartridges. The volume of each desiccant cartridge was on the order of 50 ml, and it was desired to completely flush the contents of previous experiments. The outlet terminated at a section of tubing that was fitted with a hypodermic needle, through which all outlet gases passed. At the desired time, the needle was inserted into the septum on the sample bag. The time and bag number were recorded in the log book for reference. The sample bag was allowed to fully inflate, at which point the needle was removed. The outlet valve was then switched back to vent to reduce the water vapor load through the desiccant.

6.3 Shutdown Procedure

After all samples had been collected, a set sequence of steps was performed to ensure that the catalyst was not damaged. The flowchart detailing the shutdown procedure is shown in Fig. 6.3. To begin the shutdown procedure, the gas flow was switched from CH_4 to N_2. The main tank valve on the CH_4 tank was turned off. The H_2O flow was stopped by turning off the pump. Data collection in LabVIEW was stopped, but the program was kept running in order to monitor temperatures. The main propane valve was turned off, as were both solenoid valves. The pre-heater burned was then turned off, followed by the evaporator. Time was allowed for the propane torches to burn off the residual gas present in the delivery lines, after which all propane torch valves were closed. The water flow to the heat exchanger was then stopped. Approximately two hours was required for the reactor to cool to near ambient temperature. Once the reactor temperature was below 30°C, the LabVIEW program was stopped. The mass flow controller was turned off, as was the pressure transducer demodulator. The N_2 tank valve was closed and the collected data were backed up onto a network drive.
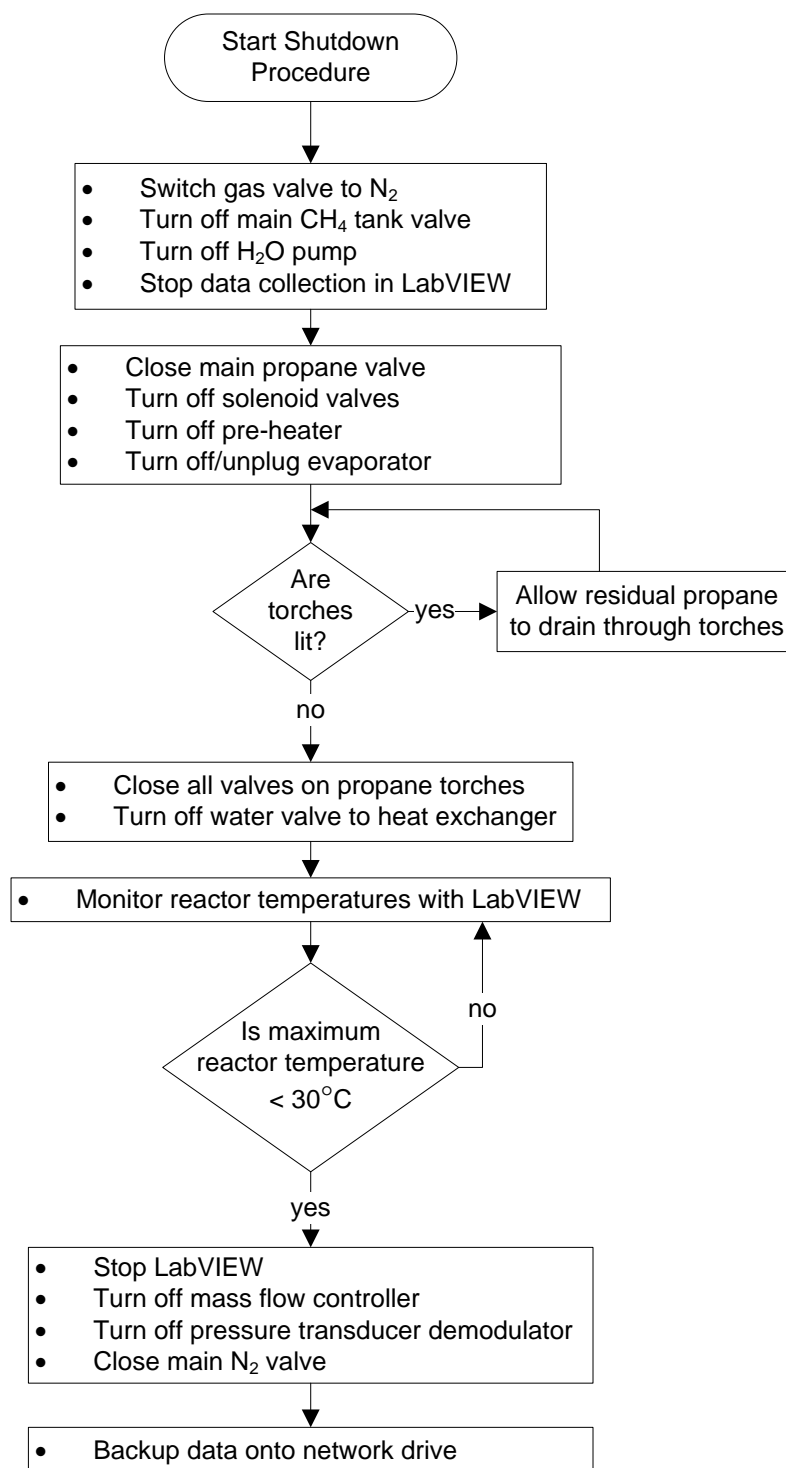
Fig. 6.3: Shutdown procedure flowchart

7. DATA ANALYSIS

In this chapter the calibration procedures are outlined and the stabilities of the salient measurements are analyzed. Additionally, equations used in the analysis are identified followed by an uncertainty analysis of the quantities of interest.

7.1 Calibration

Calibrations were conducted on all thermocouples, pressure sensor, Coriolis flow meter, and gas chromatograph. The factory calibration was used for the Sierra mass flow meter.

7.1.1 Thermocouple Calibration

 All thermocouples used in the experiment were of type K with special limits of error. The uncertainty associated with these thermocouples without calibration was the greater of 1.1°C or 0.4% of the reading. At the elevated temperatures that were anticipated in this experiment, that corresponded to an uncertainty of approximately 3.5°C.   R, S, and B type thermocouples all have much smaller uncertainties and would have been highly desirable for this experiment, unfortunately the precious materials (platinum and rhodium) used to construct these thermocouples kept them well out of the price range. Several companies offer high temperature thermocouple calibration at the cost of over $300 per thermocouple, for a potential total cost of $8,400. As this expense was outside the budget of the project, it was decided to use a calibrated resistance temperature detector (RTD) probe (OMEGA® model PR-11-2-100/8-9-E-TA4F) with a listed accuracy of 0.55°C for temperatures greater than 300°C. Initially all probes were simply inserted into the high temperature oven, but it was found that large thermal gradients were present within the oven, even after extended periods at a set temperature. A small (38 mm x 38 mm x 38 mm) copper block was drilled with 29 holes to accommodate all thermocouples and the RTD. The block was situated inside the oven and each thermocouple was fed through the top hole in the oven and inserted into the copper block using a small amount of high temperature copper based anti-seize lubricant (Fig. 7.1). The oven was heated to 300°C and left for two hours to stabilize and eliminate any

thermal gradients. Over 30 thermocouple measurements were collected at each calibration point for each thermocouple. The RTD temperature was also recorded at each calibration point. The system was allowed to stabilize for a minimum of 90 minutes between calibration points.

Fig. 7.1: Thermocouple calibration in high temperature oven

Calibration data were collected starting at 300°C at intervals of 70°C. It was thought that the maximum temperature of the RTD probe was 1100°C due to accuracies being tabulated for temperatures up to that range on the calibration sheet provided by OMEGA®. A large difference between the thermocouple measurements and the RTD was observed at temperatures above 650°C. At 790°C the RTD failed and the calibration procedure was halted. It was then ascertained that the maximum temperature listed for the RTD was only 600°C. The RTD probe was irreversibly damaged by the high

temperatures and had to be replaced. All calibration points over 600°C were discarded, yielding a maximum calibration temperature of 580°C. An example calibration curve for thermocouple number 3 is shown in Fig. 7.2. Calibration curve parameters for all thermocouples are tabulated in Appendix B.
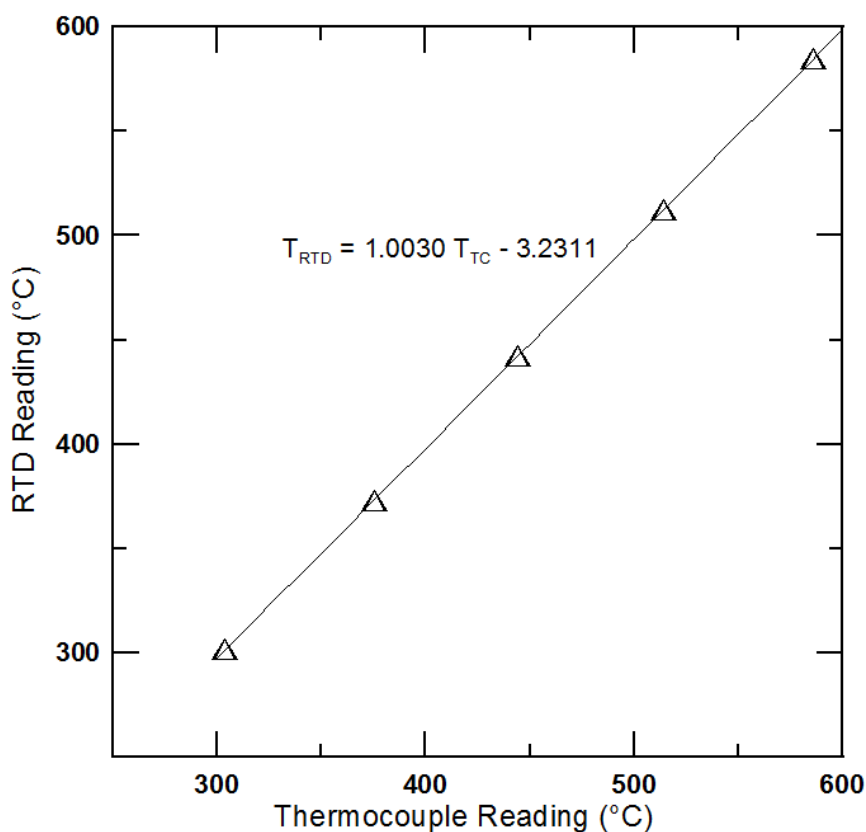
Fig. 7.2: Thermocouple calibration for thermocouple #3

The maximum curve fit uncertainty was 0.25°C with a maximum total calibration uncertainty of 0.62°C. The experiments were conducted with this less than ideal temperature calibration due to time constraints.

7.1.2 Pressure Calibration

It was important to measure the pressure near the reactor to determine the density of the flow as well as to monitor transients to ensure steady flow. The Validyne pressure transducer was calibrated against two pressure standards from OMEGA®. The low range

standard was a model PCL-MA with a range of 0 - 2500 Pa (0 – 10 in. H₂O). The high range standard was a model PCL-MB with a range of 0 – 689 kPa (0 - 100 psi). The listed accuracies for low and high range standards were 0.06% of full scale, and 0.05% of full scale respectively. This corresponded to an accuracy of 1.5 Pa for the low range standard and 344.5 Pa for the high range standard. The calibration configuration consisted of a 0.6 m (2 ft) long steel pipe with a cross-fitting situated in the middle. The calibration standard and the pressure transducer were attached via 6.4 mm (0.25 in) tubing to either side of the cross fitting. The entrance of the pipe was fed by compressed air which could be metered with a valve. The exit of the pipe also had an adjustable valve for controlling the backpressure. Both valves were adjusted to achieve a steady flow through the calibration chamber. Calibration was performed up to 51 kPa gauge pressure (Fig. 7.3).
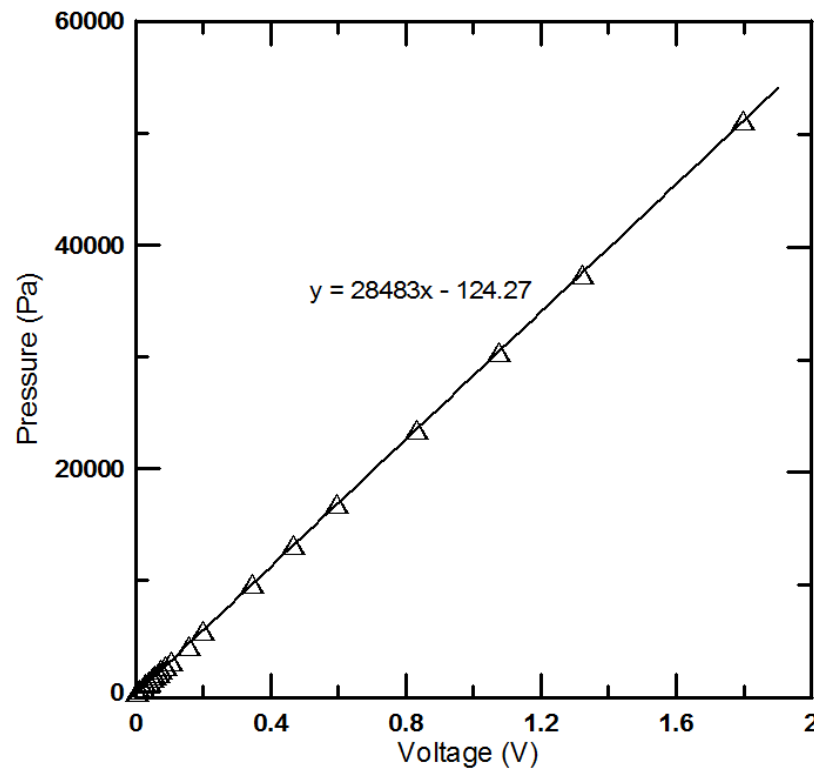
Fig. 7.3: Pressure transducer calibration

The calibration curve-fit uncertainty of the pressure transducer was 63 Pa. The calibration uncertainty combined with the accuracy of the large scale pressure standard resulted in a total calibration uncertainty of 350 Pa.

7.1.3 Water Flow Calibration

The peristaltic pump that was acquired for the experiment was equipped with an adjustment to provide variable flow rate, but initial testing demonstrated that reducing the speed on the pump caused the head to ratchet, producing highly variable flow. It was decided to run the pump at full speed and meter the flow rate using an alternative method. Several bypass/recirculation configurations were tested, with the most stable results coming from a configuration of a single line with a needle valve to control the flow. The pump produced a pressure of 689 kPa (100 psi), and all flow control was derived from a 16 turn needle valve. Water then flowed into the Coriolis meter and was subsequently piped to the evaporator. For the calibration, the hose was disconnected from the evaporator and situated over a 50 ml beaker for water collection. The dry weight of the beaker was measured and recorded. The water flow was started and the valve was adjusted to the proper flow rate and allowed to stabilize. Coriolis flow measurements were recorded at one hertz for 10 minute time periods at each calibration flow rate. The mass of the water collected over the 10 minute time period was measured and divided by 10 to produce an average flow rate measurement in grams per minute. This process was repeated for six calibration points from 0.33 – 4.5 g/min. Scale measurements were compared to average flow rates measured by the Coriolis meter and a calibration curve was generated (Fig. 7.4).
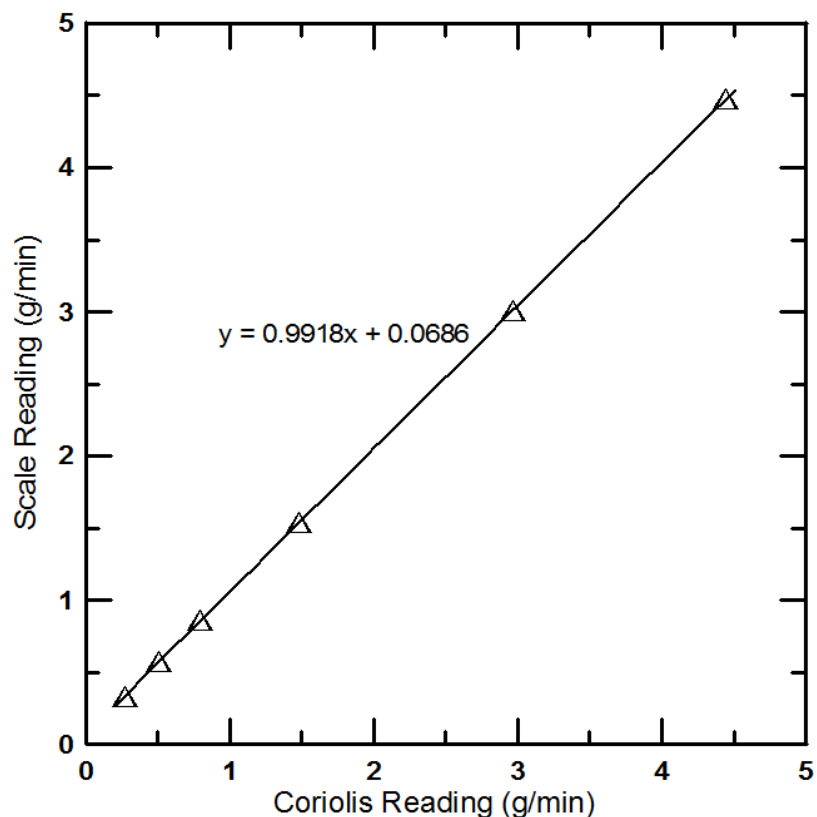
Fig. 7.4: Coriolis flow meter calibration

The calibration curve-fit uncertainty of the Coriolis flow meter was calculated to be 0.0029 g/min over this range. The accuracy of the scale used in the measurements was listed as 0.0002 g, and did not affect the calibration uncertainty.

7.1.4 Gas Chromatograph Calibration

A Hewlett Packard® model 5890 gas chromatograph (GC) equipped with a thermal conductivity detector (TCD) was used for the gas analysis. For calibration, a gas mixture containing 1% (+/- 0.02%) of H_2, CO, CH_4, CO_2 and O_2 (balance N_2) was obtained from Scott Specialty Gases. The elution order of the detector was obtained by analyzing individual pure gases and observing the elution time. The calibration gas was transferred into a SKC sample bag and subsequently loaded into the GC using a 100 µl Gastight® syringe. The elution order and relative return strength from the calibration gas are shown in Fig. 7.5.
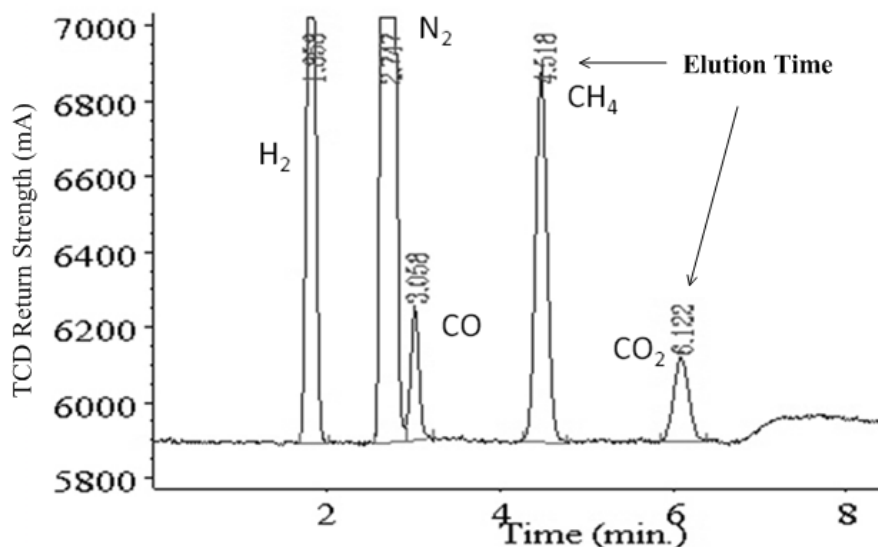
Fig. 7.5: Gas chromatograph return of calibration gas

ChemStation software was used for the identification and integration of the returns. Return strengths of the calibration gas were measured four times over a two month period. These four calibrations were used to generate gas concentrations for three samples (12 – 40% H_2), whereby the standard deviation of the concentrations was used to formulate accuracy measurements for each gas. The sensitivity and accuracy of the GC to N_2 was not quantified as it was not integral to the analysis. The sensitivities used for the gas analysis (normalized by H_2) along with the accuracy for each species are shown in Table 7.1. To avoid saturation of the detector, a 40 µl injection volume was used for the calibration and all samples.

Table 7.1: Gas chromatograph calibration sensitivities and accuracies

Gas	Elution Time (min)	Sensitivity	Accuracy
H_2	1.9	1.0000	4.99%
CO	3.1	0.1194	6.57%
CH_4	4.5	0.4611	1.95%
CO_2	6.1	0.1437	5.30%

7.2 Stability

All experiments targeted a steady-state operation. The degree to which this was attainable was variable between the multiple measured parameters, but stayed nearly constant over the different experiments. The temperature stability tests were performed over two 250 minute periods on 5/3/10 and 5/12/10. The stability assessments of pressure, H_2O flow rate, and CH_4 flow rate were conducted over a five minute period during testing on 4/5/2010. The repeatability of the gas analysis measurements was conducted by analyzing a triplicate sample.

7.2.1 Temperature Stability

The temperature of the reactor was controlled by the manual adjustment of valves controlling the nine propane blow torches. Thermocouple temperatures were monitored and reactor surface temperatures were calculated and displayed in LabVIEW (see Eq. (7.11)). The heat flux into each heating block was near constant at a given propane flow rate, but the temperature would oscillate in time due to periodic operator manipulation of the torch valves depending on if the amount of heat input was above or below what was necessary to maintain the desired surface temperature. Time-series temperature profile data for two 250 minute catalyst stability tests are shown in Fig. 7.6. Surface temperature data presented in Fig. 7.6 was calculated at the reactor surface of the pre-heater and is referred to as the inlet temperature.
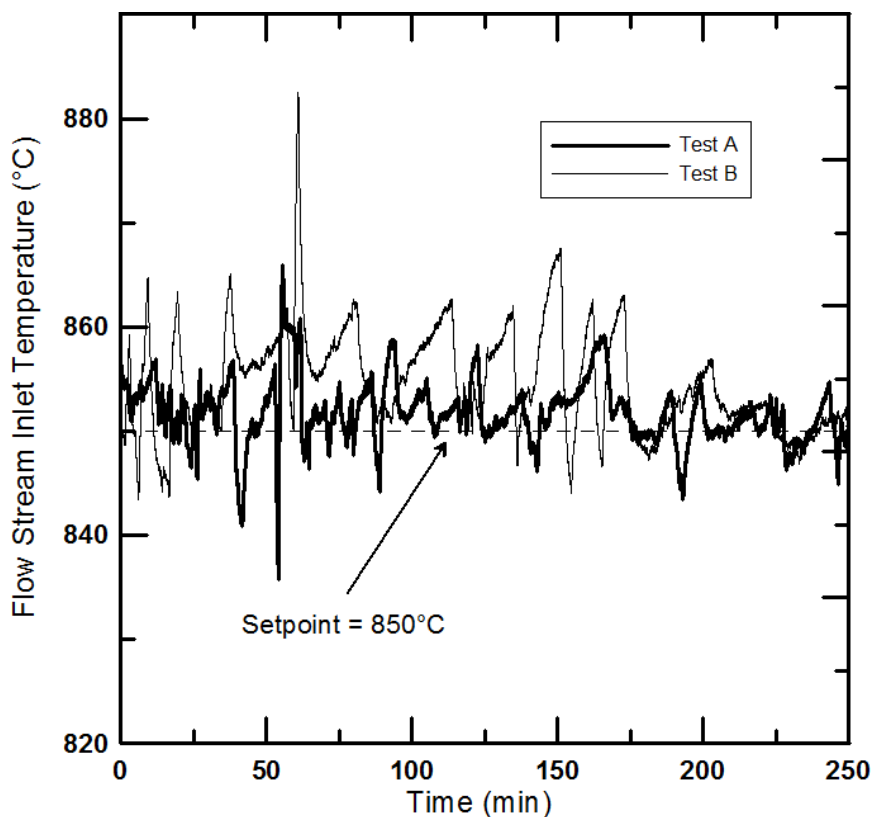
Fig. 7.6: Flow stream inlet temperature time series

Due to the manual nature of the adjustment and the lagging response from flame adjustment to temperature change, a stable temperature was difficult to achieve and required a large amount of operator adjustment. The standard deviation from the setpoint for test A was 0.42% (3.6°C) while the standard deviation for test B was higher at 0.80% (6.8°C).

7.2.2 Pressure Stability

Pressure just upstream of the reactor was monitored throughout the experiments using a Validyne DP15-40 differential pressure transducer equipped with a $0 - 276$ kPa (0-40 psi) diaphragm connected to the computer through a Validyne CD15 carrier demodulator. It was necessary to monitor the pressure near the reactor for multiple reasons. Firstly, absolute pressures were necessary to determine the density values for the two reactants which were instrumental in residence time calculations. Secondly, pressure readings were used as a method of monitoring flow stability through the test loop. The flow rates

of the incoming streams were being monitored, but the inherent instabilities associated with the phase change process led to concerns about stable flow rates through the reactor. Thirdly, carbon deposits within the reactor (coking) can occur during steam-methane reforming in situations where insufficient steam is present to react with the methane. The resultant carbon can collect in the reactor and lead to a decreased cross-sectional channel area, causing an increase in pressure drop. The stability of the steam-methane reacting flow over a five minute period is shown in Fig. 7.7. The standard deviation of the pressure over this five minute period was measured to be 138 Pa, or 1.7% of the gauge pressure.
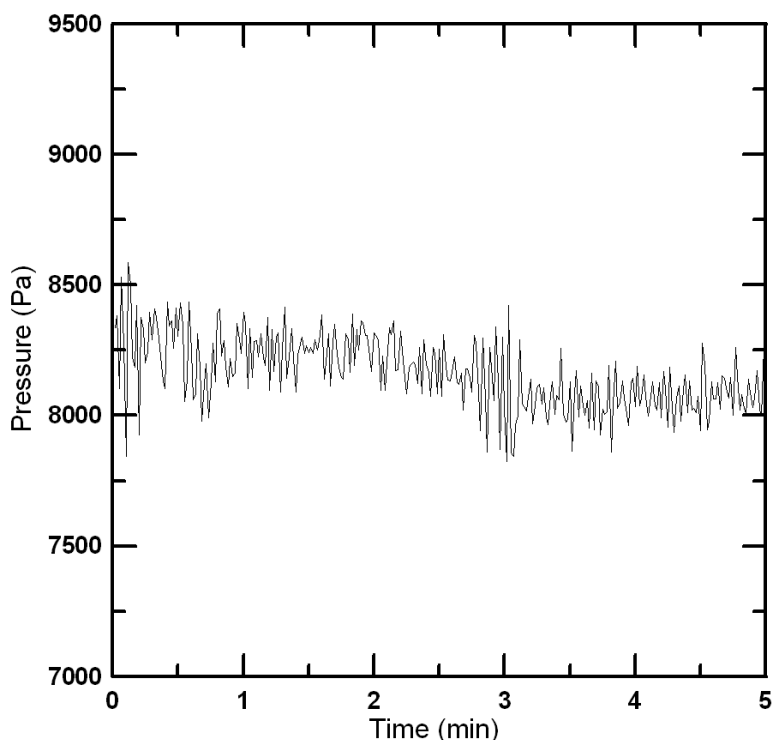
Fig. 7.7: Stability of reactor pressure

7.2.3 Water Flow Stability

The H_2O flow rate was controlled by a peristaltic pump capable of producing 689 kPa (100 psi) of upstream pressure and controlled by a 16 turn needle valve. Initial configurations did not isolate the pump from the pressure fluctuations accompanying phase-change in the evaporator resulting in backflow. Creating a large pressure drop

through a needle valve served to greatly stabilize the flow. A time series of the resultant flow is shown in Fig. 7.8. The standard deviation of the H_2O flow rate was measured to be 0.050 g/min, or 7.6% of the setpoint value. During the experiments, over 90% of the samples were at H_2O flow rates between 0.45 – 0.9 g/min with a maximum of 4.9 g/min. The magnitude of the variation was relatively stable at increased flow rates with a standard deviation of 0.056 g/min or 4.2% being produced at an average flow rate of 1.33 g/min.
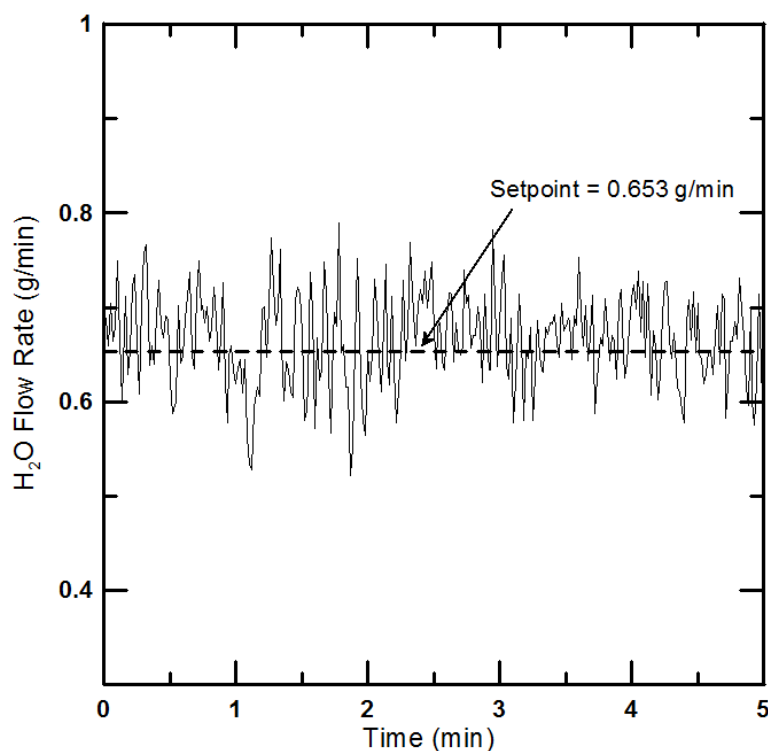
Fig. 7.8: Stability of the water flow rate

7.2.4 Gas Flow Stability

The methane flow rate was controlled by a Sierra Smart-Trak C100L mass flow controller. An internal proportional valve continuously adjusted the internal orifice size to maintain the flow rate at the setpoint. The upstream regulator pressure was set to 172 kPa (25 psi). The resultant gas stream was held within 0.9% of the desired value as seen in Fig. 7.9.
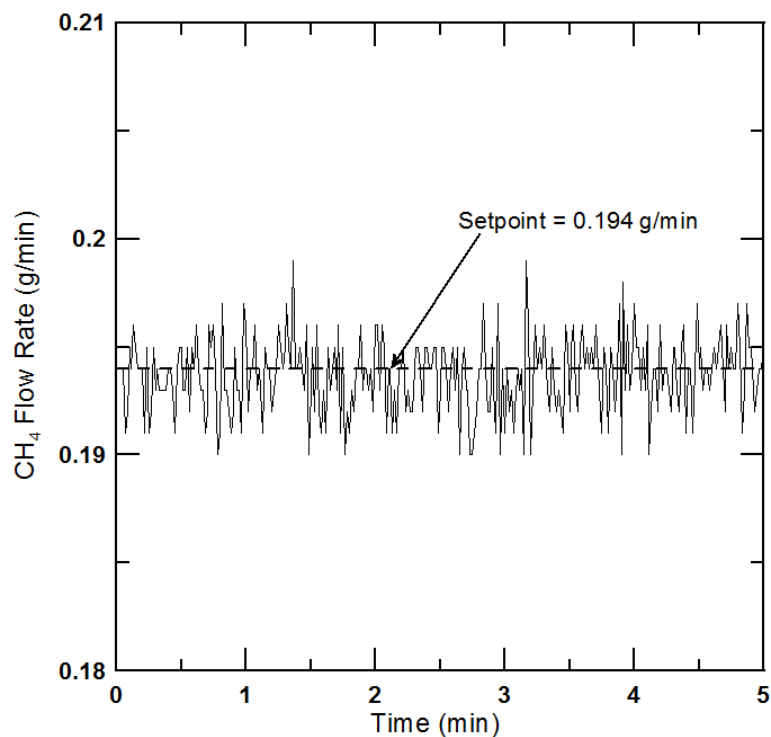
Fig. 7.9: Stability of the methane flow rate

7.2.5 Gas Chromatograph Repeatability

One sample from the steam-methane reforming experiment was analyzed three times in succession by the gas chromatograph. Molar percentages calculated using the sensitivities listed in Table 7.1 are listed along with the uncertainty for each species of interest in Table 7.2.

Table 7.2: Repeatability uncertainty of gas chromatograph

Sample	H_2	CO	CH_4	CO_2
1	15.2601%	2.5703%	80.5236%	1.6460%
2	15.2918%	2.5874%	80.5084%	1.6124%
3	15.3986%	2.5658%	80.3674%	1.6682%
Uncert.	0.47%	0.44%	0.11%	1.71%

The stability uncertainty for each gas species was calculated as follows

$$U_i(\%) = \frac{\sqrt{\frac{\sum(X_i - \bar{X}_i)^2}{n-1}}}{\bar{X}_i} \times 100 \tag{7.1}$$

where $U_i(\%)$ = percent uncertainty, X_i = measured molar concentration, $\bar{X}_i$ = average molar concentration, and n = number of samples.

7.3 Equations Used for Analysis

In this section the relevant equations for analysis are presented. In order for the results from this experiment to be applicable to the modeling efforts, it was necessary to ensure that the flow through the channel was within the laminar flow regime. The Reynolds number was calculated as

$$\text{Re} = \frac{\rho_{mix}\, U(2h)}{\mu_{mix}} \tag{7.2}$$

where ρ_{mix} is the mixture density, U is the average velocity, h is the channel height and μ_{mix} is the average kinematic viscosity. Molar flow rates of the reactants were determined using

$$\dot{\mathcal{M}}_i = \frac{\dot{m}_i}{\mathcal{M}_i} \tag{7.3}$$

where $\dot{\mathcal{M}}_i$ is the molar flow rate, $\dot{m}_i$ is the mass flow rate and $\mathcal{M}_i$ is the molecular weight of the component. The steam-methane ratio was calculated using the molar flow rates as

$$R_{SM} = \frac{\dot{\mathcal{M}}_{H_2O}}{\dot{\mathcal{M}}_{CH_4}} \tag{7.4}$$

The density of each input gas stream was determined using the ideal gas law

$$\rho_i = \frac{\mathcal{M}_i P}{(T + 273.15)R} \tag{7.5}$$

where P is the gas pressure, T is temperature and R is the universal gas constant. The mixture-averaged density of the reactant stream was calculated from the molar ratios of the constituents as

$$\rho_{mix} = \frac{R_{SM} * \rho_{H_2O} + \rho_{CH_4}}{R_{SM} + 1} \qquad (7.6)$$

The mixture-averaged viscosity was calculated in a similar manner as

$$\mu_{mix} = \frac{R_{SM} * \mu_{H_2O} + \mu_{CH_4}}{R_{SM} + 1} \qquad (7.7)$$

The volumetric flow rate at the entrance of the channel was calculated as

$$\dot{V} = \sum \frac{\dot{m}_i}{\rho_i} \qquad (7.8)$$

The flow velocity at the entrance of the channel was calculated using the volume flow rate and the channel dimensions as

$$U = \frac{\dot{V}}{w * h} \qquad (7.9)$$

where w is the channel width. Residence time in the channel was calculated using the open channel dimensions and volume flow rate as

$$t_{res} = \frac{l}{U} \qquad (7.10)$$

where l is the length of the channel with catalyst.

The surface temperature of the channel was found by extrapolating the temperature gradient observed in the heating blocks. The temperature extrapolation was only performed up to the interface of the stainless steel and the catalyst bed. Contact resistance between the catalyst bed and the stainless steel, along with conduction through the catalyst bed were unaccounted for. Consequently the actual surface temperature of the catalyst is underestimated. The magnitude of this discrepancy is not quantified in this work. A single heating section with measurement locations is shown in Fig. 7.10.
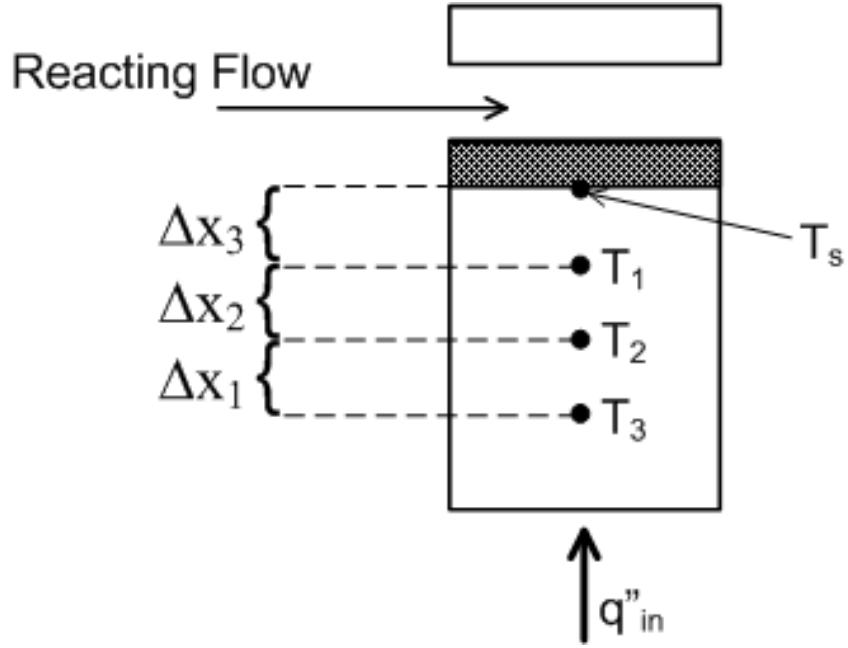
Fig. 7.10: Single conduction block configuration

The surface temperature of the stainless steel was calculated as

$$T_s = T_1 + \frac{T_1 - T_2}{\Delta x_2} * \Delta x_3 \qquad (7.11)$$

Heat flux through the stainless steel heating block was calculated between the thermocouples using three forms of the one dimensional form of Fourier's law.

$$q''_{12} = -k \frac{T_1 - T_2}{\Delta x_2} \qquad (7.12)$$

$$q''_{23} = -k \frac{T_2 - T_3}{\Delta x_1} \qquad (7.13)$$

$$q''_{13} = -k \frac{T_1 - T_3}{\Delta x_1 + \Delta x_2} \qquad (7.14)$$

The thermal conductivity of 304 stainless steel is variable with temperature. A second order polynomial fit was applied to four data points from Incorpera & Dewitt [51] that bracketed the experimental temperatures (527 – 1227°C) as follows.

$$k_{ss}(T) = 14.61 + 1.6 \cdot 10^{-2} T - 1.78 \cdot 10^{-6} T^2 \qquad (7.15)$$

7.4 Uncertainties

Uncertainties of all directly measured quantities are tabulated in Table 7.3. The thermocouple calibration uncertainty was doubled in an attempt to account for the limited calibration range. Total uncertainties were calculated using the root sum squared (RSS) of the calibration and stability uncertainties as follows

$$U_{Tot} = \sqrt{U_{Cal}^2 + U_{Stab}^2} \qquad (7.16)$$

where U_{Tot} = total uncertainty, U_{Cal} = calibration uncertainty, U_{Stab} = stability uncertainty.

Table 7.3: Uncertainties of directly measured parameters

Parameter	Calibration Uncertainty	Stability Uncertainty	Total Uncertainty
Temperature	0.20%	0.64%	0.67%
Pressure	350 Pa	138 Pa	376 Pa
H_2O Flow Rate	0.0029 g/min	0.050 g/min	0.050 g/min
CH_4 Flow Rate	0.021 g/min + 0.7%	0.9%	0.021 g/min + 1.1%
H_2%	4.99%	0.47%	5.01%
CO%	6.57%	0.44%	6.58%
CH_4%	1.95%	0.11%	1.95%
CO_2%	5.30%	1.71%	5.57%
Thermocouple separation			0.01 mm
All caliper measured distances (l, w, h)			0.05 mm

Sequential perturbation of dependant parameters by their corresponding uncertainties was used to generate uncertainties for the most important parameters of this study [55]. The results are tabulated in Table 7.4.

Table 7.4: Uncertainties of salient calculated parameters

Parameter	Uncertainty
Surface Temperature (T_S)	2.13%
Microchannel Height (h_g)	0.11 mm
Residence Time (t_{res})	17.3%
Steam-Methane Ratio (R_{SM})	14.9%

Details of the uncertainty analysis are available in Appendix C. The perturbations were conducted for a sample with a methane flow rate of 0.194 g/min, steam-methane ratio of 3, and reactor temperature near 850°C. The majority of the uncertainty of the surface temperature is associated with the lack of stability, not calibration. The large microchannel height uncertainty is due to it being a function of five measurements conducted with hand calipers with an uncertainty of 0.05 mm. If the caliper uncertainty could be reduced to 0.025 mm, the channel height uncertainty would be reduced to 0.056 mm. The residence time uncertainty is almost entirely attributed to the uncertainty of the channel height.   Uncertainties for the steam-methane ratio decrease at higher flow rates due to the absolute accuracy of the mass flow controller.

8. RESULTS AND DISCUSSION

This section presents and discusses data that were collected during the experiments. A total of 13 sets of experiments were performed on four different catalyst beds. Variation of temperature, pressure, residence time, steam-methane ratio, heat flux profiles, and temperature profiles were all tested.

8.1 Testing Matrix

The matrix of the experiments performed is listed in Table 8.1. Results for all experiments in this section are referenced to the experiment number in this table. Results from experiments 2, 7, 12 and 13 did not provide much insight into the system operation and are therefore located in Appendix D. Time averaged sample data for each experiment are available in Appendix E.

Table 8.1: Testing matrix of steam-methane reforming experiments

Exp. #	Cat. Bed	Date	Varied Parameter	Res. Time (ms)	$\dot{m}_{CH_4}$ (g/min)	Ave Temp °C	R_{SM}	Press. (kPa - abs)
1	A	2/9/10	Res. Time	8.4 - 22.1	0.25 - 1.0	865 - 879	4	134 - 201
2	A	2/15/10	Press.	22.9 - 37.0	0.25	762 - 776	4	127 - 202
3	B	4/5/10	Res. Time	10.1 - 42.5	0.15 - 0.77	777 - 797	3	107 - 134
4	B	4/7/10	Temp.	32.2 - 34.4	0.178 - 0.225	678 - 902	3	109 - 111
5	B	4/7/10	R_{SM}	24.7 - 27.2	0.15 - 0.3	817 - 825	2.54 - 5.8	112 - 120
6	C	4/20/10	Cat. Stability	23.8 - 26.6	0.192 - 0.195	850 - 893	2.74 - 2.99	103 - 104
7	C	4/28/10	q″ profile	25.7 – 26.3	0.194	808 - 811	2.94 – 2.95	104 - 106
8	C	5/3/10	Cat. Stability	24.1 - 26.0	0.194	854 - 874	2.86 - 3.05	105 - 108
9	C	5/3/10	Temp	24.8 - 27.3	0.183 - 0.233	625 - 904	2.87 - 3.13	105 - 108
10	C	5/4/10	Res. Time	5.3 - 34.1	0.15 - 1.40	777 - 783	2.91 - 3.15	106 - 162
11	C	5/4/10	Temp. Profile	25.7 - 29.6	0.194	748 - 759	3.01 - 3.07	108
12	D	5/12/10	Cat. Stability	25.1 - 26.8	0.284 - 0.285	849 - 853	2.76 - 3.03	104
13	D	5/12/10	Temp.	25.7 - 28.0	0.255 - 0.336	626 - 924	2.82 - 3.13	103 - 107

The details of the different catalyst beds were presented in Ch. 5 (Table 5.1).

8.2 Initial Testing

To test the viability of the catalyst, a preliminary experiment was performed whereby a small aluminized FeCrAlY coupon was treated with a dilute solution of catalyst and placed in the reactor. The catalyst loading of the coupon was approximately 1.9 mg of Pd. At a reactor temperature of 850°C, steam-methane ratio of 4, and a residence time through the catalyzed portion of less than 1 ms, approximately 1% hydrogen was detected in the dry outlet stream. This verified the activity of the catalyst.

Catalyst bed A, with a Pd mass loading of 24.3 mg, was used for experiment 1 in Table 8.1. The methane mass flow rate was varied from 0.25 to 1.0 g/min which corresponded to residence times of 8 – 22 ms (Fig. 8.1). The average surface temperature ranged from 865 – 880°C and the absolute pressure ranged from 134 – 201 kPa for this experiment. Four gas samples were collected and analyzed.
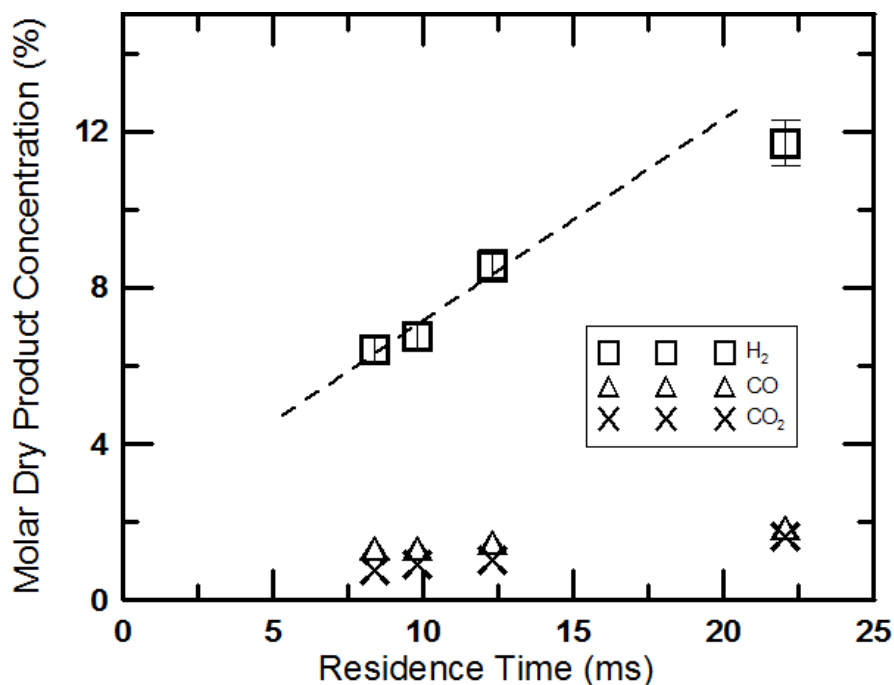

Fig. 8.1: Dry product concentration for residence time variation (Exp. 1)

The outlet gas was only analyzed for the four principle components: hydrogen, methane, carbon monoxide, and carbon dioxide. Methane concentrations are omitted from the molar concentration plots for clarity. Error bars are limited to the H_2 molar

concentrations due to that being the main metric of performance. At the highest residence time (lowest H_2O and CH_4 flow rates) a H_2 outlet concentration of nearly 12% was observed. Assuming a constant reaction rate for high CH_4 concentrations (low H_2 concentrations), a linear trend of H_2 concentration to residence time would be expected. Figure 8.1 shows an increasing trend of H_2 production with residence time with slight non-linear behavior. Deviations from this linear trend could be attributed to fluctuations of reactor temperatures and pressures.

8.3 Stability of Catalyst

The stability of catalyst bed C was tested over two 250 minute periods (experiments 6 and 8); first on 4/20/10 and then again on 5/3/10. The parameters for these experiments are listed in Table 8.2.

Table 8.2: Experimental parameters of catalyst bed C stability tests

Experiment #	6	8
Date of Experiment	4/20/2010	5/3/2010
Upstream Pressure (kPa)	103.2 – 104.3	104.7 – 107.6
CH_4 Flow Rate (g/min)	0.192 – 0.196	0.193 – 0.194
Steam - Methane Ratio	2.58 – 2.99	2.86 – 3.05
Average Reactor Temp (°C)	850.2 – 892.8	853.5 – 873.7
Residence Time (ms)	23.8 – 25.6	24.1 – 26.0
CO Selectivity (%)	58.1 – 66.7	50.2 – 54.1

The molar concentrations of the output gases from the experiments on 4/20/05 are shown in Fig. 8.2. The gas concentration output from experiment 6 followed an unexpected trend. The hydrogen output was initially very low, at 10% after 2 minutes, and then increased rapidly to 32% after 30 minutes. A subsequent decrease in the reaction was observed, followed by another increase to a peak output of 39% hydrogen at 140 minutes. The initial increase in hydrogen production could have been caused by inadequate catalyst activation which subsequently occurred during the reforming process. The

reduction in activity between 30 – 100 minutes cannot be attributed to any measured changes in experimental parameters.
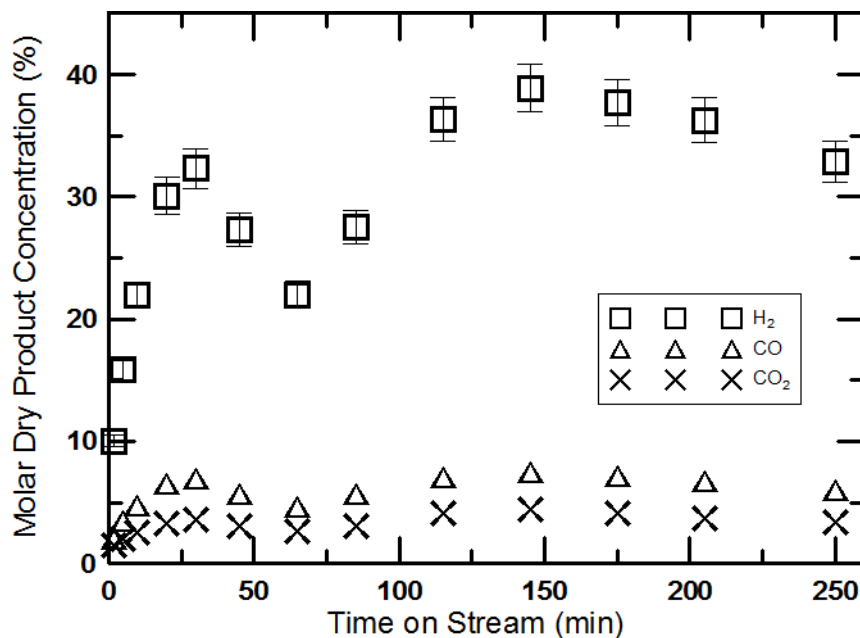

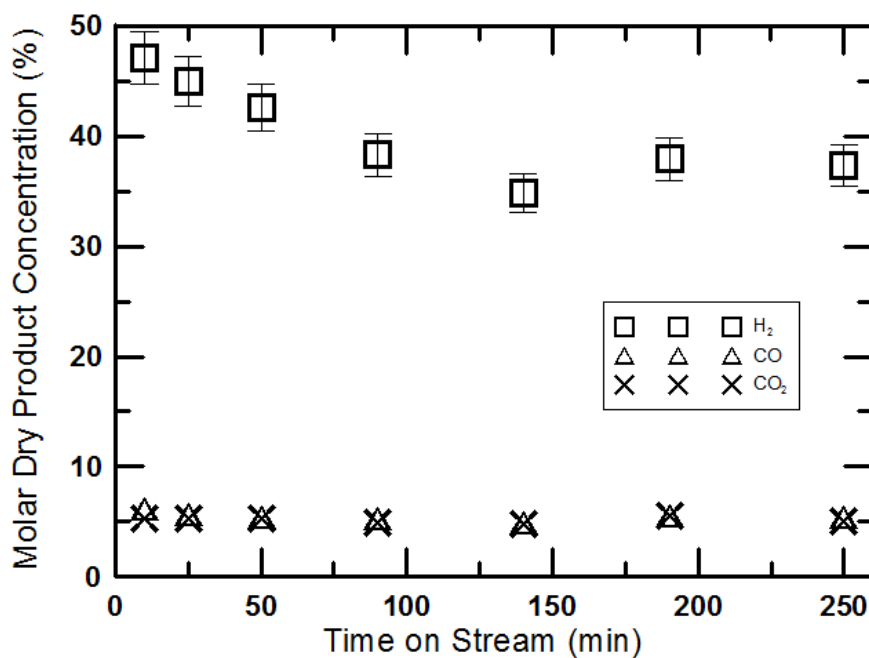Fig. 8.2: Time series output of catalyst bed C during 250 minute test (Exp. 6)

Fig. 8.3: Time series output of catalyst bed C during 250 minute test (Exp. 8)

Either there was some mechanism that caused a temporary decrease in catalyst activity, or some unmeasured experimental deviation from the set points of the experiment occured. As it remains, the temporary activity decrease in experiment 6 is unexplained. The same experiment was repeated on 5/3/10 (experiment 8) with gas outputs shown in Fig. 8.3. Total time-on-stream for the catalyst bed at the start of the experiment was 8 hours. The subsequent testing on catalyst bed C followed a trend of initial peak activity followed by a slow decrease, and final stabilization. A marked decrease in CO selectivity (ratio of CO to the sum of CO and CO_2 on a molar basis) was seen in catalyst bed C between experiments 6 and 8, suggesting an increase in the amount of water gas shift reaction taking place. Since the catalyst bed had previously been exposed to 8 hours of testing, it was postulated that the output of the 250 minute experiment would have been stable, however the output was variable. It is interesting to note that the H_2 production at the start of experiment 8 was higher than the H_2 production at the end of experiment 6, suggesting an increase in activity due to reforming during experiment 7.

8.4 Variation of Residence Time

Catalyst beds B and C were tested for output response for different residence times (experiments 3 and 10). The conditions for both experiments are listed in Table 8.3.

Table 8.3: Experimental conditions for residence time experiments

Experiment #	2	10
Date of Experiment	4/5/2010	5/4/2010
Catalyst Bed	B	C
Catalyst Loading (mg)	31.1	54
Channel Height (mm)	0.84	0.70
Upstream Pressure Range (kPa)	107 - 134	106 - 162
CH_4 Flow Rate (g/min)	0.150 - 0.771	0.150 - 1.40
Steam - Methane Ratio	2.88 - 3.04	2.91 - 3.15
Average Reactor Temp (°C)	777 - 797	777 - 788
Residence Time (ms)	10.1 – 42.5	5.3 – 34.1
CO selectivity (%)	61.0 – 64.5	32.8 – 40.7

The residence time was manipulated by changing the flow rate of both the steam and methane such that the steam-methane molar ratio was maintained constant. No backpressure was applied to the system, consequently the inlet pressure increased for the higher flow rates. An increase of 27 kPa was seen in experiment 3, whereas an increase of 56 kPa was seen in experiment 10. The difference in pressure changes between experiments is due to a lower residence time being tested during experiment 10. The change in pressure was accounted for in the density calculations. The dry output gas concentrations for experiment 3 are shown in Fig. 8.4. A total of seven gas samples were collected during experiment 3. Three samples of output gas were collected at a residence time of 32.5 ms over a 5 minute period. The sample standard deviation of the output gas molar concentrations amongst the triplicate samples was 0.6% for H_2, 0.5% for CO, 0.1% for CH_4 and 0.2% for CO_2. One of the samples was analyzed three times to assess the uncertainty of the gas analysis. All constituent gases in this analysis had a sample standard deviation of less than 0.8%, except for carbon dioxide which had a sample standard deviation of 2.6%.
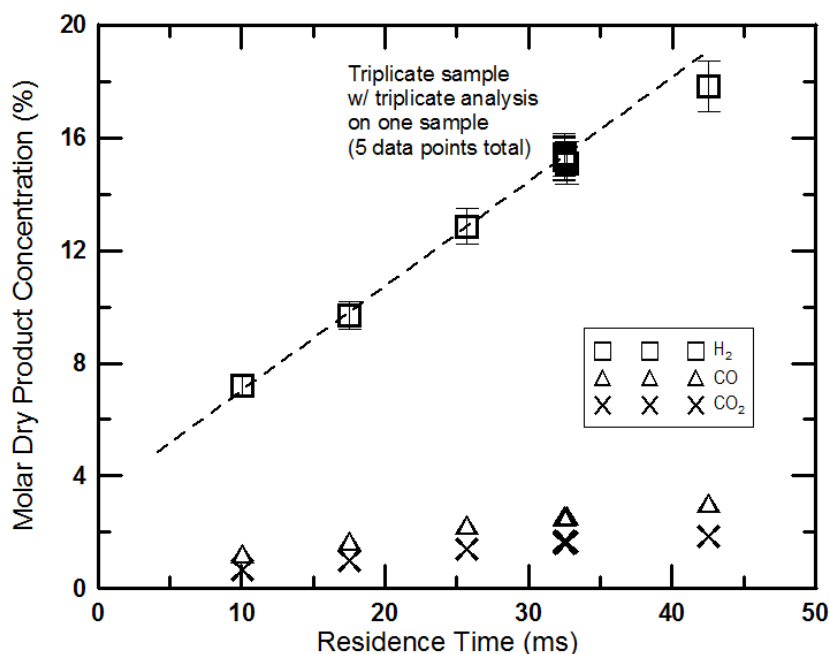
Fig. 8.4: Effects of residence time variation on catalyst bed B (Exp. 3)

Although the trend is highly linear, the intercept of the trend does not go to the origin as would be expected. Additional experiments at lower residence times would be useful in explaining this inconsistency.

During experiment 3, all heating torches were set to impinge on the heating surface at approximately the same intensity and a steady state surface temperature profile was allowed to develop. The decreasing trend in temperature along the channel is due to higher conduction and radiation losses near the exit of the channel. This temperature profile was then used as a target temperature profile for experiment 10. The temperature profiles for the two experiments coincided well with an average temperature difference of only 2°C (Fig. 8.5). The experiment was repeated on catalyst bed C on 5/4/2010 (Exp. 10 in Table 8.1). The gas analysis results for this experiment are shown in Fig. 8.6.

Fig. 8.5: Longitudinal temperature profiles (Exp. 3 and 10)

Fig. 8.6: Effects of residence time variation with catalyst bed C (Exp. 10)

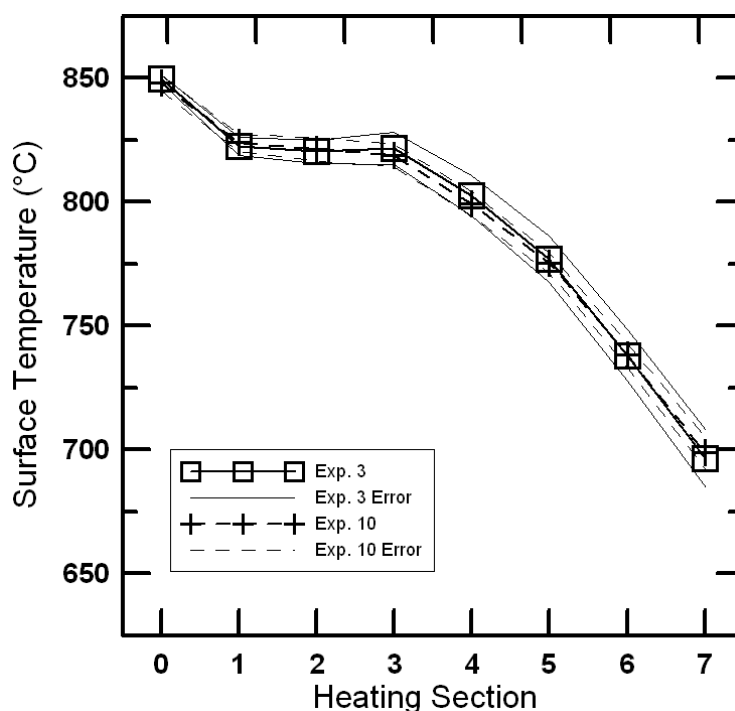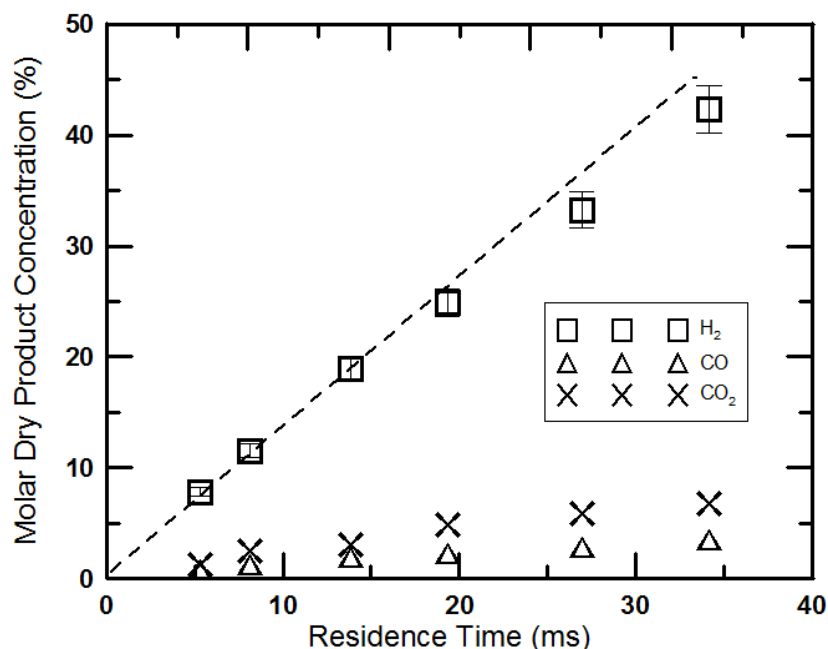Under matching conditions, the conversion rate of catalyst bed C was higher than catalyst bed B by a factor of 2.7 (1.34 $\%H_2/ms$ versus 0.50 $\%H_2/ms$); whereas the ratio of palladium mass loading of catalyst bed C to bed B was only 1.74 (54 mg versus 31.1 mg). The SEM images seen in Ch. 5 indicated that the surface was far from saturated with Pd nanoparticles, suggesting that an increased catalyst loading would lead to increased conversion of CH_4. This was verified by the increased activity seen with the higher preferential loading of catalyst bed C. It would be expected that the hydrogen output would vary linearly with increased catalyst loading (assuming that reaction sites are the limiting factor), but the increase in conversion from bed B to bed C cannot be explained by increased mass loading alone. The difference is most likely due to the variation in deposition procedure between bed B and bed C as discussed at the end of Ch. 5.

In both experiments, there was a slight decrease in the linear trend of hydrogen production as the residence time was increased. This can be attributed to the partial pressure of methane being reduced from the conversion process, thereby providing diminishing returns for additional residence time. This effect was seen in H_2 concentrations above 20% in both experiments.

There is a large discrepancy between the CO selectivity measurements of the two different catalyst beds. The residence time experiments on catalyst bed B were performed one day after the reduction process, and the CO selectivity matches closely what was observed immediately after reduction of catalyst bed C (see Table 8.2 and Fig. 8.1). The residence time experiment was performed on catalyst bed C after approximately 10 hours of on-stream testing. There is a strong trend of reduction in CO selectivity with increased time-on-stream for this experimental setup. A decrease in CO selectivity with time-on-stream was also observed by Tonkovich et al. [24] and Johnson et al. [29] over Rh catalysts; 3% reduction after 200 hr and 5% reduction after 100 hr respectively.

8.5 Variation of Reactor Temperature

The reaction rate equation has an exponential dependence on temperature; consequently temperature is expected to have a strong effect on methane conversion. Experiments examining the effect of varying the reactor temperature were carried out on catalyst bed B and catalyst bed C (experiments 4 and 9). Experimental parameters for the reaction temperature experiments are listed in Table 8.4.

Table 8.4: Experimental parameters for variation of reactor temperature

Experiment #	4	9
Date of Experiment	4/7/2010	5/4/2010
Catalyst Bed	B	C
Catalyst Loading (mg)	31.1	54
Channel Height (mm)	0.84	0.7
Upstream Pressure Range (kPa)	108.9 - 111.0	105.4 - 107.7
CH4 Flow Rate (g/min)	0.178 - 0.225	0.183 - 0.233
Steam - Methane Ratio	2.92 - 3.07	2.87 - 3.25
Residence Time (ms)	32.4 - 34.4	24.8 - 27.3
CO Selectivity (%)	55.7 - 63.1	27.0 - 54.3

The conditions of experiment 4 were such that the inlet temperature was varied while the other torches were kept at a constant level. The surface profiles that developed as a result

are shown in Fig. 8.7. Calculations were performed prior to the experiment in order to determine the flow rates necessary to operate at a set residence time due to the variations of density with pressure.

The experiments conducted on bed B on 4/7/10 (experiment 4) only consisted of four data points, but the exponential nature of the curve was still quite evident (Fig. 8.8).
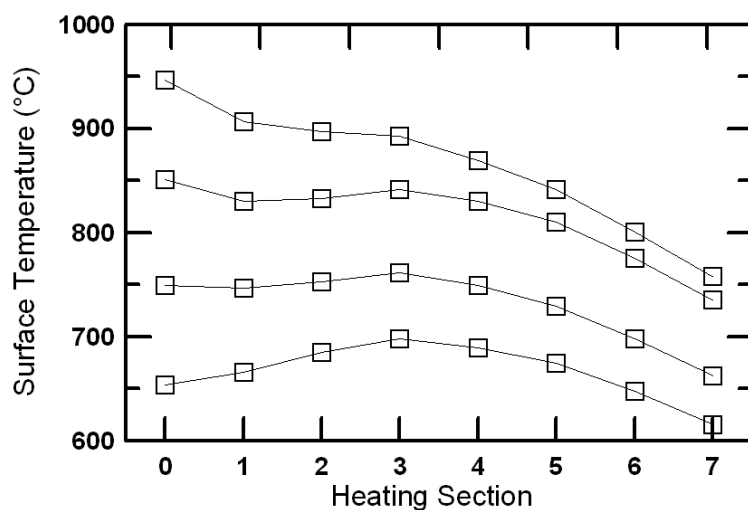
Fig. 8.7: Temperature profiles for experiment 4
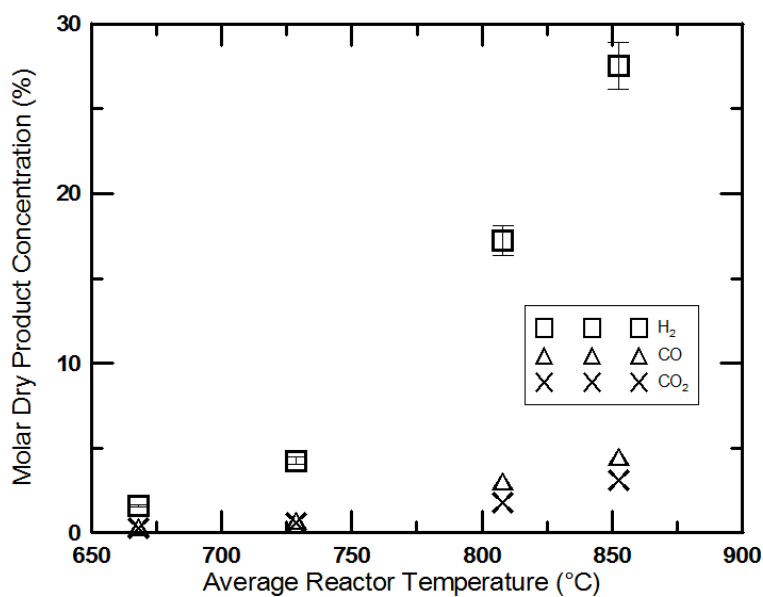
Fig. 8.8: Effects of variation of reaction temperature on catalyst bed B (Exp. 4)

A more thorough investigation of temperature effects was conducted during experiment 9 on catalyst bed C. The temperature profiles in this experiment were much more uniform as isothermal conditions were desired. The temperature profiles for experiment 9 are shown in Fig. 8.9 and the outlet concentrations are shown in Fig. 8.10.
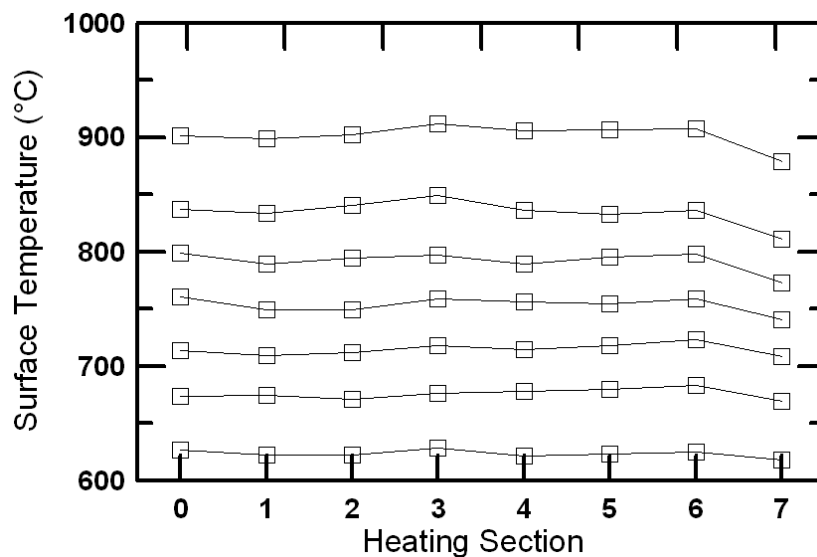
Fig. 8.9: Temperature profiles for experiment 9

$H_2(\%) = 160022 * \exp(-7098/T)$
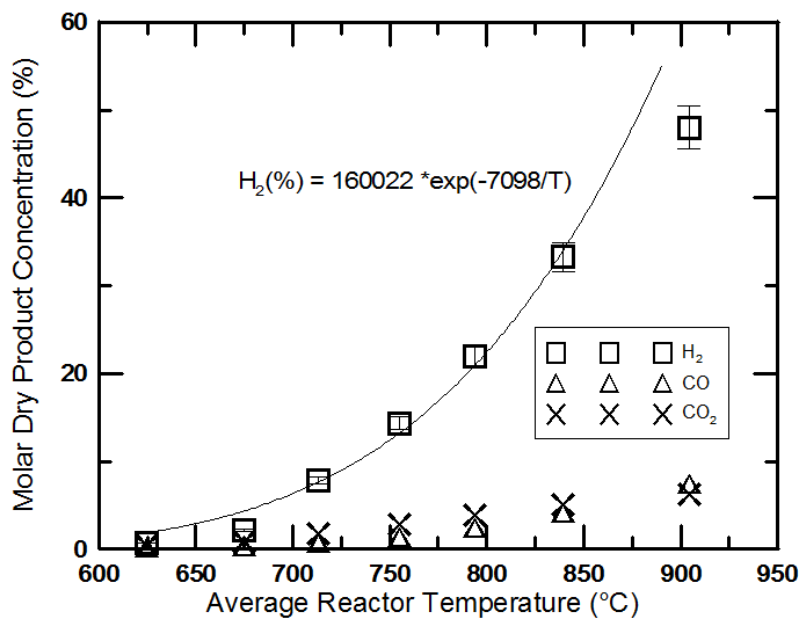
Fig. 8.10: Effects of variation of reaction temperature on catalyst bed C (Exp. 9)

The trends of the hydrogen production curves as a function of reactor temperature of the two experiments matched closely between the two catalyst beds, with catalyst bed C having a higher hydrogen production than bed B. The results from these two experiments are not directly comparable due to the difference in residence times, channel heights, and temperature profiles (variable temperature distribution versus flat).
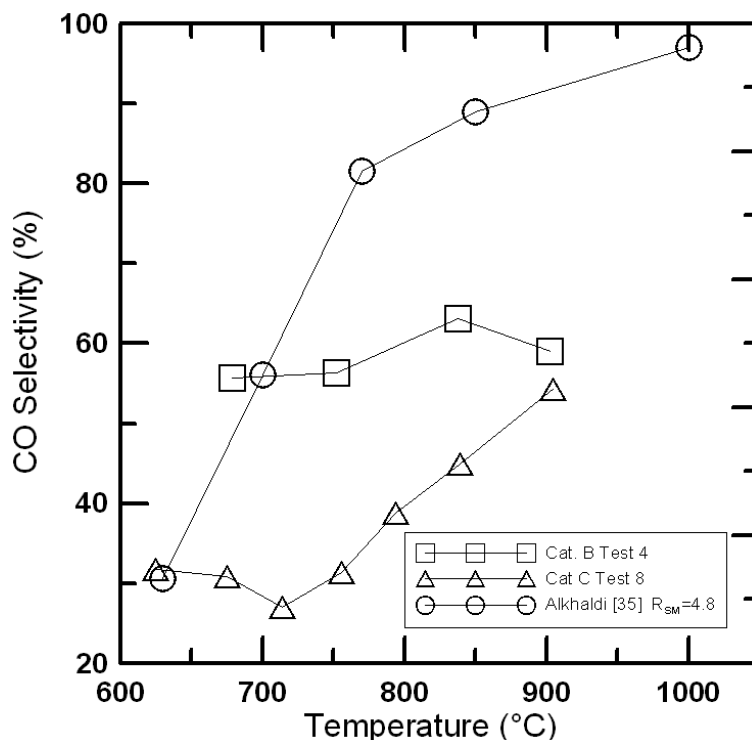
Fig. 8.11: Effects of variation of reaction temperature on CO selectivity

The CO selectivity between the two catalyst beds followed very different trends. The selectivity of bed B stayed near constant throughout the temperature range, while bed C showed a strong positive correlation between temperature and CO selectivity at temperatures greater than 700°C (Fig. 8.11).

Alkhaldi [35] observed a strong correlation of CO selectivity and temperature over a Pd catalyst; the results of which are plotted alongside the current experimental data. The CO selectivities seen in this work were generally lower than those seen by Alkhaldi [35].

8.6 Variation of Steam-Methane Ratio

Experiment 5 on catalyst bed B was carried out to test for changes in reaction with variations of the steam-methane ratio. Experimental conditions are listed in Table 8.5. The advantages of using a smaller steam-methane ratio would be decreased energy costs of heating the steam and increased residence times for a given methane flow rate. Rapid catalyst deactivation can occur at lower steam-methane ratios due to coke formation. In order to avoid this, the lowest steam-methane ratio tested was limited to 2.5

Table 8.5: Experimental parameters for steam-methane ratio variation (Exp. 5)

Date of Experiment	4/7/2010
Catalyst Bed	B
Catalyst Loading (mg)	31.1
Channel Ht (mm)	0.84
Pressure Range (kPa)	109.3 - 119.8
CH4 Flow Rate (g/min)	0.150 - 0.300
Average Reactor Temp (°C)	817 - 826
Residence Time (ms)	24.8 - 27.2
CO Selectivity (%)	55.1 - 63.1

The flow rate of methane and steam were adjusted in order to keep the residence time through the reactor near constant ($t_{res} = 25.4 \pm 1.8$ ms). The temperature profile used during this experiment is shown in Fig. 8.12. The molar output percentages are plotted in Fig. 8.13.
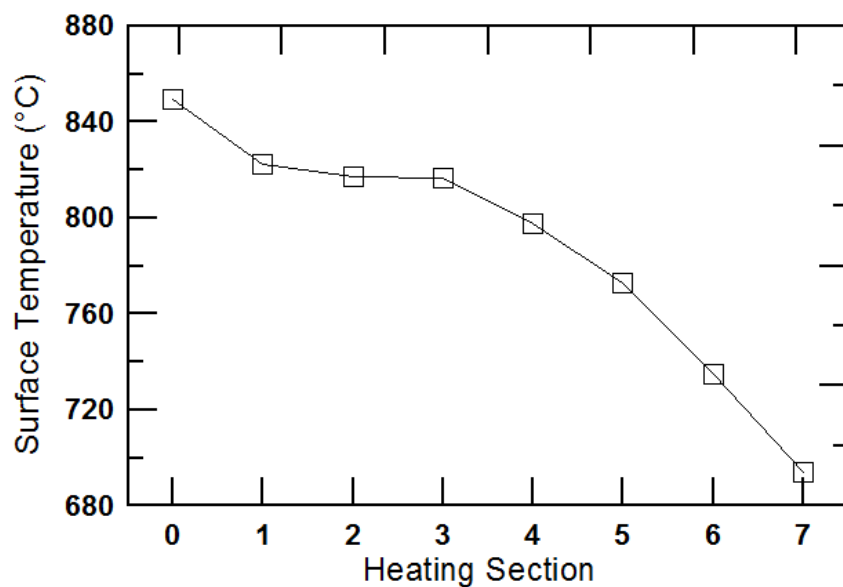
Fig. 8.12: Temperature profile for variable steam-methane ratio (Exp. 5)
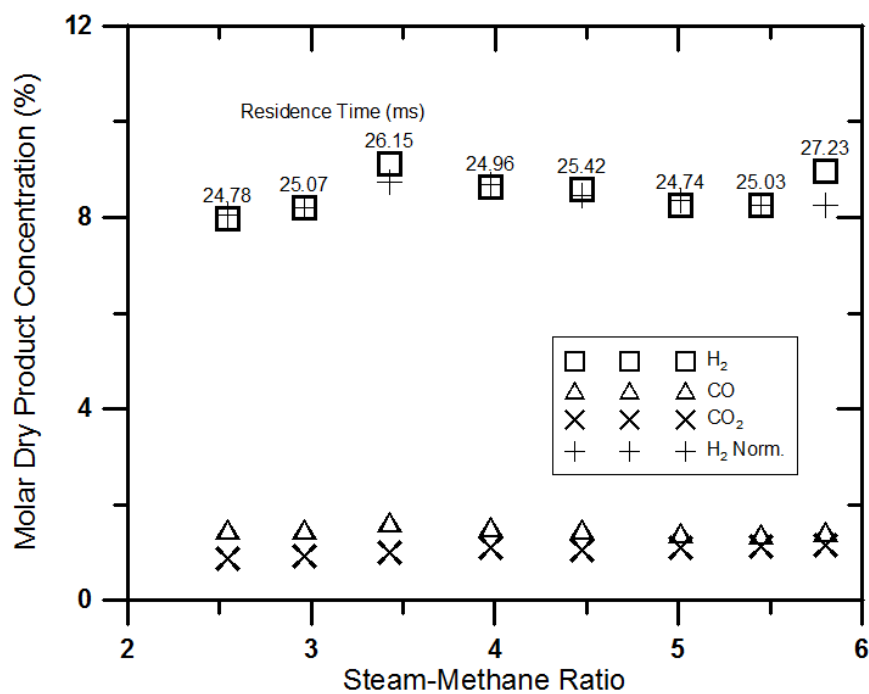
Fig. 8.13: Effects of varying the steam-methane ratio (Exp. 5)

Little difference was observed amongst sample points, with variations in output corresponding well to slight changes in residence time. The H_2 molar concentrations were normalized to a residence time of 25 ms as follows

$$y_{H_2 NORM} = y_{H_2} \left(\frac{25}{t_{res}} \right) \qquad\qquad (8.1)$$

where y_{H_2} is the molar concentration of H_2 and t_{res} is the residence time in milliseconds. By normalizing the H_2 concentrations, several of the outlying points were brought closer to a straight line, suggesting that the steam-methane ratio has little to no effect on the H_2 output under the conditions tested.

8.7 Variation of Temperature Distribution

Experiment 11 was conducted on catalyst bed C to explore the influence of temperature distribution along the reactor.   Experimental conditions are listed in Table 8.6. The configuration was such that the average temperature of the reactor was held constant at 750°C, but the longitudinal temperature profiles were varied across four different ramp configurations (Fig. 8.14).

Table 8.6: Experimental conditions of variable temperature distribution (Exp. 11)

Date of Experiment	4/28/2010
Catalyst Bed	C
Catalyst Loading (mg)	54
Channel Ht (mm)	0.7
Pressure Range (kPa)	107.5 - 108.1
CH4 Flow Rate (g/min)	0.194
Steam - Methane Ratio	3.01 - 3.07
Average Reactor Temp (°C)	748.1 - 757.8
Residence Time (ms)	25.7 - 29.6
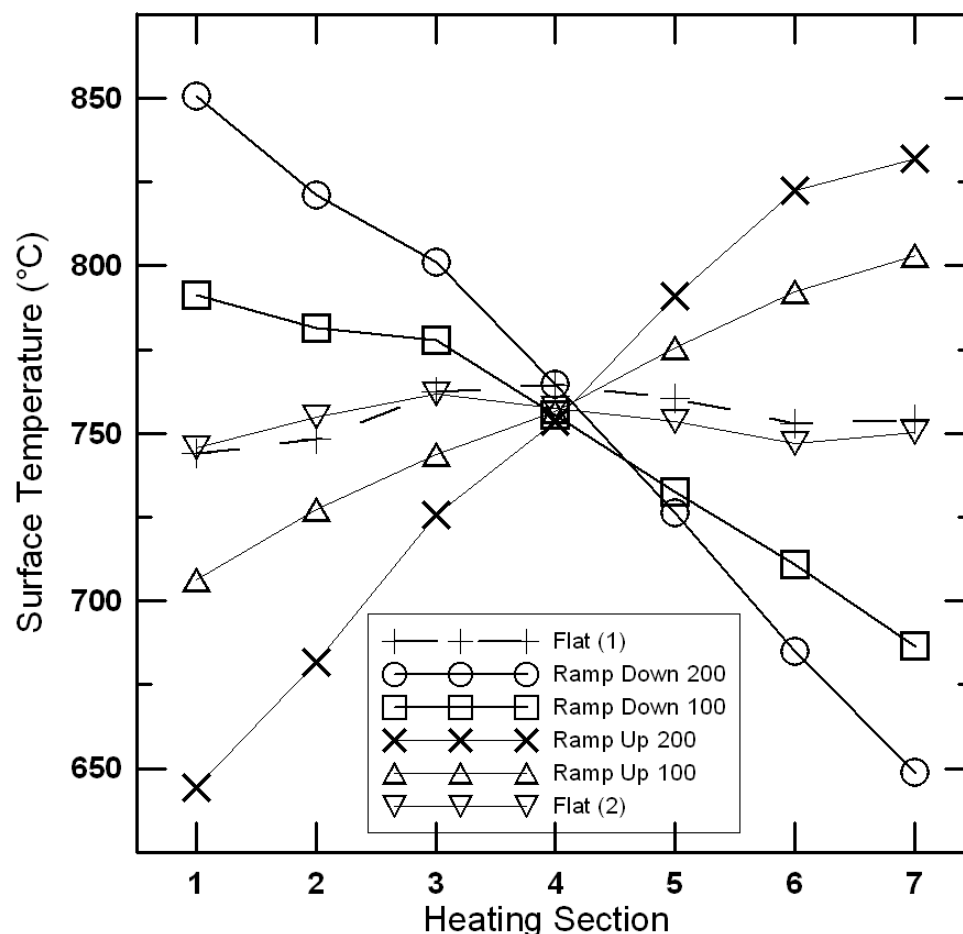
Fig. 8.14: Reactor surface temperature distributions (Exp. 11)

Two flat profiles were tested, one at the start and one at the end of the experiment to check for consistency. Two "ramp up" and two "ramp down" profiles were tested; one with a temperature difference of 100°C from the entrance of the reactor to the exit, and one with a difference of 200°C, for a total of four ramping configurations. It was expected that the Ramp Down 200 temperature profile would exhibit the highest conversion rate due to the greatly elevated temperatures (and reaction rates) at the inlet, where the partial pressure of methane was greatest. The gas chromatograph output from the experiment is plotted in Fig. 8.15. All ramping scenarios produced a significantly higher percentage of hydrogen than the flat line profiles. The Ramp Down 200 scenario produced the most hydrogen, but not significantly so. The Ramp Up 100 scenario produced slightly more hydrogen than the Ramp Up 200 scenario, suggesting that the

reaction rate at the entrance of the reactor is more important than overall maximum temperature in the reactor.
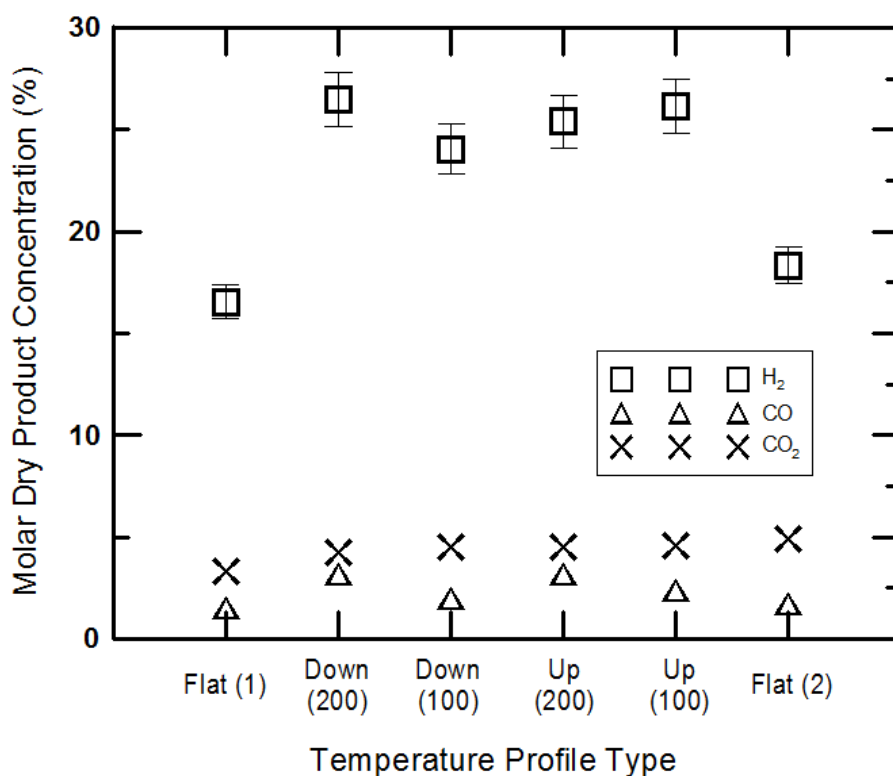
Fig. 8.15: Gas concentrations from variable temperature profile testing (Exp. 11)

8.8 Application of Experimental Data to Numerical Model

Data from the residence time variation experiments on catalyst bed B (Exp. 3) and C (Exp. 10) (see Table 8.1) were used as inputs into the CFD model being developed by Peterson [1] to establish multipliers to pre-exponential factors of the rate constants of reaction 1 (see Eq. (2.7)). The model was tuned in an iterative fashion in order to find the constants that best fit the H_2 production demonstrated in these experiments. Numerical versus experimental results for catalyst bed B and C are shown in Fig. 8.16.
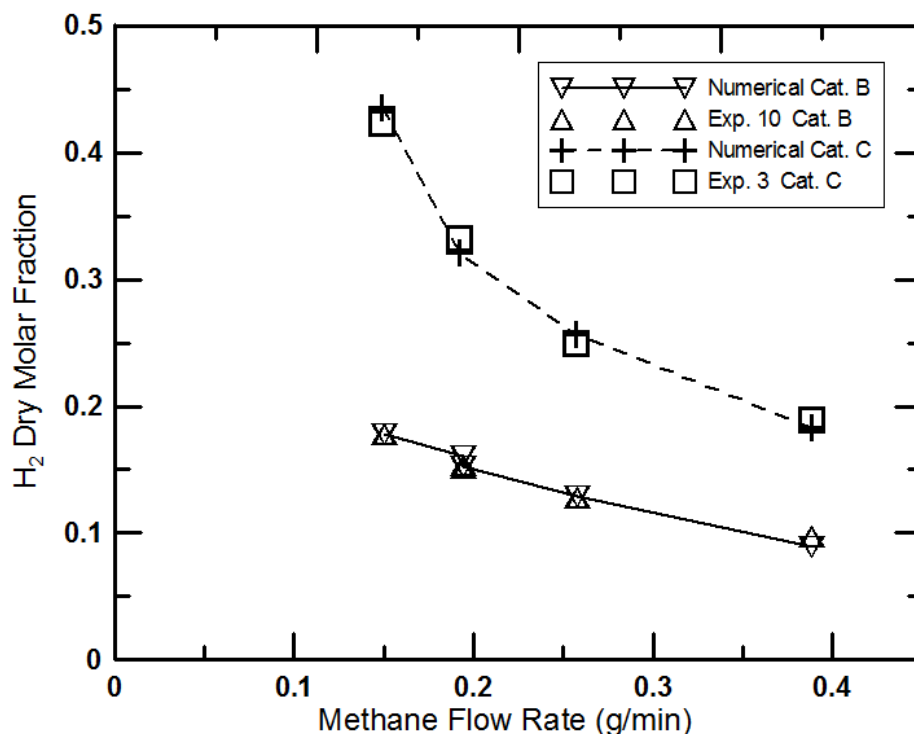
Fig. 8.16: Numerical versus experimental results for catalyst bed B and C, taken from [1]

The average error between the numerical and experimental results for these data was 3% for both catalyst beds. Since these were the calibration data sets, one would expect good agreement. The robustness of a numerical model comes in predicting parameters outside of the calibration data set. This model only takes into account the varied parameter over which the calibration experiments were performed; in this case CH_4 flow rate (analogous to residence time for a set channel height). To ensure robustness of the model it would be necessary to incorporate other variations of parameter, most importantly temperature. The modeling effort by Peterson [1] represents a good first step to simulating the reaction investigated here, but further integration of the experimental results provided here could greatly improve the performance and applicability of such a model. Standardized catalyst deposition procedures and tighter experimental control would also greatly facilitate the calibration and future development of such a model.

9. CONCLUSIONS AND RECOMMENDATIONS

A microchannel steam-methane reformer capable of producing variable temperature distributions was designed and tested. Catalyst stability was analyzed and the effects of temperature, residence time, steam-methane ratio, and temperature distribution were established.

9.1 Conclusions

The catalyst stability testing produced variable results. The initial stability test exhibited a large temporary decrease in methane conversion without any noticeable changes in input parameters. Subsequent testing on the same catalyst bed produced results more typical of what has been seen in literature. Whether this is a function of a change in the catalyst activity or a product of unmeasured changes in operational parameters is unknown.

The response of methane conversion to reactor temperature was established as exponential. Maximum hydrogen production from a steam-methane reformer will occur at the maximum temperature possible. Therefore special attention should be given to materials selection to maximize the working temperature.

A linear response of H_2 production to residence time was established up until H_2 concentrations reached 25%. The non-linearity exhibited at higher H_2 concentrations is readily explained by the reduction of the partial pressure of CH_4 which serves to slow the reaction.

Variation of the steam-methane ratio, while maintaining a set residence time, produced no change in the outlet gas composition. The total volume of hydrogen production is reduced at higher steam-methane ratios due to the reduced amount of methane in the inlet stream, but the percent of methane that is converted stays constant.

Tests involving the variation of the temperature distribution established that an elevated temperature served to accelerate the reaction, regardless of the spatial location of that elevated temperature. Temperature distributions with spatial variations of 100°C and

200°C produced similar results, with average H_2 output increased by 46% over testing isothermally at the same average temperature.

Increasing catalyst loading was demonstrated to increase the methane conversion percent. Preferential loading of the catalyst bed on the side exposed to the open channel surface produces enhanced methane conversion suggesting that the entire catalyst bed is not being fully utilized.

Initial calibration of the CFD model by Peterson [1] showed good agreement with H_2 molar outlet concentration, with errors near 3% for both catalyst bed B and C.

9.2 Recommendations for future work

Several aspects of the current reactor design could be modified to achieve enhanced performance. The thermocouple network present at the bottom of the reactor was implemented with the hope of being able to quantify the heat flux entering the channel. The thermal losses in the system were such that this could not be accurately quantified. Situating the thermocouples closer to the reactor channel would allow a better estimate of the temperature at the reactor surface.

Manual control of heat input should be eliminated in order to achieve more accurate control of the temperature distribution. Ideally a network of computer-controlled high-temperature microheaters could be used.

It is recommended that Rhodium be considered as an alternative catalyst. Recent studies have found that Rh is highly active and stable catalyst capable of coke free reforming at steam-methane ratios as low as one. Accelerating the reaction would serve to increase hydrogen output and investigate smaller residence times. If the reaction is greatly accelerated a smaller gap microchannel should be used to avoid diffusion limitations at the reduced time scales.

Any future experiments should consider the use of an alternative mass flow controller capable of higher accuracies at lower flow rates. This would decrease the residence time and steam-methane ratio uncertainties and allow investigation of more complete reactions.

In-line gas analysis should be implemented thereby increasing the number of sample points possible, and allowing the researcher to have real-time feedback regarding the dynamics of the system. Systems such as the Agilent Micro-GC 3000 would be ideal and are capable of returning sample analysis in less than 160 seconds, three times faster than the GC used in this work.

The next step in evaluating the feasibility of microchannel steam-methane reforming within a solar receiver would ideally involve the simulation of thermal transients (such as clouds passing overhead). A control network could be established whereby the system would be able to detect the change in solar input and adapt in such a way as to maintain optimal reformation activity.

References

[1] Peterson D., 2010, Numerical Simulation of Micro/Mini-Channel based Methane-Steam Reformer, Ph. D. Thesis, Oregon State University.

[2] Rostrup-Nielsen J. R., and Rostrup-Nielsen T., 2002, "Large-Scale Hydrogen Production," CATTECH, **6**(4), pp. 150-159.

[3] Chaniotis A., and Poulikakos D., 2005, "Modeling and optimization of catalytic partial oxidation methane reforming for fuel cells," Journal of Power Sources, **142**(1-2), pp. 184-193.

[4] Pregger T., Graf D., Krewitt W., Sattler C., Roeb M., and Möller S., 2009, "Prospects of solar thermal hydrogen production processes," International Journal of Hydrogen Energy, **34**(10), pp. 4256-4267.

[5] Stutz M. J., and Poulikakos D., 2005, "Effects of microreactor wall heat conduction on the reforming process of methane," Chemical Engineering Science, **60**(24), pp. 6983-6997.

[6] Rostrup-Nielsen J. R., Sehested J., and Norskov J. K., 2002, "Hydrogen and Synthesis Gas by Steam and CO2 Reforming," Advances in Catalysis, **47**, pp. 65-139.

[7] Rostrup-Nielsen T., 2005, "Manufacture of hydrogen," Catalysis Today, **106**(1-4), pp. 293-296.

[8] Akers W. W., and Camp D. P., 1955, "Kinetics of the methane-steam reaction," AIChE Journal, **1**(4), pp. 471-475.

[9] Bodrov N. M., Apelbaum L. O., and Temkin M. I., 1964, "Kinetics of the reaction of methane with steam on the surface of nickel," Kinetics and Catalysis, **5**, pp. 696-705.

[10] Bodrov N. M., Apelbaum L. O., and Temkin M. I., 1967, "Kinetics of the reaction of methane with water vapour, catalyzed nickel on a porous carrier," Kinetics and Catalysis, **8**, pp. 821-828.

[11] Bodrov N. M., Apelbaum L. O., and Temkin M. I., 1967, "Kinetics of the reaction of methane with steam on the surface of nickel at 400-600C," Kinetics and Catalysis, **9**, pp. 1065-1071.

[12] Ross J. R. H., and Steel M. C. F., 1973, "Mechanism of the steam reforming of

methane over a coprecipitated nickel-alumina catalyst," J. Chem. Soc., Faraday Trans. 1:, **69**, pp. 10-21.

[13] Agnelli M. E., Ponzi E. N., and Demicheli M. C., 1987, "Catalytic deactivation of methane steam reforming catalysts. 1. Activation," Industrial & Engineering Chemistry Research, **26**(8), pp. 1704-1707.

[14] De Deken J., Devos E. F., and Froment G. F., 1982, Steam reforming of natural gas: intrinsic kinetics, difusional influence and reactor design, American Chemical Society, Boston MA.

[15] Numaguchi T., and Kikuchi K., 1988, "Intrinsic kinetics and design simulation in a complex reaction network; steam-methane reforming," Chemical Engineering Science, **43**(8), pp. 2295-2301.

[16] Xu J., and Froment G. F., 1989, "Methane steam reforming, methanation and water-gas shift: I. Intrinsic kinetics," AIChE Journal, **35**(1), pp. 88-96.

[17] Hou K., and Hughes R., 2001, "The kinetics of methane steam reforming over a Ni/α-Al2O catalyst," Chemical Engineering Journal, **82**(1-3), pp. 311-328.

[18] Kuo K. K., 2005, Principles of Combustion, Wiley-Interscience.

[19] Van Hook J., "Methane-Steam reforming," Catalysis Reviews, **21**(1), pp. 1-51.

[20] Jones G., Jakobsen J. G., Shim S. S., Kleis J., Andersson M. P., Rossmeisl J., Abild-Pedersen F., Bligaard T., Helveg S., Hinnemann B., Rostrup-Nielsen J. R., Chorkendorff I., Sehested J., and Nørskov J. K., 2008, "First principles calculations and experimental insight into methane steam reforming over transition metal catalysts," Journal of Catalysis, **259**(1), pp. 147-160.

[21] Qin D., and Lapszewicz J., 1994, "Study of mixed steam and CO2 reforming of CH4 to syngas on MgO-supported metals," Catalysis Today, **21**(2-3), pp. 551-560.

[22] Rostrup-Nielsen J. R., and Hansen J. H. B., 1993, "CO2-Reforming of Methane over Transition Metals," Journal of Catalysis, **144**(1), pp. 38-49.

[23] Wang Y., Chin Y., Rozmiarek R., Johnson B., Gao Y., Watson J., Tonkovich A., and Vander Wiel D., 2004, "Highly active and stable Rh/MgOAl2O3 catalysts for methane steam reforming," Catalysis Today, **98**(4), pp. 575-581.

[24] Tonkovich A. L. Y., Yang B., Perry S. T., Fitzgerald S. P., and Wang Y., 2007, "From seconds to milliseconds to microseconds through tailored microchannel reactor design of a steam methane reformer," Catalysis Today, **120**(1), pp. 21-29.

[25] Sharma P. O., Abraham M. A., and Chattopadhyay S., 2007, "Development of a Novel Metal Monolith Catalyst for Natural Gas Steam Reforming," Industrial & Engineering Chemistry Research, **46**(26), pp. 9053-9060.

[26] Aartun I., Gjervan T., Venvik H., Görke O., Pfeifer P., Fathi M., Holmen A., and Schubert K., 2004, "Catalytic conversion of propane to hydrogen in microstructured reactors.," Chemical Engineering Journal, **101**(1-3), pp. 93-99.

[27] Tonkovich A., Perry S., Wang Y., Qiu D., LaPlante T., and Rogers W., "Microchannel process technology for compact methane steam reforming," Chemical Engineering Science, **59**(22-23), pp. 4819-4824.

[28] Tonkovich A. Y., Zilka J. L., LaMont M. J., Wang Y., and Wegeng R. S., 1999, "Microchannel reactors for fuel processing applications. I. Water gas shift reactor," Chemical Engineering Science, **54**(13-14), pp. 2947-2951.

[29] Johnson B. R., Canfield N. L., Tran D. N., Dagle R. A., Li X. S., Holladay J. D., and Wang Y., 2007, "Engineered SMR catalysts based on hydrothermally stable, porous, ceramic supports for microchannel reactors.," Catalysis Today, **120**(1), pp. 54-62.

[30] Venkataraman K., Wanat E. C., and Schmidt L. D., 2003, "Steam reforming of methane and water-gas shift in catalytic wall reactors," AIChE Journal, **49**(5), pp. 1277-1284.

[31] Stefanidis G. D., Vlachos D. G., Kaisare N. S., and Maestri M., 2009, "Methane steam reforming at microscales: Operation strategies for variable power output at millisecond contact times," AIChE Journal, **55**(1), pp. 180-191.

[32] Barbieri G., Violante V., Di Maio F. P., Criscuoli A., and Drioli E., 1997, "Methane Steam Reforming Analysis in a Palladium-Based Catalytic Membrane Reactor," Industrial & Engineering Chemistry Research, **36**(8), pp. 3369-3374.

[33] Hara S., Haraya K., Barbieri G., and Drioli E., 2008, "Reaction rate profiles in long palladium membrane reactors for methane steam reforming," Desalination, **233**(1-3), pp. 359-366.

[34] Lin Y., Liu S., Chuang C., and Chu Y., 2003, "Effect of incipient removal of hydrogen through palladium membrane on the conversion of methane steam reforming: Experimental and modeling," Catalysis Today, **82**(1-4), pp. 127-139.

[35] Alkhaldi K. H., 2005, Steam Reforming of Hydrocarbons in a Microreactor: Experiment and Modeling, Ph. D. Thesis, Oregon State University.

[36] Valmikanathan O., Ostroverkhova O., Mulla I., Vijayamohanan K., and Atre S., 2008, "The effect of synthesis procedure on the structure and properties of palladium/polycarbonate nanocomposites," Polymer, **49**(16), pp. 3413-3418.

[37] Holladay J. D., Wang Y., and Jones E., 2004, "Review of Developments in Portable Hydrogen Production Using Microreactor Technology," Chemical Reviews, **104**(10), pp. 4767-4790.

[38] Kolb G., and Hessel V., 2004, "Micro-structured reactors for gas phase reactions," Chemical Engineering Journal, **98**(1-2), pp. 1-38.

[39] Cao C., Wang Y., and Rozmiarek R. T., 2005, "Heterogeneous reactor model for steam reforming of methane in a microchannel reactor with microstructured catalysts," Catalysis Today, **110**(1-2), pp. 92-97.

[40] Steinfeld A., 2005, "Solar thermochemical production of hydrogen--a review," Solar Energy, **78**(5), pp. 603-615.

[41] Moller S., Kaucic D., and Sattler C., 2006, "Hydrogen Production by Solar Reforming of Natural Gas: A Comparison Study of Two Possible Process Configurations," J. Sol. Energy Eng., **128**(1), pp. 16-23.

[42] "SolarPACES Website "http://www.solarpaces.org/Tasks/Task2/solref.htm"."
[43] Hogan Jr. R., Skocypec R., Diver R., Fish J., Garrait M., and Richardson J., 1990, "A direct absorber reactor/receiver for solar thermal applications," Chemical Engineering Science, **45**(8), pp. 2751-2758.

[44] Wörner A., and Tamme R., 1998, "CO2 reforming of methane in a solar driven volumetric receiver-reactor," Catalysis Today, **46**(2-3), pp. 165-174.

[45] Levy M., Rubin R., Rosin H., and Levitan R., 1992, "Methane reforming by direct solar irradiation of the catalyst," Energy, **17**(8), pp. 749-756.

[46] Muir J. F., Hogan Jr. R. E., Skocypec R. D., and Buck R., 1994, "Solar reforming of methane in a direct absorption catalytic reactor on a parabolic dish: I--Test and analysis," Solar Energy, **52**(6), pp. 467-477.

[47] Almazo Optics Website "http://www.almazoptics.com"

[48] Beder E. C., Bass C. D., and Shackleford W. L., 1971, "Transmissivity and Absorption of Fused Quartz Between 0.22 μm and 3.5 μm from Room Temperature to 1500°C," Appl. Opt., **10**(10), pp. 2263-2268.

[49] Kuznetsov V., and Kozlov S., 2008, "Modeling of methane steam reforming in a

microchannel with a heat flow distributed in length," Journal of Engineering Thermophysics, **17**(1), pp. 53-59.

[50] Fuller E. N., Ensley K., and Giddings J. C., 1969, "Diffusion of halogenated hydrocarbons in helium. The effect of structure on collision cross sections," The Journal of Physical Chemistry, **73**(11), pp. 3679-3685.

[51] Incropera F. P., and De Witt D. P., 1985, Fundamentals of heat and mass transfer, 2nd edition.

[52] Twigg M. V., 1996, Catalyst Handbook, Manson Publishing.

[53] Brust M., Bethell D., Kiely C. J., and Schiffrin D. J., 1998, "Self-Assembled Gold Nanoparticle Thin Films with Nonmetallic Optical and Electronic Properties," Langmuir, **14**(19), pp. 5425-5429.

[54] Aartun I., 2004, "Catalytic conversion of propane to hydrogen in microstructured reactors," Chemical Engineering Journal, **101**, pp. 93-99.

[55] Moffat R. J., 1985, "Using Uncertainty Analysis in the Planning of an Experiment," J. Fluids Eng., **107**(2), pp. 173-178.

APPENDICES

Appendix A: Detailed drawings of reactor components
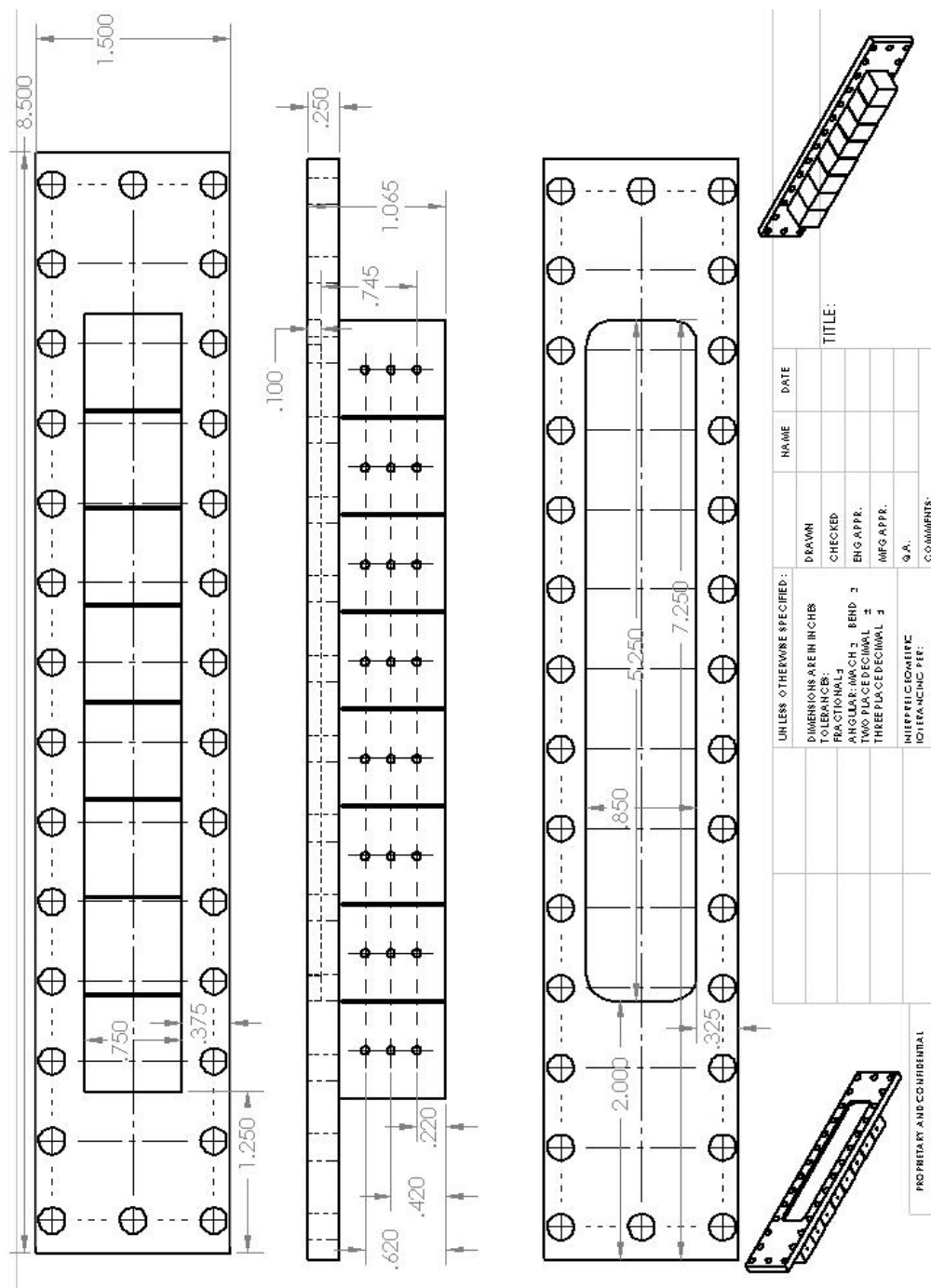
All dimensions in inches
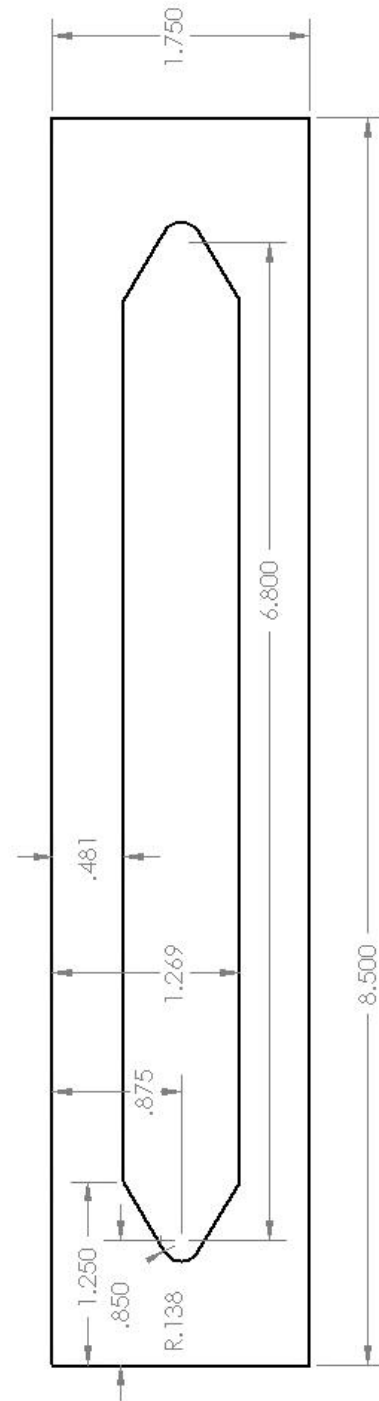

Fig. A.1: CAD drawing of reactor base and heating blocks

Appendix A cont.

Fig. A.2: CAD drawing of gasket/shim – height is a function of gasket material
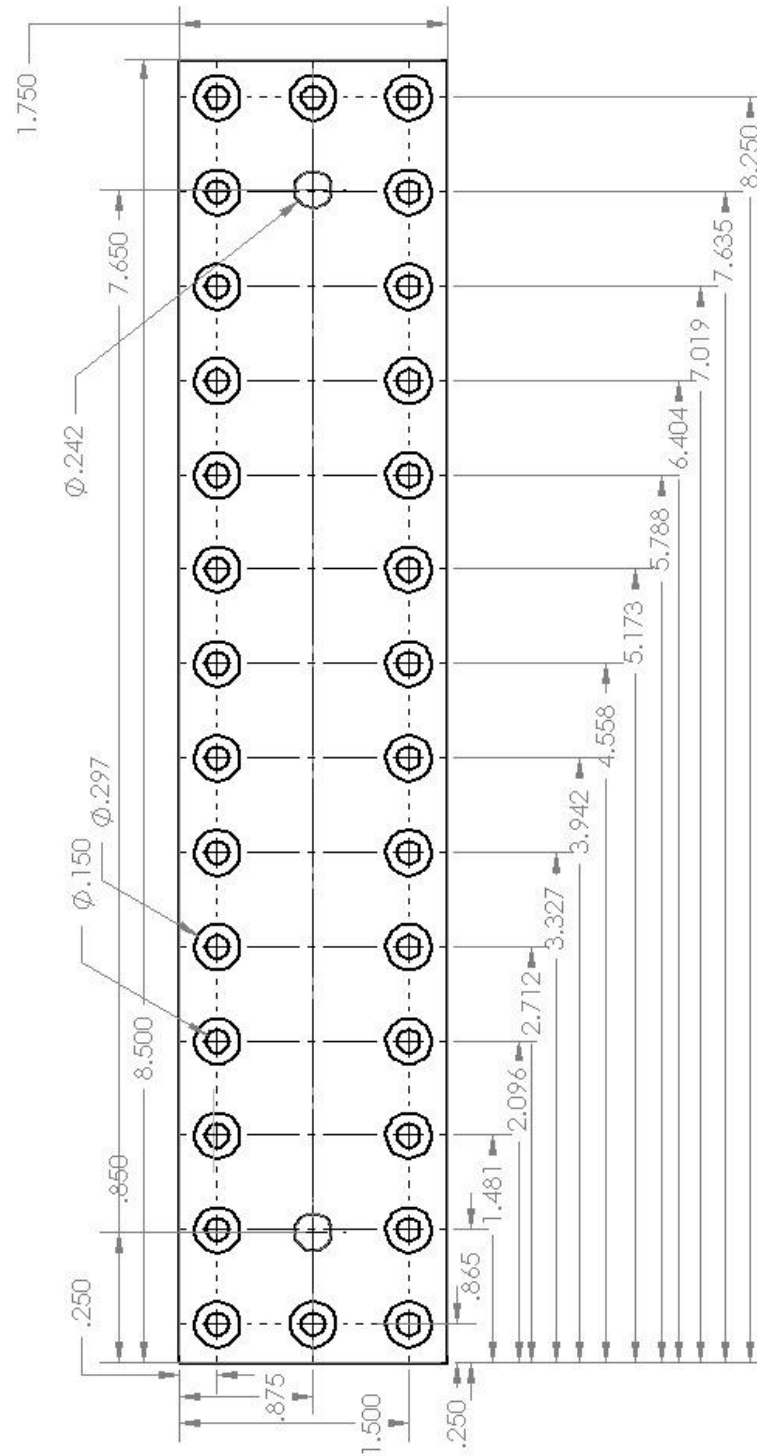
Appendix A cont.

Fig. A.3: CAD drawing of top plate of reactor

Appendix B: Thermocouple calibration parameters

Table B.1: Curve fits and uncertainties of thermocouple calibrations

Thermocouple	Slope	Intercept	Curve fit Uncertainty (°C)	Total Calibration Uncertainty (°C)
TC1	1.0012	-3.4219	0.246	0.60
TC2	1.0014	-3.3147	0.253	0.61
TC3	1.003	-3.2311	0.219	0.59
TC4	1.0012	-3.1173	0.241	0.60
TC5	1.0028	-2.3516	0.155	0.57
TC6	1.0013	-3.269	0.253	0.61
TC7	1.0011	-3.0906	0.253	0.61
TC8	1.003	-2.7426	0.157	0.57
TC9	1.0029	-3.8641	0.243	0.60
TC10	1.0034	-3.2461	0.171	0.58
TC11	1.001	-3.6546	0.246	0.60
TC12	1.0027	-2.8592	0.170	0.58
TC13	1.0018	-3.8953	0.249	0.60
TC14	1.0011	-3.9004	0.250	0.60
TC15	1.0018	-2.311	0.176	0.58
TC16	1.0036	-3.6844	0.248	0.60
TC17	1.0032	-3.7579	0.226	0.59
TC18	1.0035	-3.2664	0.173	0.58
TC19	1.0017	-3.5161	0.248	0.60
TC20	1.0034	-3.4429	0.216	0.59
TC21	1.0021	-2.6656	0.156	0.57
TC22	1.0022	-3.6767	0.239	0.60
TC23	1.0023	-2.6192	0.171	0.58
TC24	1.0018	-2.2523	0.174	0.58
TC25	1.0084	-4.2265	0.166	0.57
TC26	1.0054	-2.8543	0.161	0.57
TC27	1.0085	-2.6732	0.173	0.58

Appendix C: Uncertainty Analysis

The uncertainty analysis of salient calculated parameters is detailed in this section.
The perturbation analysis method involves computing the deviations from the nominal
calculated value by sequentially varying each input parameter by its associated
uncertainty. The uncertainty of the surface temperature was calculated as seen in Table
C.1.

Table C.1: Uncertainty of surface temperature

Surface Temperature (T_s)						
Nominal Value = 855.39°C						
Formula:	$T_s = T_1 + \dfrac{T_1 - T_2}{\Delta x_2} * \Delta x_3$					
Variable	Value	U_i	T_s (+ U_i)	T_s (-U_i)	Avg. U_{tot}	Avg U_{tot} (%)
T_1 (°C)	878.31	0.64%	870.71	840.07	15.318	1.7907%
T_2 (°C)	891.60	0.64%	845.55	865.24	9.843	1.1507%
Δx_2 (mm)	5.08	0.01	855.44	855.35	0.045	0.0053%
Δx_3 (mm)	8.763	0.05	855.26	855.52	0.131	0.0153%
					U_{tot} (RSS)	2.13%

The channel height was calculated using the following formula:
$$h_g = h_m - (h_t + h_b) - (h_c - h_d)$$
The uncertainty of the channel height was calculated using Kline and McClintock to
generate the following formula:
$$U_{h_g} = \sqrt{U_{h_g}^2 + U_{h_t}^2 + U_{h_b}^2 + U_{h_c}^2 + U_{h_d}^2}$$
The uncertainty of each measurement was 0.05 mm, resulting in a channel height
uncertainty of 0.11mm.

The uncertainty of the density measurement for H_2O was calculated using the
uncertainties of pressure and temperature as seen in Table C.2.

Table C.2: Uncertainty of density

Density (ρ)						
Nominal Value: 0.207025 (kg/m^3)						
Formula:	$\rho_i = \dfrac{\mathcal{M}_i P}{(T + 273.15)R}$					
Variable	**Value**	**U$_i$**	**ρ_{H_2O} (+ U$_i$)**	**ρ_{H_2O} (-U$_i$)**	**Avg. U$_{tot}$**	**Avg U$_{tot}$ (%)**
P (Pa)	107649	376 Pa	0.2077	0.2063	0.00072	0.35%
T (°C)	853.49	2.10%	0.1814	0.1874	0.00298	1.61%
R	8314.5	0	0.2070	0.2070	0.00000	0.00%
$\mathcal{M}_{H_2O}$ (g/mole)	16.04	0	0.2070	0.2070	0.00000	0.00%
					U$_{tot}$ (RSS)	1.65%

The uncertainty of density is valid for both H_2O and CH_4.

The uncertainty of the residence time was computed as seen in Table C.3.

Table C.3: Uncertainty of residence time

Residence Time (t$_{res}$)						
Nominal Value: 27.593 ms						
Formula:	$t_{res} = \dfrac{l * w * h}{\dfrac{\dot{m}_{CH4}}{\rho_{CH4}} + \dfrac{\dot{m}_{H_2O}}{\rho_{H_2O}}}$					
Variable	**Value**	**U$_i$**	**t$_{res}$ (+ U$_i$)**	**t$_{res}$ (-U$_i$)**	**Avg. U$_{tot}$**	**Avg U$_{tot}$ (%)**
l (mm)	133.35	0.05	27.60	27.58	0.010	0.04%
w (mm)	19	0.05	27.67	27.52	0.073	0.26%
h (mm)	0.7	0.11	31.93	23.26	4.336	15.71%
$\dot{m}_{CH4}$ (g/min)	0.1936	0.02313	26.72	28.52	0.899	3.26%
$\dot{m}_{H_2O}$ (g/min)	0.581	0.05	25.97	29.44	1.735	6.29%
ρ_{CH4} (kg/m^3)	0.18434	1.65%	27.72	27.47	0.124	0.45%
ρ_{H_2O} (kg/m^3)	0.20703	1.65%	27.92	27.26	0.331	1.20%
					U$_{tot}$ RSS	17.29%

The majority of the residence time uncertainty is from the uncertainty of the channel height. The channel height would be the same for all experiments on a given catalyst bed. Disregarding the channel height uncertainty would put the total residence time uncertainty at a more reasonable value of 7.22%.

The steam-methane ratio uncertainty was computed as seen in Table C.4.

Table C.4: Uncertainty of steam-methane ratio

Steam-Methane Ratio (R_{SM})						
Nominal Value: 2.6720						
Formula: $R_{SM} = \dfrac{\dot{m}_{H_2O}}{\dot{m}_{CH_4}} \times \dfrac{\mathcal{M}_{CH_4}}{\mathcal{M}_{H_2O}}$						
Variable	Value	U_i	R_{SM} (+ U_i)	R_{SM} (-U_i)	Avg. U_{tot}	Avg U_{tot} (%)
$\dot{m}_{CH_4}$ (g/min)	0.1936	0.02313	2.39	3.03	0.324	12.12%
$\dot{m}_{H_2O}$ (g/min)	0.581	0.05	2.90	2.44	0.230	8.61%
$\mathcal{M}_{H_2O}$ (g/mole)	18.015	0	2.67	2.67	0.000	0.00%
$\mathcal{M}_{CH_4}$ (g/mole)	16.04	0	2.67	2.67	0.000	0.00%
					U_{tot} RSS	14.86%

Even though the CH_4 flow rate had a higher uncertainty than that of the H_2O flow rate, it had a greater influence on the total uncertainty of the steam-methane ratio.

Appendix D: Results from experiments 2, 7, 11 and 12

Experimental details for these tests are available in Chapter 8 (Table 8.1).

Experiment 2 – Variation of Pressure

It was desired to characterize the reaction as a function of reactor pressure. An adjustable valve was installed in the test loop just prior to the outlet selector valve. By incrementally closing this valve, the pressure inside the reactor was increased. The pressure range for this set of experiments was 127 – 202 kPa. The molar concentrations are shown in Fig. D.1.
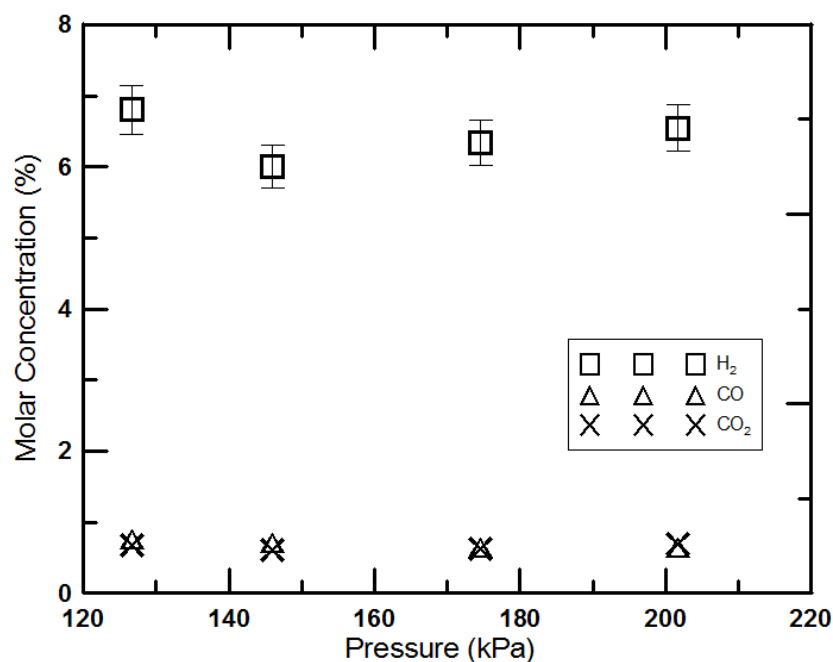

Fig. D.1: Gas returns of varied pressure test (Exp. 2)

During testing it was noticed that the rate of gas effluent from the reactor at higher pressures was greatly reduced, indicating leaks developing in the system. There was no flow rate measurement on the outlet; consequently the metric for this assessment was the length of time necessary to completely fill a sampling bag.

Experiment 7 – Variable heat flux testing

An attempt was made to match temperature profiles to those modeled by Peterson [1] in order to simulate a variable heat flux profile through the reactor. Multiple heat flux profiles were input into a calibrated model for catalyst bed C and the surface temperatures were computed. The variation of the calculated temperature profiles was less than the resolution readily attainable in the experimental facility. Due to large conduction and radiation losses in heating section 7, this heating torch had to be turned up much higher than the other torches. Torch 6 was turned off for all experiments, but the heat flux provided from the neighboring torches was more than what was necessary to reach the desired temperature. As a result, the surface temperature at heating section 6 was always greater than what was desired. The target, or model, temperature profiles along with the experimentally achieved profiles are shown in Fig. D.2.
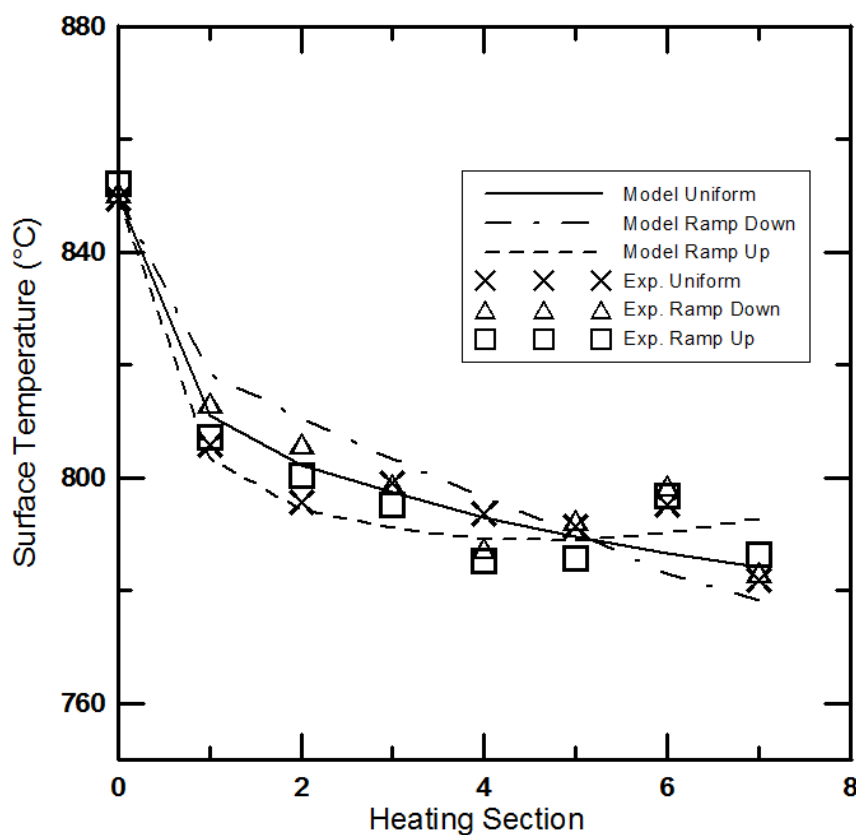

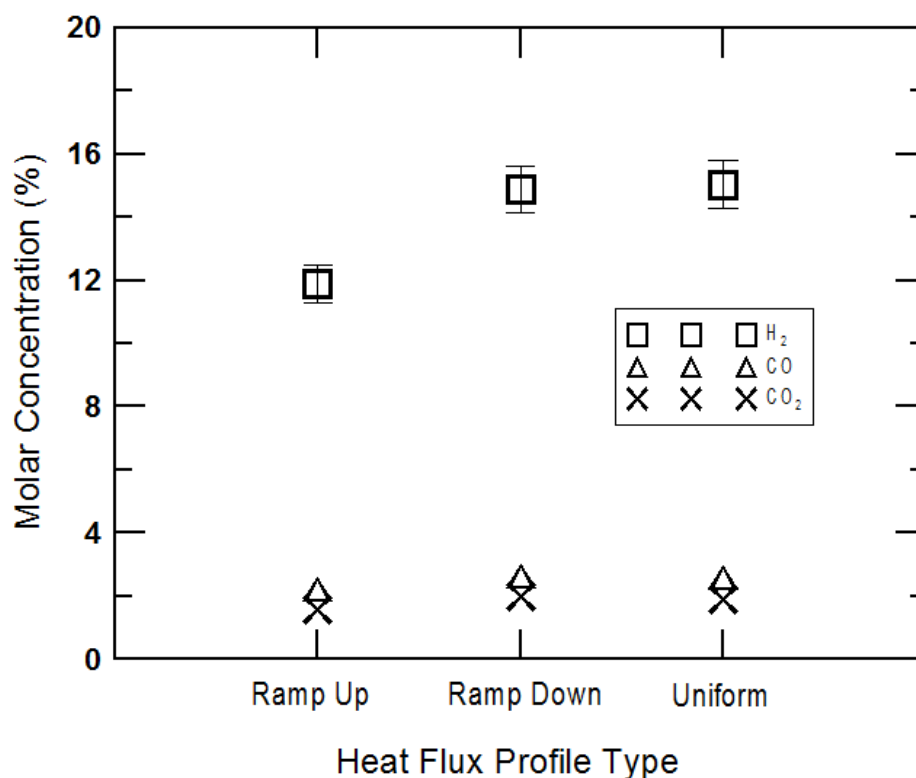Fig. D.2: Experimental versus target surface temperature profiles (Exp. 7)

Fig. D.3: Gas returns for experiment 7

Molar concentrations of the effluent stream are shown in Fig. D.3. The desired temperature profiles were not matched close enough to be able to draw any conclusions from the data.

Experiments 11 & 12 – Catalyst deposition on flat plate

An alternative catalyst configuration referred to as "catalyst bed D" was tested whereby the catalyst was deposited directly on the stainless steel wall of the reactor. The bottom portion of the channel was machined flat in order to remove the slot previously allocated for the FeCrAlY catalyst bed. A full batch (60 mg Pd) of particles was reduced to an approximate volume of 5 ml. The reactor surface was taped off and the Pd particles were deposited with a small paintbrush in a series of 3 applications. Approximately 2/3 of the catalyst batch was used (~40 mg Pd). The reactor was allowed to dry under a fume hood for at least four hours between sequential catalyst applications. The reactor could

not be dried in an oven due to the attached instrumentation. The reactor was assembled and situated in the experimental apparatus for testing. During the heat-up process smoke was seen exiting from the flow loop. No smoke was observed under initial heat up of the other catalyst beds, possibly because all other beds were dried in an oven prior to use. Catalyst bed D was tested for catalyst stability (experiment 12) and for temperature response (experiment 13). Test conditions can be found in Ch. 8 (Table 8.1). Output from experiment 12 is shown in Fig. D.4.
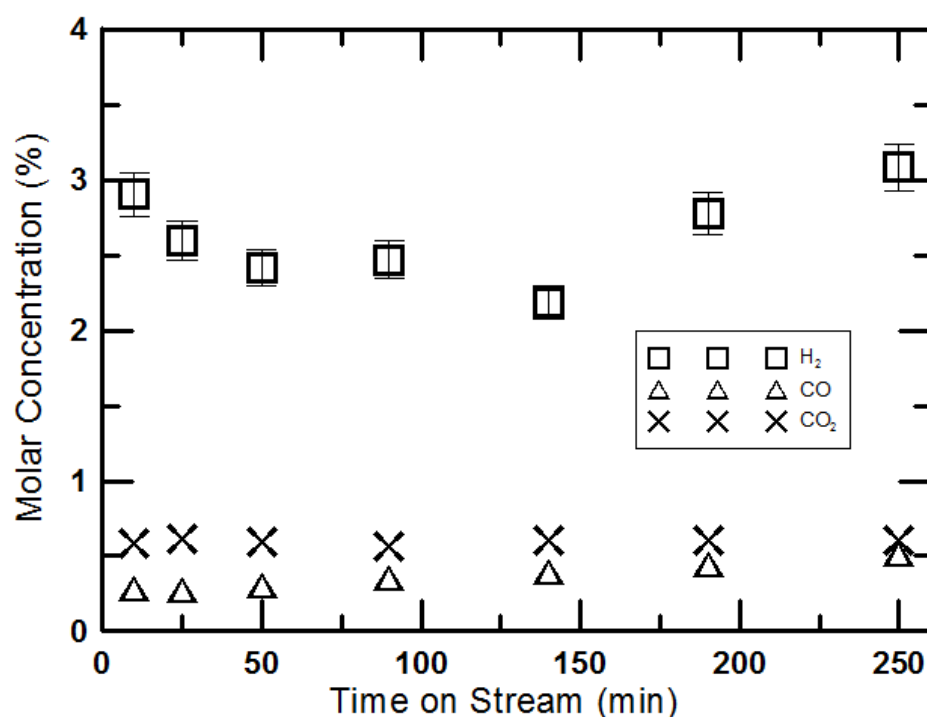

Fig. D.4: Gas output of stability testing of catalyst bed D (Exp. 12)

The H_2 output of this catalyst configuration ranged from 2.4 to 3.1%. No deactivation trend was seen, suggesting that the particles were adhering adequately to the stainless steel at the temperatures and flows tested. It was readily apparent that the increased surface area provided by the FeCrAlY felt served to greatly enhance conversion rates. Catalyst bed D was also tested for temperature response. After the 250 minute test was performed, the testing continued by varying the average reactor surface temperature from

625 – 925°C (experiment 13). The gas analysis of the variable temperature test of catalyst bed D is shown in Fig. D.5.
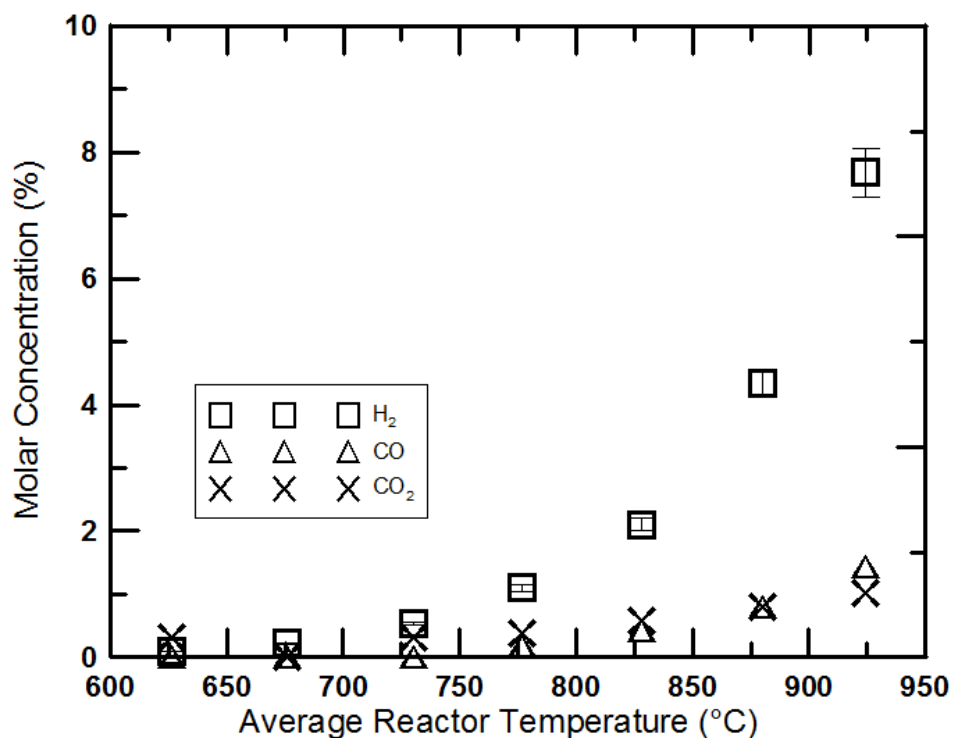

Fig. D.5: Output of variable temperature testing on catalyst bed D (Exp. 13)

The H₂ outlet concentration followed the same exponential trend as was seen in experiments 4 and 9 (see Fig. 8.8 and Fig. 8.10), but with much smaller conversion percentages.

Appendix E: Experimental data

Temperatures listed are average reactor surface temperatures.

Table E.1: Experiment 1: Catalyst Bed A, Test: variation of residence time

Sample	$\dot{m}_{CH_4}$ (g/min)	R_{SM}	t_{res} (ms)	P (kPa)	Temp (°C)	Molar Dry Product Composition			
						H_2 (%)	CO (%)	CH_4 (%)	CO_2 (%)
2.9.002	1.000	4.00	8.4	201	865	6.40	1.32	91.53	0.75
2.9.005	0.750	4.00	9.8	177	869	6.75	1.34	91.00	0.91
2.9.006	0.500	4.00	12.3	149	876	8.57	1.49	88.91	1.03
2.9.007	0.250	4.00	22.1	134	880	11.71	1.87	84.79	1.63

Table E.2: Experiment 2: Catalyst Bed A, Test: variation of pressure

Sample	$\dot{m}_{CH_4}$ (g/min)	R_{SM}	t_{res} (ms)	P (kPa)	Temp (°C)	Molar Dry Product Composition			
						H_2 (%)	CO (%)	CH_4 (%)	CO_2 (%)
2.15.002	0.250	4.00	22.9	127	777	6.80	0.75	91.77	0.68
2.15.005	0.250	4.00	26.7	146	767	6.01	0.70	92.68	0.61
2.15.008	0.250	4.00	32.0	175	765	6.34	0.64	92.40	0.63
2.15.009	0.250	4.00	37.0	202	763	6.54	0.63	92.13	0.69

Table E.3: Experiment 3: Catalyst Bed B, Test: variation of residence time

Sample	$\dot{m}_{CH_4}$ (g/min)	R_{SM}	t_{res} (ms)	P (kPa)	Temp (°C)	Molar Dry Product Composition			
						H_2 (%)	CO (%)	CH_4 (%)	CO_2 (%)
4.5.011	0.150	3.00	42.5	107	827	17.83	3.06	77.25	1.86
4.5.013	0.194	3.00	32.5	109	821	15.23	2.58	80.54	1.65
4.5.014.1	0.194	3.00	32.5	109	820	15.26	2.57	80.52	1.65
4.5.014.2	0.194	3.00	32.5	109	820	15.29	2.59	80.51	1.61
4.5.014.3	0.194	3.00	32.5	109	820	15.40	2.57	80.37	1.67
4.5.015	0.194	3.00	32.7	109	819	15.11	2.60	80.64	1.65
4.5.016	0.258	3.00	25.7	112	819	12.85	2.24	83.50	1.41
4.5.018	0.388	3.00	17.5	118	824	9.69	1.69	87.64	0.99
4.5.020	0.770	3.00	10.1	134	832	7.22	1.24	90.87	0.68

Table E.4: Experiment 4: Catalyst Bed B, Test: variation of temperature

Sample	$\dot{m}_{CH_4}$ (g/min)	R_{SM}	t_{res} (ms)	P (kPa)	Temp (°C)	Molar Dry Product Composition			
						H_2 (%)	CO (%)	CH_4 (%)	CO_2 (%)
4.7.005	0.225	3.01	32.4	109	668	1.60	0.31	97.85	0.25
4.7.007	0.203	3.07	32.8	109	729	4.26	0.73	94.45	0.56
4.7.008	0.193	3.06	32.2	110	808	17.25	3.04	77.93	1.78
4.7.009	0.178	2.92	34.4	111	852	27.53	4.47	64.89	3.11

Table E.5: Experiment 5: Catalyst Bed B, Test: variation of steam-methane ratio

Sample	$\dot{m}_{CH_4}$ (g/min)	R_{SM}	t_{res} (ms)	P (kPa)	Temp (°C)	Molar Dry Product Composition			
						H_2 (%)	CO (%)	CH_4 (%)	CO_2 (%)
4.7.011	0.150	5.80	27.2	120	826	8.97	1.42	88.46	1.16
4.7.012	0.161	5.45	25.0	112	824	8.26	1.38	89.23	1.13
4.7.013	0.175	5.01	24.7	112	821	8.25	1.39	89.27	1.09
4.7.014	0.191	4.47	25.4	114	820	8.60	1.48	88.87	1.05
4.7.015	0.210	3.98	25.0	112	820	8.65	1.54	88.72	1.10
4.7.016	0.233	3.43	26.2	115	817	9.13	1.62	88.25	1.00
4.7.017	0.263	2.96	25.1	112	818	8.20	1.47	89.42	0.92
4.7.019	0.300	2.54	24.8	113	819	7.96	1.48	89.69	0.87

Table E.6: Experiment 6: Catalyst Bed C, Test: catalyst stability

Sample	$\dot{m}_{CH_4}$ (g/min)	R_{SM}	t_{res} (ms)	P (kPa)	Temp (°C)	Molar Dry Product Composition				Time (m)
						H_2 (%)	CO (%)	CH_4 (%)	CO_2 (%)	
4.20.005	0.193	2.95	24.7	103	850	10.04	2.07	86.39	1.50	2
4.20.007	0.192	2.94	24.8	103	852	15.84	3.54	78.63	1.99	5
4.20.008	0.194	2.91	24.7	103	856	21.96	4.79	70.76	2.50	10
4.20.009	0.193	2.89	24.9	104	859	30.06	6.50	60.21	3.23	20
4.20.011	0.196	2.75	25.6	104	862	32.30	6.99	57.14	3.57	30
4.20.012	0.195	2.74	25.6	104	865	27.34	5.70	63.94	3.02	45
4.20.014	0.194	2.78	25.3	104	871	22.00	4.65	70.72	2.63	65
4.20.015	0.194	2.58	26.6	104	875	27.52	5.67	63.77	3.04	85
4.20.016	0.194	2.85	24.8	104	880	36.34	7.08	52.42	4.15	115
4.20.017	0.194	2.82	24.9	104	883	38.86	7.44	49.31	4.39	145
4.20.019	0.194	2.87	24.4	104	888	37.69	7.14	51.08	4.08	175
4.20.020	0.194	2.90	24.0	103	891	36.27	6.79	53.26	3.69	205
4.20.021	0.193	2.99	23.8	104	893	32.88	6.03	57.74	3.35	250

Table E.7: Experiment 7: Catalyst Bed C, Test: heat flux profile

Sample	$\dot{m}_{CH_4}$ (g/min)	R_{SM}	t_{res} (ms)	P (kPa)	Temp (°C)	Molar Dry Product Composition				Ramp
						H_2 (%)	CO (%)	CH_4 (%)	CO_2 (%)	
4.28.009	0.194	2.95	26.2	106	808	11.90	2.23	84.28	1.59	Ramp Up
4.28.011	0.194	2.95	25.7	104	811	14.89	2.66	80.45	2.00	Ramp Down
4.28.012	0.194	2.94	26.3	106	809	15.04	2.60	80.46	1.89	Flat

Table E.8: Experiment 8: Catalyst Bed C, Test: catalyst stability

Sample	$\dot{m}_{CH_4}$ (g/min)	R_{SM}	t_{res} (ms)	P (kPa)	Temp (°C)	Molar Dry Product Composition				Time (m)
						H_2 (%)	CO (%)	CH_4 (%)	CO_2 (%)	
5.03.003	0.194	3.05	24.1	105	862	47.10	6.22	41.39	5.28	10
5.03.005	0.194	2.89	25.2	105	861	44.93	5.67	44.14	5.27	25
5.03.007	0.194	2.93	25.0	105	860	42.64	5.47	46.64	5.25	50
5.03.008	0.194	2.98	24.7	105	859	38.31	5.28	51.46	4.96	90
5.03.009	0.194	2.89	26.0	108	853	34.80	4.98	55.40	4.83	140
5.03.011	0.194	2.89	25.0	106	874	37.92	5.55	51.04	5.49	190
5.03.012	0.194	2.86	25.4	106	874	37.36	5.45	52.14	5.05	250

Table E.9: Experiment 9: Catalyst Bed C, Test: variation of temperature

Sample	$\dot{m}_{CH_4}$ (g/min)	R_{SM}	t_{res} (ms)	P (kPa)	Temp (°C)	Molar Dry Product Composition			
						H_2 (%)	CO (%)	CH_4 (%)	CO_2 (%)
5.03.013	0.233	2.87	27.3	108	624	0.66	0.20	98.71	0.43
5.03.014	0.211	3.13	26.2	105	675	2.18	0.36	96.65	0.81
5.03.015	0.210	2.91	27.2	108	713	7.88	0.65	89.70	1.77
5.03.016	0.203	2.96	26.2	106	755	14.33	1.31	81.50	2.86
5.03.017	0.195	3.06	25.7	106	794	21.90	2.44	71.82	3.84
5.03.019	0.188	3.25	24.8	108	839	33.30	4.11	57.56	5.03
5.03.020	0.183	2.87	26.3	107	904	48.03	7.40	38.35	6.22

Table E.10: Experiment 10: Catalyst Bed C, Test: residence time

Sample	$\dot{m}_{CH_4}$ (g/min)	R_{SM}	t_{res} (ms)	P (kPa)	Temp (°C)	Molar Dry Product Composition			
						H_2 (%)	CO (%)	CH_4 (%)	CO_2 (%)
5.04.008	0.149	2.91	34.1	106	777	42.33	3.54	47.38	6.76
5.04.009	0.192	2.91	26.9	108	779	33.28	2.87	57.97	5.88
5.04.011	0.257	3.15	19.3	111	781	24.93	2.29	67.96	4.82
5.04.012	0.388	3.00	13.9	115	788	18.89	1.99	76.04	3.08
5.04.013	0.771	2.96	8.1	133	785	11.55	1.32	84.59	2.54
5.04.014	1.398	3.09	5.3	162	782	7.85	0.85	90.06	1.24

Table E.11: Experiment 11: Catalyst Bed C, Test: temperature profiles

Sample	$\dot{m}_{CH_4}$ (g/min)	R_{SM}	t_{res} (ms)	P (kPa)	Temp (°C)	Molar Dry Product Composition				Ramp
						H_2 (%)	CO (%)	CH_4 (%)	CO_2 (%)	
5.04.015	0.194	3.07	27.3	108	755	16.55	1.51	78.60	3.34	Flat 1
5.04.016	0.194	3.04	25.7	108	757	26.45	3.19	66.12	4.24	Down 200
5.04.017	0.194	3.01	29.6	108	750	25.39	3.19	66.91	4.51	Up 200
5.04.019	0.194	3.01	28.5	108	758	26.16	2.38	66.85	4.61	Up 100
5.04.020	0.194	3.01	27.0	108	748	24.05	2.02	69.43	4.50	Down 100
5.04.021	0.194	3.04	27.6	108	753	18.34	1.73	75.05	4.88	Flat 2

Table E.12: Experiment 12: Catalyst Bed D, Test: catalyst stability

Sample	$\dot{m}_{CH_4}$ (g/min)	R_{SM}	t_{res} (ms)	P (kPa)	Temp (°C)	Molar Dry Product Composition				Time (m)
						H_2 (%)	CO (%)	CH_4 (%)	CO_2 (%)	
5.12.003	0.284	2.86	26.3	104	848	2.91	0.28	96.23	0.58	10
5.12.005	0.285	2.76	26.8	104	850	2.60	0.28	96.51	0.61	25
5.12.007	0.285	3.03	25.1	104	850	2.42	0.30	96.69	0.59	50
5.12.008	0.285	3.01	25.3	104	851	2.47	0.36	96.61	0.56	90
5.12.009	0.285	2.95	25.6	104	853	2.18	0.39	96.82	0.60	140
5.12.011	0.285	2.91	26.0	104	853	2.77	0.44	96.18	0.60	190
5.12.012	0.285	2.85	26.3	104	850	3.09	0.51	95.80	0.61	250

Table E.13: Experiment 13: Catalyst Bed D, Test: variation of temperature

Sample	$\dot{m}_{CH_4}$ (g/min)	R_{SM}	t_{res} (ms)	P (kPa)	Temp (°C)	Molar Dry Product Composition			
						H_2 (%)	CO (%)	CH_4 (%)	CO_2 (%)
5.12.013	0.336	3.12	26.1	104	626	0.09	0.00	99.60	0.30
5.12.014	0.320	2.82	28.0	104	676	0.22	0.00	99.78	0.00
5.12.015	0.301	2.90	28.0	105	730	0.53	0.00	99.16	0.31
5.12.016	0.288	3.01	27.4	107	777	1.11	0.19	98.32	0.38
5.12.017	0.275	2.84	27.8	103	828	2.10	0.42	96.89	0.59
5.12.019	0.264	3.00	26.6	104	880	4.35	0.80	94.04	0.81
5.12.020	0.255	3.13	25.7	104	924	7.68	1.44	89.85	1.03